Technische Universität München
Lehrstuhl für Physikalische Chemie

Cluster catalysis under UHV and ambient conditions

Sebastian M. Kunz

Vollständiger Abdruck der von der Fakultät für Chemie der Technischen Universität München zur Erlangung des akademischen Grades eines

Doktors der Naturwissenschaften

genehmigten Dissertation.

Vorsitzender: Univ.-Prof. H. Gasteiger, Ph.D.

Prüfer der Dissertation:
1. Univ.-Prof. Dr. U. K. Heiz
2. Univ.-Prof. Dr. J. A. Lercher
3. Univ.-Prof. Dr. K. Köhler

Die Dissertation wurde am 28.4.2010 bei der Technischen Universität München eingereicht und durch die Fakultät für Chemie am 14.6.2010 angenommen.

For Irmgard Kunz (1923-2009)

There's a dark cloud rising from the desert floor
I packed my bags and I'm heading straight into the storm

(Bruce Springsteen – The promised land)

Contents

1 Introduction 1

2 Literature survey and theoretical background 5

2.1 CO oxidation 5

2.1.1 General remarks 5

2.1.2 Oxygen dissociation during CO oxidation 6

2.1.3 CO poisoning 8

2.1.4 Support effects 10

2.2 Ultraviolet photoelectron spectroscopy (UPS)/ Metastable impact electron spectroscopy (MIES) 17

2.2.1 Ultraviolet photoelectron spectroscopy (UPS) 17

2.2.1.1 Basic principle of photoelectron spectroscopy (PES) 18

2.2.1.2 Work function and Jellium model 20

2.2.1.3 Work function determination 21

2.2.1.4 Conservation of energy and sample work function 22

2.2.1.5 Complete formulation of the three-step model 25

2.2.1.6 Angle-Resolved UPS (ARUPS) 32

2.2.2 Metastable Impact electron spectroscopy (MIES) 34

2.2.2.1 Singlet vs. Triplet state 34

2.2.2.2 Overview of the different photo ionization mechanisms of MIES 35

2.2.2.3 Auger Deexcitation (AD) 36

2.2.2.4 Resonant Transfer (RT) 37

2.2.2.5 Resonant Transfer (RT) followed by Auger Neutralization (AN) 38

2.2.2.6 Resonant Transfer (RT) followed by Autodetachment (AU) or Auger Deexcitation (AD) 40

3 Experimental 42

3.1 Cluster source 42

3.2 Vacuum chamber 43

3.2.1 Sample 44

3.2.1.1 Crystal holder 44

3.2.1.2 Crystal cleaning 45

3.2.1.3 Preparation of MgO film 45

3.2.2 MIES/UPS 46

3.2.2.1 General aspects of a DC discharge source 46
3.2.3 First MIES/UPS source version 47
3.2.4 MIES/UPS source developed by Kempter *et al.* 48
3.2.4.1 MIES/UPS source of the nanocatalysis laboratory 50
3.2.4.2 Data acquisition 51
3.2.4.3 MIES/UPS post-detection data treatment 53
3.2.5 Auger Electron Spectroscopy (AES) 55
3.2.6 Hemispherical analyzer 55
3.2.7 TPD/TPR (temperature programmed desorption / reaction) 56
3.2.8 Molecular beam doser 57
3.2.9 Pulsed molecular beam reactive scattering (p-MBRS) experiments 57
3.2.10 Infrared-Reflective Absorption Spectroscopy (IRAS) 60
3.3 Transfer system 60
3.4 Three electrode setup 61
4 The effect of CO poisoning on the reactivity of small size-selected Pd_n clusters. 63
4.1 Experiments and results 63
4.1.1 TPR 63
4.1.2 p-MBRS (at isothermal conditions) 64
4.1.3 IRAS 67
4.2 Discussion 68
4.3 Conclusion 74
5 Microkinetic simulations of mole fraction dependent reactivity properties of size-selected Pd_{13} clusters 75
5.1 Results 75
5.1.1 Mole fraction dependent studies on size-selected Pd_{13} clusters 75
5.1.2 Micro kinetic simulations 78
5.2 Discussion 83
5.3 Conclusion 88
6 Adsorption studies of organic molecules on MgO films 89
6.1 Results 89
6.1.1 MgO characterization 89
6.1.1.1 Auger electron spectroscopy (AES) 89
6.1.1.2 MIES/UPS 90
6.1.2 Adsorption properties of benzene on MgO 92

6.1.2.1 UPS spectra of benzene adsorbed on MgO/Mo(100) 93
6.1.2.2 MIES spectra of benzene adsorbed on MgO/Mo(100) 94
6.1.3 Adsorption properties of cyclohexene on MgO 95
6.1.3.1 TPD studies 95
6.1.3.2 UPS spectra of various cyclohexene coverages on MgO/Mo(100) 96
6.1.3.3 MIES spectra of various cyclohexene coverages on MgO/Mo(100) 98
6.1.3.4 Work function changes extracted from MIES/UPS spectra 99
6.1.4 Adsorption properties of Trichloroethylene (TCE) on MgO 100
6.1.4.1 TPD spectra of various TCE coverages on MgO/Mo(100) 100
6.1.4.2 UPS spectra of various TCE coverages on MgO/Mo(100) 102
6.1.4.3 MIES spectra of various TCE coverages on MgO/Mo(100) 103
6.1.4.4 Work function changes extracted from MIES/UPS spectra 104
6.2 Discussion of adsorption studies of organic molecules on MgO/Mo(100) 105
6.2.1 Cyclohexene adsorption on MgO/Mo(100) 105
6.2.2 TCE adsorption on MgO/Mo(100) 107
6.3 Conclusions and outlook 109
7 Cluster under ambient conditions 112
7.1.1 Size control 112
7.1.2 Coverage control 113
7.1.3 Storage of deposited clusters under ambient conditions and in water 115
7.1.4 Cluster sample under electrochemical conditions 116
7.1.5 Deposition of cluster on glassy carbon 117
7.2 Discussion 119
7.3 Conclusion and outlook 120
8 Conclusions 121
9 Literature 124
10 Appendix 131
10.1 Acknowledgement 131
10.2 Statement 132
10.3 Curriculum Vitae 133

List of Figures

Figure 1.1 Energy diagram with respect to the reaction progress 1
Figure 2.1 Different surface states of a Pt(110) single crystal during CO oxidation 7
Figure 2.2 MO(Molecular Orbital)-scheme for CO adsorption on a d-metal 8
Figure 2.3 STM image of large facetted nanoparticles 10
Figure 2.4 Different possible interaction paths for a reactant that strikes from the gas-phase onto a metal oxide surface of a catalyst. 11
Figure 2.5 Illustration of a capture zone around a cluster. 13
Figure 2.6 Uniformly distributed clusters on the surface 14
Figure 2.7 Escape depth of photo-excited electrons with respect to the kinetic energy. 17
Figure 2.8 Different approaches for UPS experiments 19
Figure 2.9 Illustration of the Jellium model. 20
Figure 2.10 Energy diagram for a sample electrically connected with an analyzer 22
Figure 2.11 UPS spectrum of typical d-metal 25
Figure 2.12 Ejection of an electron described in the three-step model. 26
Figure 2.13 Transition via absorption illustrated in a dispersion relation. 27
Figure 2.14 Vector model describing the escape of the excited electron through the surface. 30
Figure 2.15 Symmetry analysis of a clean MgO surface. 33
Figure 2.16 Symmetry analysis for deposited clusters. 33
Figure 2.17 Different interaction paths for the dexcitation of a metastable atom on a surface 35
Figure 2.18 Illustration of the AD process 36
Figure 2.19 Illustration of RT process followed by an AN. 38
Figure 2.20 Illustration of a RT followed by either an AU (left) or an AD (right) 40
Figure 3.1 The experimental setup can be divided into three compartments. 42
Figure 3.2 Sample holder with three crystals. 44
Figure 3.3 E-gun as it is attached to the vacuum chamber 45
Figure 3.4 The different domains of a DC glow discharge 47
Figure 3.5 First MIES source. 48
Figure 3.6 MIES/UPS source with two discharges developed by Kempter *et al.* 49
Figure 3.7 Principle of TOF separation. 49
Figure 3.8 Improved source of the nanocatalysis laboratory. 50
Figure 3.9 Scheme of the data acquisition of the different electron spectroscopic methods ... 52

Figure 3.10 Screenshot of the data treatment program interface. 54
Figure 3.11 Sketch of a pulsed valve. 58
Figure 3.12 Sketch of the continuously pumped gas reservoir system 59
Figure 3.13 IRAS setup used in the nanocatalysis laboratory..... 60
Figure 3.14 A typical three-electrode setup with is corresponding electric circuit diagram ... 62
Figure 3.15 Voltage drop appearing between two electrodes in an electrolyte 62
Figure 4.1 TPD spectra of the two different procedures described in the text..... 64
Figure 4.2 Representative CO_2 pulses..... 65
Figure 4.3 Pulsed molecular beam experiments of various cluster sizes 66
Figure 4.4 Spectra of CO adsorbed on Pd_{13} clusters annealed to different temperatures 67
Figure 4.5 Comparison of time dependent CO_2 signals of an oxygen precovered Pd(111) single crystal and size-selected Pd clusters 69
Figure 4.6 Comparison of maximum CO_2 rate determined for a Pd(111) single crystal with the integrated CO_2 of size-selected clusters 70
Figure 4.7 Time dependent CO_2 signal detected for a CO precovered Pd(111) single crystal and size-selected Pd clusters 71
Figure 4.8 Temperature regimes for CO poisoning and oxygen activation. 72
Figure 4.9 TPR spectrum of Pd_{13}. 72
Figure 4.10 Temperature regimes for CO poisoning and oxygen activation on Pd clusters.... 73
Figure 5.1 A typical CO_2 pulse recorded in mole fraction dependent measurements. 76
Figure 5.2 *TOF* and *RP* obtained for Pd_{13} clusters in mole fraction measurements 77
Figure 5.3 Mole fraction dependent *TOFs* and *RPs* obtained for a single crystal model 81
Figure 5.4 Mole fraction dependent *TOFs* and *RPs* obtained for a supported cluster 83
Figure 5.5 Comparison of the experimental *TOFs* and the single crystal model..... 83
Figure 5.6 Comparison of the experimental *RPs* and the single crystal model. 84
Figure 5.7 Comparison of the *TOFs* simulated for a single crystal and a supported cluster ... 85
Figure 5.8 Comparison of the *RPs* simulated for a single crystal and a supported cluster 86
Figure 5.9 Comparison of the experimental *TOFs* and simulated for a supported cluster 86
Figure 5.10 Comparison of the experimental *RPs* and simulated for a supported cluster 87
Figure 6.1 Typical Auger spectra recorded for a clean Mo(100) and a MgO film 90
Figure 6.2 UPS and MIES spectra recorded and literature spectra..... 91
Figure 6.3 UPS spectra of benzene adsorbed on MgO and literature spectra..... 93
Figure 6.4 MIES spectra of benzene adsorbed on MgO and literature spectra..... 94
Figure 6.5 TPD spectra of different cyclohexene coverages on MgO. 95

Figure 6.6 UPS spectra of different cyclohexene coverages on MgO 96
Figure 6.7 UPS spectra of different cyclohexene coverages on MgO 97
Figure 6.8 MIES spectra of different cyclohexene coverages on MgO 98
Figure 6.9 MIES spectra of different cyclohexene coverages on MgO 98
Figure 6.10 Change in the WF for increasing cyclohexene surface concentration 99
Figure 6.11 TPD spectra of different TCE coverages on MgO 100
Figure 6.12 Integrated ion signal plotted for different dosages. 101
Figure 6.13 UPS spectra of different TCE coverages on MgO 102
Figure 6.14 UPS spectra of different TCE coverages on MgO 102
Figure 6.15 MIES spectra of different TCE coverages on MgO 103
Figure 6.16 MIES spectra of different TCE coverages on MgO 104
Figure 6.17 WF change for increasing TCE surface concentrations 105
Figure 6.18 Assumed four step adsorption model for TCE on MgO 108
Figure 6.19 Spectra of different unselected Pd cluster coverages 110
Figure 6.20 Same spectra of different unselected Pd cluster coverages 110
Figure 7.1 TEM images and their corresponding histograms 113
Figure 7.2 TEM images of different deposition times 114
Figure 7.3 A typical cluster sample after transfer to ambient conditions 115
Figure 7.4 TEM images taken before and after a electrochemical treatment 116
Figure 7.5 CO-stripping experiment performed for Pt clusters and Pt single crystal 117
Figure 7.6 Cluster coverage determined via integration of the cluster neutralization current and CO stripping signal plotted with respect to each other 118

Flow chart

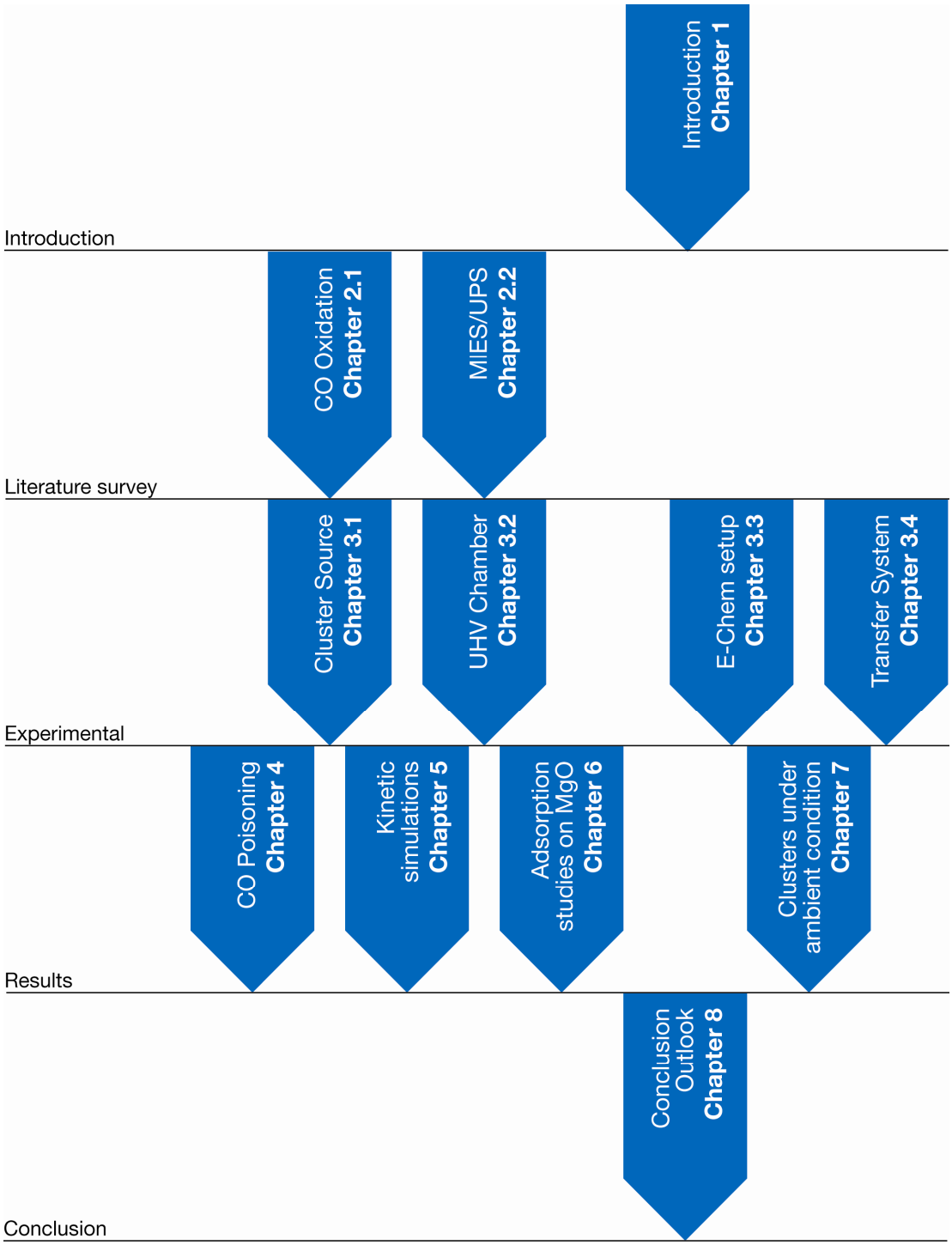
Introduction
Introduction Chapter 1
Literature survey
CO Oxidation Chapter 2.1
MIES/UPS Chapter 2.2
Experimental
Cluster Source Chapter 3.1
UHV Chamber Chapter 3.2
E-Chem setup Chapter 3.3
Transfer System Chapter 3.4
Results
CO Poisoning Chapter 4
Kinetic simulations Chapter 5
Adsorption studies on MgO Chapter 6
Clusters under ambient condition Chapter 7
Conclusion
Conclusion Outlook Chapter 8

1 Introduction

The effect of catalysis has been defined by Ostwald as follows: “A catalyst is a substance that accelerates a chemical reaction, without being changed by the reaction and without changing the final location of the thermodynamic equilibrium of that reaction.”[1]

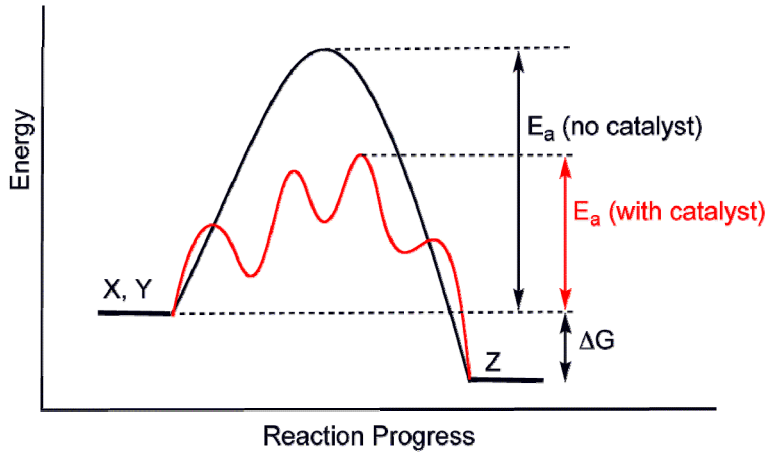

Figure 1.1 Energy diagram with respect to the reaction progress. The black curve describes the reaction path without, the red curve the path with a catalyst. The activation barrier is lowered for the catalyzed reaction. Note: thermodynamics remains unaltered.

As seen in Figure 1.1 the usage of catalysis lowers the activation barrier and reduces the demand of energy, which needs to be applied in order to perform a chemical reaction.[2, 3] Since energy losses can occur during a chemical conversion, catalysis is of great interest for large industrial as well as laboratorial applications, because lower energy demands needed for a reaction to happen, reduces energy losses, too.

The three major catalysis subareas are: Homogeneous, heterogeneous and bio-catalysis. Homogeneous and bio-catalysts exhibit extremely high reactivity and selectivity.[4] In comparison, the reactivity of heterogeneous catalysts are usually lower and less specific. However, they maintain stable under extreme conditions and are easy separable, since the catalyst can be filtered off from the reaction mixture afterwards. Nevertheless, a detailed understanding of catalysis in order to achieve systematic investigations and developments is still a key issue for both, the scientific and industrial community.

For heterogeneous catalysis single crystal studies under ultra high vacuum (UHV) conditions have formed the fundament of catalysis research.[5] The use of UHV enabled the

application of techniques, such as electron diffractometry as well as electron spectroscopy, since the mean free path is increased by around 14 orders of magnitude in comparison to ambient conditions.[6]

Low energy electron diffraction (LEED) was successfully applied to single crystals in the 1960's and one gained much important information regarding the adsorption properties of reactants like e.g. CO, hydrogen or oxygen on metal surfaces.[7-9]

By means of Auger electron spectroscopy (AES) and X-ray photoelectron spectroscopy (XPS) information about core-electrons and their shifts in binding energy with respect to the chemical environment of the probed atoms can be obtained.[10, 11] Even more interesting are surface sensitive methods such as ultraviolet photoelectron spectroscopy (UPS), metastable impact electron spectroscopy (MIES) or photoelectron spectroscopy of adsorbed Xe (PAX spectroscopy).[12-14] The use of these methods gives access to information about the valence structure of a given surface.[15]

The successful application of the above mentioned experimental methods has given detailed insights into catalytic mechanisms of simple reactions on single crystals like CO oxidation or ammonia synthesis.[16] Patents have been developed for industrial catalysts based on single studies and the importance of this pioneering work has been honored by the Nobel Prize in 2007 for G. Ertl.[17-19]

It is well-known that an industrial applicable catalyst consists of dispersed metal particles on a chemically inert support like carbons or metal oxides. A detailed comparison with single crystals shows that many effects must be considered for industrial catalysts which are not relevant for single crystals. Hence, these model systems are not sufficient for a complete understanding of effects such as: the stability of the metal particles on the support, particle shape, electronic effects, dispersion, reactant spill-over or reverse spill-over effects.[20-24] Furthermore, it has been shown that the size of the metal particles has an influence on the catalytic properties.[25] Especially interesting in that respect is the behavior of gold, which shows catalytic activity exclusively for small particles.[26, 27]

To overcome the shortcomings of single crystal studies, different methods have been developed and applied for the preparation of metal particles on metal oxide or carbon supports. One of the most important and promising approach for UHV studies is physical vapor deposition (PVD).[28-30] A given metal is evaporated onto the support material which is subsequently annealed. By controlling the annealing temperature of the sample the

particle growth is influenced. The nucleation of the atoms, leading to particle formation, depends furthermore on the support, the metal, the defect concentration on the surface and the vacuum conditions.[31] The particles synthesized by means of PVD have been characterized extensively in the past using Transmission Electron Microscopy (TEM) and Scanning Tunneling Microscopy (STM).[30, 32, 33]

Furthermore, reactivity studies have been performed for CO oxidation, decomposition of methanol, oxidation of methanol and NO-CO reactions.[34-36] Results like a less pronounced CO poisoning effect for smaller particles in comparison to larger particles and single crystals have already shown the importance of those systems for advanced catalysis research.[37]

Nevertheless, there are some limitations of the PVD methodology. A main disadvantage is that the coverage can not be controlled independently from the choice of the particle size. Furthermore, the size distribution is difficult to control and the exact nucleation conditions are rarely reproducible.[31]

In order to overcome these problems the deposition of gas-phase clusters under soft-landing conditions has been developed as a another technical method to prepare metal particles on a given support.[38] A main advantage of this method is that the size and size distribution of the cluster beam can be precisely controlled by using a quadrupole mass-spectrometer (QMS) before deposition onto the support. Additionally, since the particles are formed in the gas-phase and subsequently deposited, the coverage can be independently controlled with respect to the size.[39] Deposited mass-selected clusters have already shown great potential as model catalysts, e. g. the influence of the size of gold clusters on their electronic structure and their catalytic properties.[26] Another interesting result is the successful application of the non-reactive reverse spill-over model for CO oxidation on small palladium clusters under quasi steady-state conditions.[40]

A further advantage of cluster deposition is that the electronic structure of gas-phase clusters can be determined experimentally and verified theoretically.[41, 42] Consequently, theoreticians use this “bottom up” approach to develop new theoretical models in order to explain phenomena in catalysis like charging effects of the clusters or structural dynamic fluctuations.[43-45]

However, there is still a lack of information about the electronic structure of small metal clusters on support materials. Recently, an XPS study of mass-selected palladium clusters

on TiO_2 has been published, which shows a correlation between a shift of the 3d electrons binding energies with respect to size in a range of 0.3 eV and the reactivity of those small size-selected clusters for CO oxidation.[46] It is worth mentioning that the catalytic reactivity has been determined by means of TPR, which is not a suitable method to determine catalytic reactivity, because no stationary conditions (constant temperature, constant reactant flux) are achieved in a TPR experiment.

Although XPS can be applied to probe clusters the use of photons in the X-ray range leads to a limited surface sensitivity.[47] Another disadvantage is that XPS probes core electrons; catalysis and reactivity are, however, determined by the valence electron structure.

Another open question is the relevance of clusters for catalysis research under catalytically relevant conditions. For this approach cluster samples have to be transferred out of UHV to ambient conditions, which has been recently done recently by Kappes et. al.. Mass-selected gold clusters ($n = 10 – 20$) were deposited onto carbon TEM grids and the longtime stability of these very small clusters has been investigated by means of transmission electron microscopy. Coalescence was proven to occur after several days.[48]

A different possibility to achieve size-selection with a broader size distribution is the application of a quadrupole deflector as a size-selecting unit. Using this approach a size distribution in the range of 2-3 nm was reported, recently.[49] However, catalytic studies of transferred clusters samples and their stability under reactive conditions have yet to be performed.

In conclusion, it can be stated that deposited clusters exhibit high potential for catalysis research. However, there are still many problems in cluster catalysis research, like catalytic reactivity determination, electronic structure, or stability and characterization under ambient conditions. The aim of the presented work is to make a contribution to overcome some of these problems that still limit the full investigation and application of clusters in catalysis research.

2 Literature survey and theoretical background

The scope of the presented PhD thesis was to investigate the following three different topics:

1. CO oxidation properties of small size-selected palladium clusters. Experimental and theoretical studies.
2. Implementation and characterization of a MIES/UPS source in an existing UHV setup (nanocatalysis setup) as a surface sensitive electron spectroscopy.
3. Transfer of deposited clusters to ambient conditions, stability studies and electrochemical catalytic testing.

In the following a brief introduction about the theoretical background to each of these topics is given.

2.1 CO oxidation

2.1.1 General remarks

The conversion of CO to CO_2 is probably the most investigated reaction in heterogeneous catalysis. It plays a significant role in industrial as well as scientific research and is a key reaction in the cleaning process of exhaust from hydrocarbon combustion.[50,51] In scientific research it attracted many groups to explore the catalytic conversion catalyzed by transition metals in order to enhance the understanding of heterogeneous catalysis. Due to its simplicity (equation 2.1) with respect to its selectivity it allowed detailed studies on mechanistic details of the reaction.

$$CO + \frac{1}{2} O_2 \rightleftarrows CO_2 \qquad (2.1)$$

For a long time it was discussed whether this reaction, catalyzed by group VIII metals (e.g Pd or Pt) follows an Eley-Rideal or a Langmuir-Hinshelwood mechanism. The two mechanisms differ in the way the reactants are adsorbed during the reaction.

In an Eley-Rideal mechanism (equation 2.2) one of the two reactants (A) adsorbs on a specific site (*), whereas the second one (B) is still in the gas-phase. The reaction occurs if a gas-phase reactant B hits an adsorbate complex (A*). A product (C) is formed which is still adsorbed (C*). The final step of the reaction involves desorption of the product molecule back into the gas-phase.

$$A^* + B_{gas} \rightleftarrows C^* \rightarrow C_{gas} \tag{2.2}$$

In the Langmuir-Hinshelwood (equation 2.3) mechanism both reactants must be adsorbed in order to react with each other. The product C is formed and subsequently desorbs into the gas-phase.

$$A^* + B^* \rightleftarrows C^* \rightarrow C_{gas} \tag{2.3}$$

2.1.2 Oxygen dissociation during CO oxidation

The dissociation of oxygen was clearly shown to be a relevant step in determining the reactivity of a given catalyst for most metals, except for gold.[52] First, based mainly on steady-state rate measurements, it was suggested that the reaction occurs via an Eley-Rideal mechanism. However, it is well-know that mechanistic details cannot be gained from rate laws derived from steady-state rates. Reactions must instead be performed in transient regimes. This has been shown by Eigen, who developed the relaxation method for kinetic studies.[53]

Using this approach in molecular-beam experiments it was first demonstrated in 1978 that CO oxidation catalyzed by Pd follows a Langmuir-Hinshelwood mechanism.[54] The Langmuir-Hinshelwood mechanism was later proven for other group VIII metals like platinum, too.[55] The investigation of CO oxidation on group VIII metals also led to findings of other distinctive aspects not known to occur in heterogeneous catalysis before, like the appearance of kinetic oscillations.[56] Although this phenomenon had been shown for industrial catalysts, for the first time, single crystal studies were necessary to explain the origin of this property.[57, 58]

Depending on the metal, different driving forces were found to be responsible for the oscillations.

On platinum (100) and (110) it was shown, that a reconstruction of the surface induces the appearance of a bistability. As an example, for a Pt(110) single crystal the surface structure changes from a 1 x 2 structure with an oxygen sticking coefficient of $S_{O2} \approx 0.3 - 0.4$ to a 1 x 1 structure with an oxygen sticking coefficient of $S_{O2} \approx 0.4 - 0.6$ upon CO adsorption.

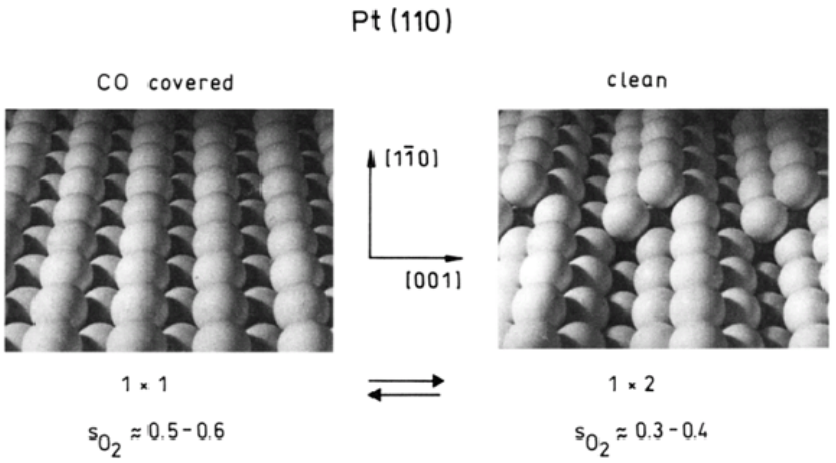

Figure 2.1 Different surface states of a Pt(110) single crystal during CO oxidation. Depending on the CO coverage of the surface the oxygen sticking varies from 0.5-0.6 on a CO precovered surface to 0.3-0.4 in a clean surface.[56]

Starting with a CO covered 1 x 1 phase, the adsorption rate of oxygen, hence the catalytic activity, will be high.[59] Consequently, more adsorbed CO will be consumed in the reaction than being adsorbed, leading to a decrease in CO coverage. When a certain value is reached, the surface will reconstruct into the 1 x 2 phase. As previously mentioned, the oxygen sticking coefficient is low on this surface yielding in an increasing CO coverage, which then induces a reconstruction back to the 1 x 1 phase, when a distinctive coverage is reached (see Figure 2.1). For constant reaction fluxes the system will, hence, oscillate between those two states.[60]

For palladium single crystals it was shown that the oscillations are not related to any reconstruction effects, because the adsorption of oxygen on palladium is not structure sensitive. The appearance is explained by the filling and depletion of a subsurface oxygen reservoir which is associated with a deactivation and activation of the model catalyst.

Starting with an active oxygen-covered surface, oxygen begins to penetrate into the subsurface region, leading to a deactivation of the surface. The oxygen sticking coefficient decreases, leading to an increase in the CO coverage. The excess surface concentration of CO depletes the oxygen reservoir and a reduced palladium surface is formed upon reaction. The formed clean phase shows a higher oxygen sticking coefficient and thus, exhibits a high oxidation affinity.[61]

2.1.3 CO poisoning

Another mechanistic detail to be mentioned is the CO poisoning effect. It is well-known that CO adsorbs molecularly on group VIII metals, with the carbon atom pointing to the metal surface and exhibiting a strong interaction.[62] The adsorption can be described on a molecular level using the Blyholder model. This model describes the bond between CO and a metal based on the interaction of the highest occupied molecular orbital (HOMO) and the lowest unoccupied molecular orbital (LUMO) of CO with the electronic band of the metal.[63] The 5σ orbital, which is the HOMO, forms a bond by a metal forward donation (electron density is transferred from CO to the metal), whereas the 2π*, which is the LUMO, forms a back-bond (electron density is transferred from the metal to CO).

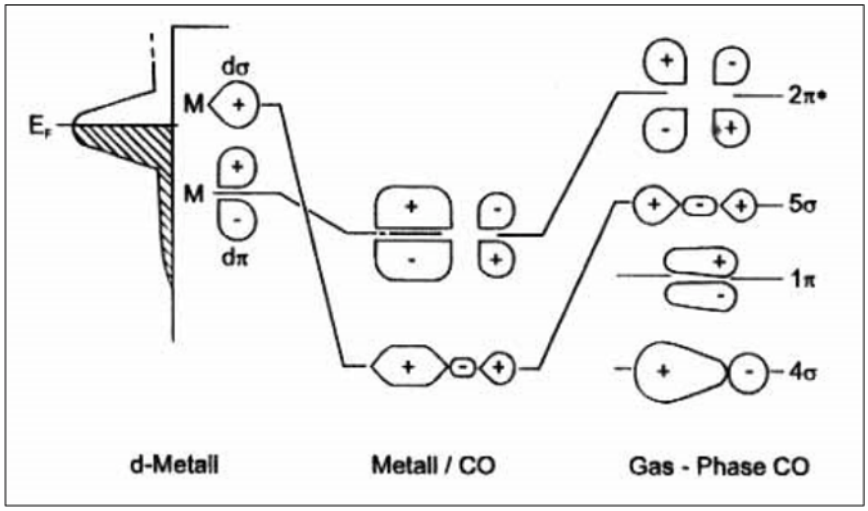

Figure 2.2 MO(Molecular Orbital)-scheme for CO adsorption on a d-metal. On the left side the electronic structure of a d-metal is illustrated on the right side the MO-scheme of CO in the gas-phase. The interaction between CO and the surface leads to a stabilization of the d-metal band and the 5σ as well as the antibonding 2π* CO orbitals. Filling of the antibonding 2π* orbital leads to a destabilization of the CO bond. **[63]**

In the Blyholder model the strength of the bond is mainly determined by the π-back donation. This charge transfer strengthens the metal-C bond, however, the C-O bond is weakened, because the anti-bonding orbital becomes more populated as can be seen in Figure 2.2.

On (111) surfaces three different adsorption configurations can be distinguished: on-top (one-fold), bridge-bonded (two-fold) and three-fold.[64] Similar to coordination chemistry, the back-donation strengthens with increasing coordination number.[65] Hence, the following bonding strength order is expected: On-top (one-fold) < bridge-bonded (two-fold) < three-fold.[66]

Although lateral interactions between the adsorbed CO molecules have to be taken into account, the above described rule holds for many metals and is a very useful tool to explain Infra-Red-spectra (IR) of CO adsorbed on metals. Since the C-M strength is inverse to the C-O bond, it can be concluded, that a low C-O stretching frequency relates to a strong C-metal bond.[67]

The adsorption strength of CO on a given metal is one of the two key points determining the reactivity of a metal catalyst; the aforementioned dissociation of oxygen being the second. It has been shown that a surface covered with CO blocks the surface for oxygen adsorption. If no oxygen is able to reach the surface, it cannot become activated via dissociative adsorption, even if the temperature would allow for activation. For palladium the oxygen dissociation occurs around 200 K and CO adsorbs strongly up to temperatures of 450 K. Hence, the reactivity is limited in this temperature regime by CO on the catalyst surface.[68] The same observations hold for platinum, as well.[69]

However, one has to ask if the properties of a metal-particle differ from those of a single crystal. A detailed study on the CO oxidation of nanoparticles prepared via physical vapor deposition (PVD) has shown that for large facetted particles similar catalytic properties are observed to those of single crystals. This can be attributed to their surface morphology, which is dominated by a 111 facets as seen is from an STM image (Figure 2.3) of those particles.[70]

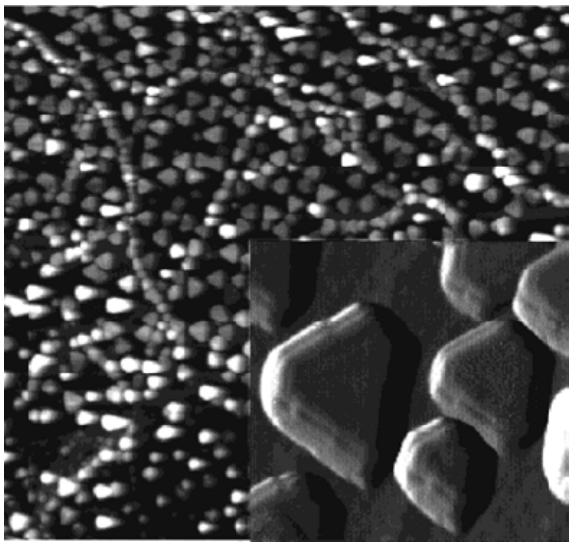

Figure 2.3 STM image of large facetted nanoparticles exhibiting a size of 2700 atoms / particle.[70]

Surprisingly, it could be shown at the same time that for smaller particles, prepared via physical vapor deposition, without clearly assignable facetted areas, the CO poisoning effect is shifted to lower temperatures.[71]

2.1.4 Support effects

An important difference between small metal clusters and larger nanoparticles in comparison to singles crystal is the support. Depending on the support material the properties of catalysts can change. The chemical properties of the support material have been shown to influence the stability of small metal particles.[72] Furthermore, the electronic structure of the support material has an influence on the electronic properties of the particles and their morphology.[73]

Another support effect not originating from chemical or electronic support influences is the spill-over of reactants.[74] It has been shown for hydrogenation reactions on supported platinum particles, that hydrogen is activated via dissociative adsorption. The formed atomic hydrogen diffuses from the particle to the support and reacts with the second reactant on the support surface. This phenomenon is called spill-over, because it describes the diffusion of activated reactants onto the support. The opposite case, that reactants adsorb on the support and diffuse to the particles deposited onto the support surface, has also been shown.

Here an introduction to the occurring mechanism on metal oxides, as they are usually applied as catalyst support materials, is given. The heat of adsorption of oxygen on metal oxides is known to be very small (< 0.1 eV), whereas CO exhibits a higher heat of adsorption (< 0.4 eV e. g. on MgO, Al_2O_3), leading to a much longer life time of CO on metal oxides in contrast to oxygen.[75-77] The different scenarios that can occur for CO molecules striking from the gas-phase onto a metal oxide based catalysts are illustrated in Figure 2.4.

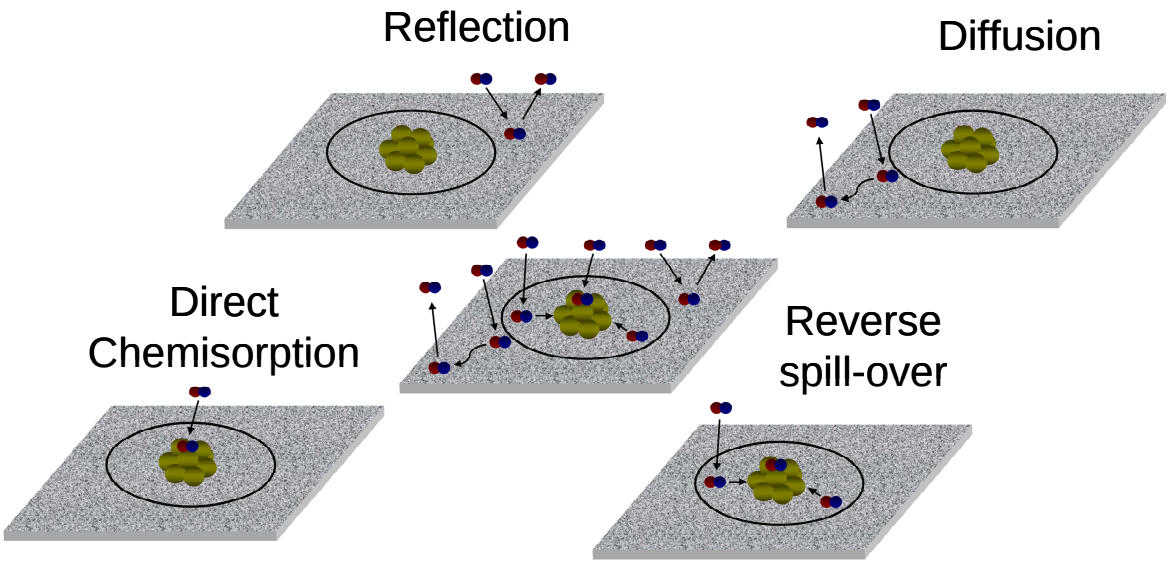

Figure 2.4 Different possible interaction paths for a reactant that strikes from the gas-phase onto a metal oxide surface of a catalyst.

Molecules striking onto a surface can either adsorb or be reflected. The chance of adsorption is described by the sticking probability that can be measured by means of molecular beam experiments.

The situation is, however, more complex for a catalyst consisting of supported metal clusters, because the reactants can either adsorb on the clusters or on the support as seen in Figure 2.4. If the reactants adsorb directly on a cluster the term “direct chemisorption” is used, because the reactants usually exhibit a high heat of adsorption on a transition metal cluster. If the reactants adsorb on the support they can diffuse over the support surface. Depending on their life-time they can either desorb or diffuse to a cluster leading to “indirect chemisorption”. The mechanism of indirect chemisorption is called “reverse spill-

over" or more explicit "non-reactive reverse spill-over". This takes into account that the reactant is not modified, in contrast to the aforementioned spill-over of hydrogen proceeding via dissociative adsorption .[43]

Two different models have been investigated in the past in order to describe the effect of reverse spill-over. Since MgO was the support of choice in the presented work and palladium metal clusters the catalytic reactive species, the following relations of the two different models will be formulated for Pd clusters, supported on MgO.

In the first model it was assumed that every CO molecule that adsorbs on the support close to a cluster will be chemisorbed, if the distance to a cluster is less than the mean diffusion lengths, a molecule can travel across the surface.[78] In order to determine the mean traveling distance X_s, the diffusion coefficient D and the lifetime τ of the molecule on the surface are defined as:

$$D = \nu \left(\frac{a^2}{4} \right) \exp\left(-\frac{E_{diff}}{RT} \right) \tag{2.4}$$

$$\tau = \nu^{-1} \exp\left(-\frac{E_{des}}{RT} \right) \tag{2.5}$$

The frequency factor ν is assumed for simplification to be equal for both, adsorption and diffusion; a is the diffusion hopping distance that takes the distance between two adsorption sides into account[1]. E_{diff} is the activation energy for diffusion and E_{des} the activation barrier for desorption, which equals the adsorption energy for the case of physisorption, since physisorption does not exhibit an activation barrier for the process of adsorption. Combining equation 2.4 and 2.5 one can derive the mean traveling distance X_s:

$$X_s = \sqrt{D\tau} = a \cdot \exp\left[\left(E_{ads} - E_{diff} \right) / 2 N_A k_B T \right] \tag{2.6}$$

[1] a is set to 0.4 nm in the case of MgO.

A capture zone is defined as follows: Every molecule that adsorbs on the support close to a cluster with a distance less than X_s to a neighboring cluster will diffuse to the cluster and chemisorb (see Figure 2.5).

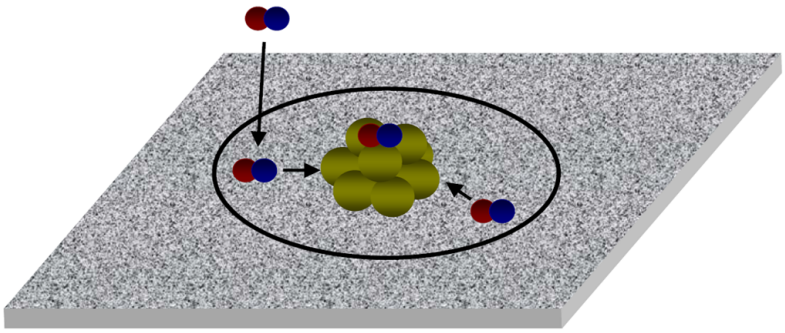

Figure 2.5 Illustration of a capture zone around a cluster. In this model the radius of the capture zone is defined exclusively by the diffusion length of the reactant on the surface.

Finally, the reactant flux can be formulated as the sum of a direct flux that takes direct chemisorption into account and a diffusion flux that takes the CO flux into account, which adsorbs in the capture zone.

$$F_{CO} = F_{dir} + F_{diff} = \alpha_{Pd}\pi R^2 J + \alpha_{MgO} J\pi\left[\left(R + X_S\right)^2 - R^2\right] \qquad (2.7)$$

α_{Pd} and α_{MgO} are the sticking probabilities of CO on palladium (≈ 1) and MgO (≈ 0.5); J is the total reactant flux per surface area and R the cluster diameter. The model allows the determination of the total CO flux reaching a cluster.

The second model, which has been developed by Henry *et al.* uses a different approach by applying the diffusion equation.[79] Three assumptions are made for this model:

1. The clusters are uniformly distributed over the surface.
2. A circular area of a radius of L is defined around each metal cluster, determining a diffusion cell equal in size for each cluster (see Figure 2.6).
3. Using the diffusion equation, the diffusion of the CO molecules on the support surface is taken into account.

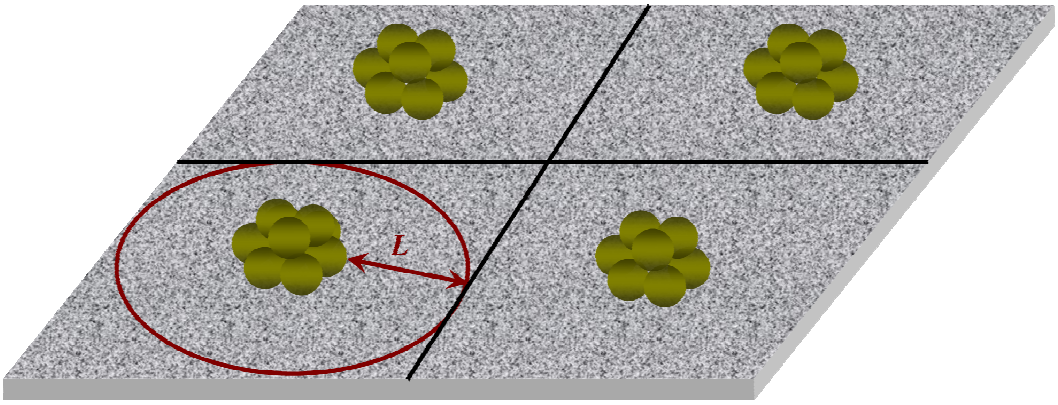

Figure 2.6 Uniformly distributed clusters on the surface. The black lines illustrate the diffusion cells that are defined in the model developed by Henry *et al*.

The surface concentration of CO molecules with respect to the time is as follows:

$$\frac{\partial N(r,t)}{\partial t} = \alpha_{MgO} J + D\left[\frac{\partial^2 N(r,t)}{\partial r^2} - \frac{1}{r}\frac{\partial N(r,t)}{\partial r}\right] - \frac{N(r,t)}{\tau} \qquad (2.8)$$

The first term $\alpha_{MgO} J$ includes the total amount of CO that adsorbs on the MgO surface. The second term is the diffusion equation in polar coordinates, which describes the diffusion of the reactants to the clusters. The last term takes the limited lifetime of CO on the surface into account.

In order to solve this mathematical problem, which is a second order differential equation, three assumptions have to be made:

1. Clusters are perfect sinks for CO → $N(R) = 0$
2. Steady state conditions → $dN/dt = 0$
3. No net flux across the boundary of each diffusion cell → $dN(L)/dr = 0$

The first point holds only if the reaction probability of CO is 1. This is fulfilled for CO combustion performed at temperatures above the CO poisoning limit, because then every oxygen molecule that hits a cluster is activated and therefore under these conditions they are oxygen saturated.

Stationary conditions have to be achieved to ensure that constant diffusion profiles are formed. Thus, the model holds only for experiments performed under steady state conditions.

The last point is a consequence of the assumption that the clusters are uniformly distributed. All clusters are treated equally and so they exhibit the same reactivity. This leads to the fact that no net flux between the diffusion cells can occur.

Finally the diffusion flux to the clusters can be described using Fick's first law:

$$F_{diff} = -2\pi RD\frac{\partial N(r,t)}{\partial r} = 2\pi RX_S aJP(R/X_S, L/X_S) \tag{2.9}$$

P is a term that includes the Bessel functions I_n and K_n, which are necessary to solve the differential equation:

$$P(x,y) = \frac{I_1(y)K_1(x) - I_1(x)K_1(y)}{I_0(x)K_1(y) + I_1(y)K_0(x)} \tag{2.10}$$

The flux can than be described as in the first case using a direct and a diffusion flux:[80]

$$F_{tot} = F_{direct} + F_{diffusion} = \alpha_{global} J \tag{2.11}$$

Furthermore, a new coefficient called global sticking coefficient α_{global} is defined in equation 2.11. The total flux reaching the surface is corrected by this coefficient yielding in the total amount of CO that reaches the cluster.

A major difference between the two models is that the second model assumes a net flux to the cluster, whereas in the first model it is assumed that every CO molecule diffuses directly to a cluster. Consequently, a concentration gradient is built up during the reaction in the second model, because the clusters are assumed to be perfect CO sinks. This forces the CO molecules to diffuse to the clusters. However, this does not mean that every molecule adsorbing in the capture zone will diffuse to the cluster, as it is assumed in the first model. Every molecule is diffusing individually, only the net flux points towards the

direction of the clusters. This is a real improvement, compared to the first model, where one has to assume that the cluster exhibits an attractive potential that forces every CO molecule to diffuse to the cluster. One should be aware that this kind of attractive force has a very limited range and thus it should be negligible for a diffusion length in the range of a few nanometers.

It has been shown that the second model developed by Henry shows better accordance with experimental CO oxidation rates, measured for palladium nanoparticles, than the first model. Additionally, the model holds also for smaller systems, as it has been successfully applied by Heiz *et al.* for small size-selected palladium clusters.

Finally, it should be discussed if and under which conditions the two models fail. For the first model this is the case when the capture zones of the individual clusters start to overlap, because then a certain molecule can diffuse to different clusters.

The second model behaves differently, because the explicit concentration profile is calculated, allowing the individual molecule to diffuse to different clusters and so the model does not fail for increasing coverages in comparison to the first. It is also noteworthy that the assumption of a reaction probability of 1 does not hold for every case.

2.2 Ultraviolet photoelectron spectroscopy (UPS)/ Metastable impact electron spectroscopy (MIES)

2.2.1 Ultraviolet photoelectron spectroscopy (UPS)

In the field of photoelectron spectroscopy (PES) techniques, UPS is defined as a spectroscopic method in which photons in the energy range of 10 to 100 eV (UV radiation) are used to eject electrons from a given surface. In Figure 2.7 the mean free path of an electron in a solid state body with respect to the energy of the electron is shown.[47]

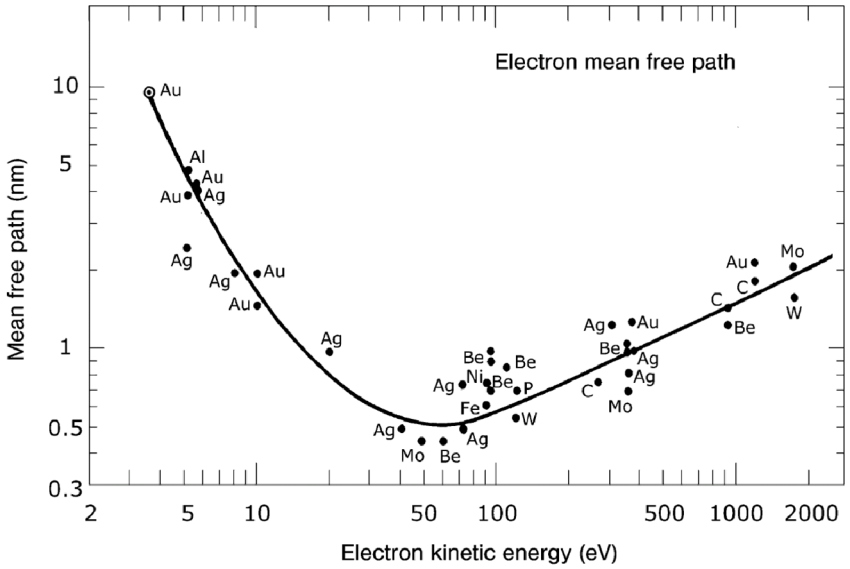

Figure 2.7 Escape depth of photo-excited electrons with respect to the kinetic energy. A minimum occurs in the range of UV radiation.[6]

It can be seen that the curve exhibits a minimum in the range of ultraviolet photo electrons (≈ 50 eV). Hence, UPS is a surface sensitive method in contrast to XPS (use of X-ray radiation: Al K_α, $h\nu$ = 1486,6 eV und Mg K_α, $h\nu$ = 1253,6 eV), because the probed electrons have an escape depth of 2-3 layers.

In the presented work a MIES/UPS source (He discharge lamp) is applied, which emits photons with an energy of 21.22 eV (He I).[81] At these low UV exciting energies, photo emission is exclusively limited to valence electrons. Thus, it allows probing the electronic structure and bonding of the surface as well as changes in electronic levels due to the presence of adsorbates.[6, 82]

From UPS spectra the density of states (DOS), more precisely a convolution of the densities of unoccupied and occupied states which are therefore referred to as the Joined Density of States (JDOS) can be extracted.[83] Further details about the different experimental possibilities are given in the next section. It should also be stressed that UPS allows the determination of the macroscopic work function, which is a characteristic material constant.

2.2.1.1 Basic principle of photoelectron spectroscopy (PES)

Photo electron spectroscopic methods are based on the photoelectric effect, which describes the emission of electrons, due to the absorption of electromagnetic waves, by a given material. The kinetic energy E_{kin} of the emitted electrons is defined as,

$$E_{kin} = h\nu - \phi \tag{2.12}$$

with $h\nu$ as the excitation and ϕ as the work function of the bulk material.
The emission of photo electrons can be described using a three step model:[84, 85]

1. An electron absorbs a photon of a given energy and consequently the electron is excited.
2. The excited electron diffuses to the surface.[1]
3. Emission of the excited electron from the surface into the vacuum to a point at which the surface ceases to influence the electron.

A detailed mathematical formulation will be given in section 2.2.1.5. UPS experiments can be performed in three different ways leading to three different results: Energy Distribution Curve (EDC), Constant Final State (CFS) and Constant Initial State (CIS).

[1] If the diffusion occurs without any inelastic collision the electron is assigned as a primary electron. If the electron suffers an energy loss due to inelastic scattering processes, the electron is assigned as a secondary electron. Since primary electrons carry the correct energy information in contrast to the secondary, the aim in PES is to maximize the yield of primary electrons, while the amount of secondary electrons should be minimized

The EDC is recorded in experiments in which the excitation energy is kept constant (fixed wavelength) and the final state (energy of the analyzer) is varied. The disadvantage of this method is that the detected intensity and thus the outcome of the experiment depends on both, the initial and the final state of the excited electrons. Due to this reason the recorded spectra are called the JDOS (see Figure 2.8 a).[47]

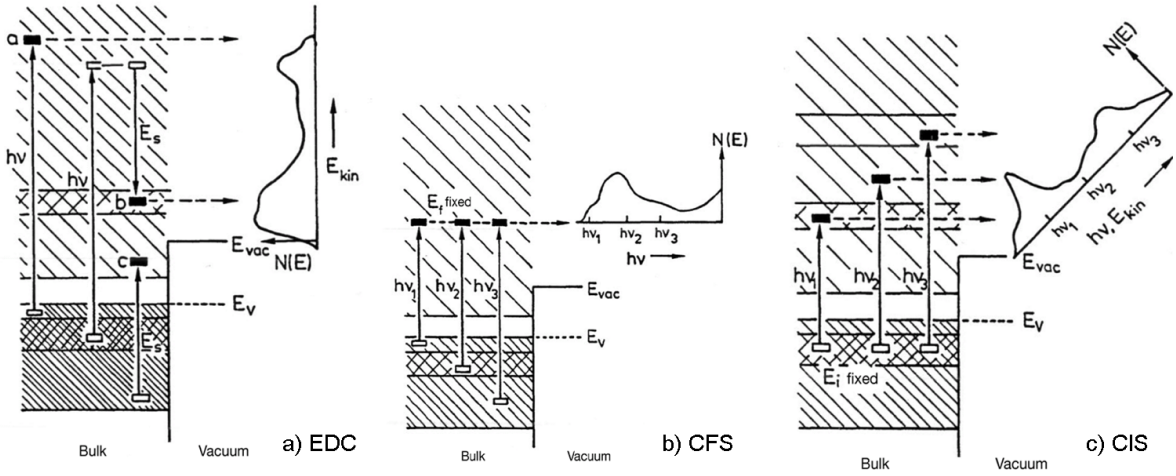

Figure 2.8 Different approaches for UPS experiments. The left part (a) illustrates detection of a spectrum at a constant excitation energy while the analyzer energy is scanned. Different initial and finial states are probed. Spectrum b) in the middle shows a spectrum detected for a constant final state. The analyzer energy is kept constant and the excitation energy is varied. The right part (c) illustrates how a spectrum for a fixed initial state can be recorded by varying the excitation energy and the analyzer energy.[47]

In the second approach, (see Figure 2.8 b) the kinetic energy of the photo electron is kept constant and the excitation energy is changed. Thus, the final state is fixed (CFS) and only the initial state is probed.

In the third case, the excitation energy and the energy at which the analyzer detects the photo electrons is varied, in a way that the energy difference between those two is kept constant as seen in the right part of Figure 2.8 c. In this experiment the initial state is fixed and so the method is called CIS. It should be mentioned that case two and three can only be achieved using synchrotron-radiation, as the excitation energy has to be tuned.[47]

The setup of the nanocatalyis laboratory is limited to the first case in which the excitation energy is constant and the analyzer energy is varied. The experiments preformed in this work are thus limited to the determination of the JDOS.

2.2.1.2 Work function and Jellium model

The work function is defined as the energy needed to remove an electron from the Fermi edge to the vacuum level (to a point of infinite distance from the material). This quantity is also related to the electrochemical potential of the electrons in the solid.[86] It is the contribution of the surface, to the energy which has to be applied to a material in order to eject an electron. The value depends on the material and the crystal structure of the material.

The "Jellium model" is a useful tool to explain the origin of the work function. It consists of an ordered array of positively charge metal ions. The electrons behave like a quasi "free electron gas". At the border to the surface the positively charge metal ions are not strong enough to keep electrons inside the material. Hence, the electrons can tunnel into the vacuum leading to a certain electron density outside the surface (see Figure 2.9).[87, 88]

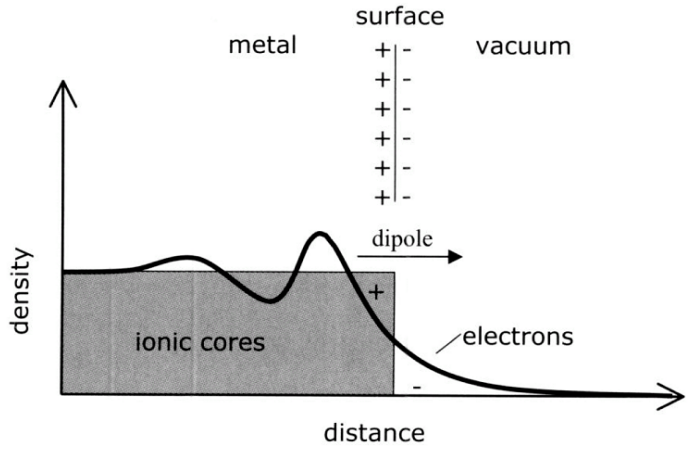

Figure 2.9 Illustration of the Jellium model. A free electron gas can diffuse into the vacuum leading to an increase in negative charge in direction of the vacuum, whereas the positively charged cores are fixed. This generates a surface dipole moment.[6]

A potential difference is built up, leading to a surface dipole moment. As will be discussed in detail in the following chapter, the electrons must have enough energy to overcome the barrier of the surface dipole moment.

Although the "Jellium model" is a quite simple model and holds only for alkali metals, it illustrates very well the importance of the surface dipole moment which is the surface contribution to the work function of a given material.

2.2.1.3 Work function determination

In order to determine the work function, one has to examine the lowest energy needed to remove an electron from a given material. This energy can either be applied thermally or via electronic excitation.[89]

In thermoelectric measurements the temperature dependence of electrons emitted from a surface is elucidated. Kelvin probe spectroscopy uses the difference in an electric potential between two solid state surfaces with different work functions (vibrating capacitor method).[90] In this thesis the work function was determined by means of photo electron spectroscopy (PES), via examining the spectrum width and subtracting the excitation energy from this value.[91]

The work function values gained by different methods are hardly comparable. The electron emission via optical methods occurs extremely fast and thus the final state is normally not completely relaxed (Franck-Condon principle).[92] The kinetic energy of the electron is influenced with respect to the degree of relaxation (the faster the relaxation occurs the higher the kinetic energy of the electron becomes). In contrast, Kelvin probe or thermoelectric measurements are performed under equilibrium conditions. Also, in photo-ionization experiments the lowest possible work function value is measured in any case, whereas in Kelvin Probe measurements an average value is always obtained. Therefore, one expects that by using Kelvin Probe, a higher work function value will be determined compared to values gained from PES experiments.

Most important is that the absolute value of the work function should not be stressed. As mentioned before, it depends on the experimental method. Furthermore, it is extremely sensitive and changes from day to day even for the same sample and the same method due to small impurities hardly seen in the spectrum shape.

Due to these inconsistencies, only relative changes of the work functions with respect to the value examined for a clean MgO surface on the same day and under similar measurements conditions will be discussed.

2.2.1.4 Conservation of energy and sample work function

In photo electron spectroscopy (PES) free electrons of a certain energy are generated. Their kinetic energy depends on the excitation energy, the work function of the sample and the binding energy of the excited electron.[91] Hence, the kinetic energy $E_{kin,S}$ of the electrons, leaving the surface, is determined by conservation of energy in the following way:

$$E_{kin,S} = h\nu - E_B - \phi_S \tag{2.13}$$

In order to measure the kinetic energy distribution of the electrons, they are guided and detected in a hemispherical analyzer. The analyzer A exhibits a work function ϕ_A, which has to be taken into account if the binding energies E_B of the detected electrons are to be determined.

For this purpose the sample and the analyzer are connected electrically, leading to a potential difference of $\Delta\phi = \phi_S - \phi_A$, whereas the Fermi edges of the two materials (analyzer and sample) are equilibrated ($E_{F,S} = E_{F,A}$).

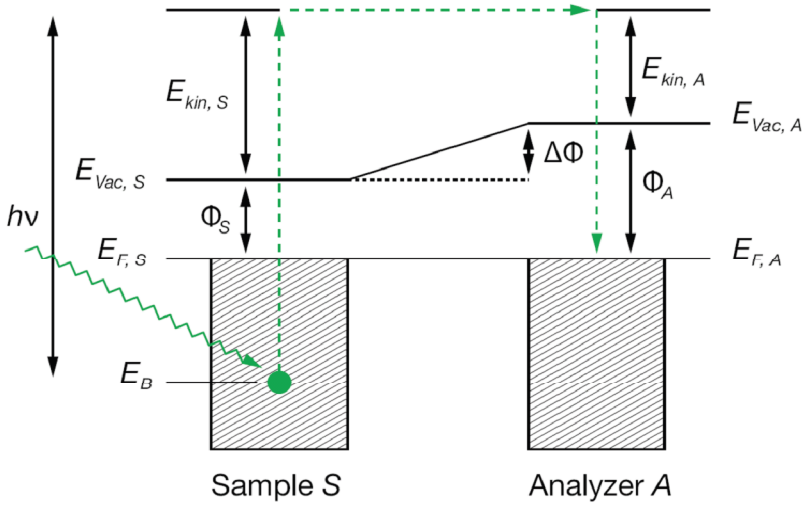

Figure 2.10 Energy diagram for a sample electrically connected with an analyzer.

The kinetic energy of an electron which is ejected form the sample into the vacuum is given by equation (2.14).

$$E_{kin,S} = h\nu - \phi_S - (E_{F,S} - E_B) \tag{2.14}$$

From Figure 2.10 the following relation can be concluded between the analyzer and the sample, which forms the base for the determination of the binding energy and the work function:

$$E_{kin,S} + \phi_S = E_{kin,A} + \phi_A \tag{2.15}$$

This allows the extraction of the kinetic energy of the electrons detected by the analyzer:

$$E_{kin,A} = E_{kin,S} + \phi_S - \phi_A \tag{2.16}$$

Using equation (2.15), (2.16) and the fact that the Fermi edges are equilibrated, leads to relation (2.17):

$$E_{kin,A} = h\nu - \phi_A - (E_{F,A} - E_B) \tag{2.17}$$

The electrons exhibiting the maximum kinetic energy are the electrons emitted from the Fermi edge. The binding energy of these electrons is zero $\left(E_F = E_B = 0\right)$, if the binding energies are derived with respect to the Fermi edge, as it is usually defined:

$$E_{kin,A}^{max}(E_F = E_B) = h\nu - \phi_A \tag{2.18}$$

The electrons with the lowest kinetic energy are those, with zero kinetic energy:

$$E_{kin,A}^{min}(E_{kin,S} = 0) = \phi_S - \phi_A = \Delta\phi \tag{2.19}$$

An important requirement for the correct application of UPS can be extracted from equation (2.19). If the work function of the analyzer is higher than the work function of the

sample the potential difference between the analyzer and sample leads to a cut-off of the spectrum. Hence, an additional potential (acceleration potential) must be applied to the sample with respect to analyzer, so that the electrons can overcome the barrier. The width of the spectrum can be determined by taking the difference of the maximum and minimum kinetic energy (equation 2.18 and 2.19):

$$\Delta E = E_{kin,A}^{max} - E_{kin,A}^{min} = h\nu - \phi_S \tag{2.20}$$

From the spectrum width one can elucidate the sample work function. It should be kept in mind that the discussed relations only hold for conducting materials, which exhibit electrons at the Fermi edge. For an insulator the Fermi edge and/or the work function of the analyzer must be determined by measuring a metal as a reference, because the Fermi edge of an insulator lies in the band gap.[1]
The correct binding energy with respect to the Fermi edge can be examined as follows:

$$E_B = h\nu - E_{kin,A} \tag{2.21}$$

In order to determine the work function of a given material the maximum binding energy has to be found:

$$\phi_S = h\nu - E_B^{max} \tag{2.22}$$

A typical spectrum of a d-metal is presented in Figure 2.11.

[1] Therefore no occupied states near the Fermi edge E_F are present.

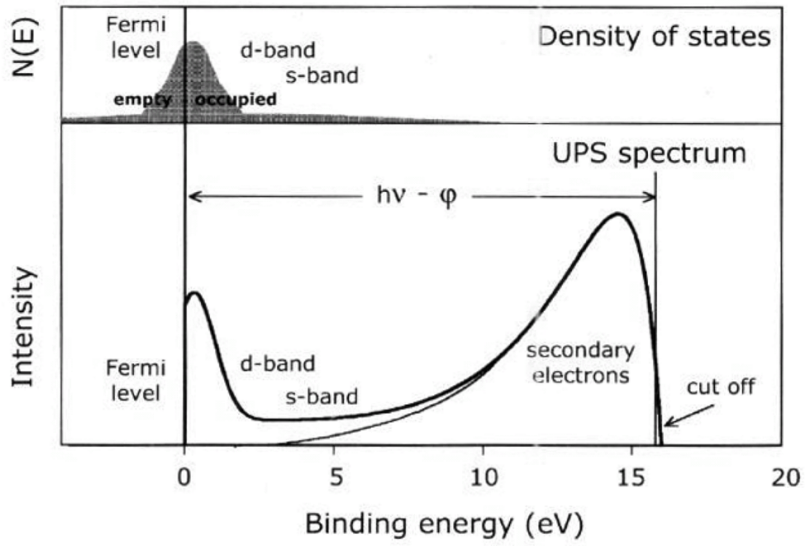

Figure 2.11 UPS spectrum of typical d-metal.[6]

The d-band is usually very narrow in contrast to s- and p- bands, due to the low overlap of the d-orbitals.[93] This leads to a distinctive Fermi edge for d-metals. It should also be noted that the yield of secondary electrons increases rapidly with increasing photon intensity. Hence, one has to find the optimum working conditions for a high information density of the valence band. The amount of secondary electrons should be as low as possible, since they attenuate the valence structure seen in the spectrum.

2.2.1.5 Complete formulation of the three-step model

In this chapter a complete formulation of the three-step model will be given. Each process will be treated independently and an equation will be formulated, taking each step into account. An electron in a solid state is defined by these two quantities: The energy E and the momentum $\underline{k}$, on which the following formulations are focused. A sketch that illustrates the different step of the three-step model is presented in Figure 2.12.

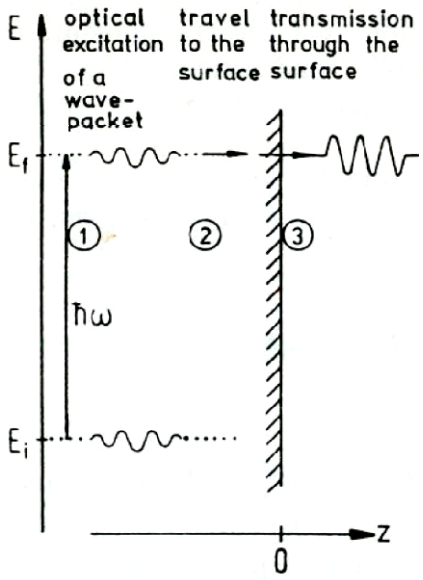

Figure 2.12 Ejection of an electron described in the three-step model. The electron is excited via absorption of a photon (1). In the second step (2) the electron diffuses to the surface and escapes subsequently through the surface into the vacuum (3).[94]

First step:

The first step describes the photo excitation of an electron. A band structure is shown in Figure 2.13 in order to clarify the different considerations.

An electron absorbs a photon of a given energy $h\nu$, leading to an excitation of the electron from its initial state E_i to a final state E_f that is determined by the photon energy and taking conservation of energy into account.

$$E_f\left(\underline{k}_f\right) - E_i\left(\underline{k}_i\right) = \hbar\omega \tag{2.23}$$

The final momentum of the excited electron can be described as follows:

$$\underline{k}_{final} = \underline{k}_{inital} + \underline{k}_{photon} + \underline{G} \tag{2.24}$$

The final wave vector $\underline{k}_{final}$ of the electron is the sum of the initial wave vector $\underline{k}_{inital}$, the wave vector of the photon $\underline{k}_{photon}$ and a reciprocal lattice vector $\underline{G}$. The reciprocal lattice vector $\underline{G}$ takes into account, that the final state of the electron, after the excitation

occurred, can be part of another Brillouin zone (part of the extended zone scheme). The reciprocal lattice vector allows folding back of the state into the 1. Brillouin-zone as shown in Figure 2.13.[95]

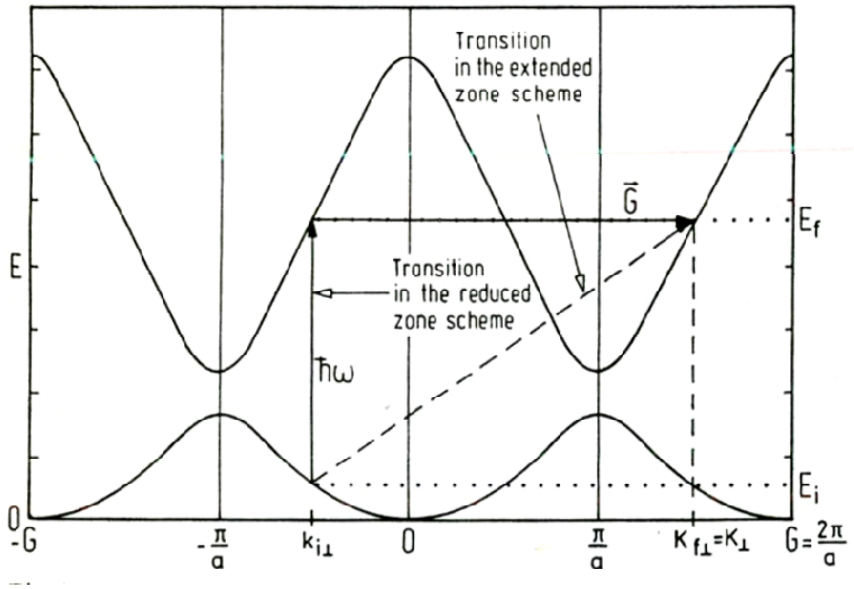

Figure 2.13 Transition via absorption illustrated in a dispersion relation. Transitions occur via absorption of reciprocal lattice vector G and thus the electron is excited into a neighboring Brillouin zone. The extended band structure can be folded back into the 1. Brillouin zone. Thus, the transition can be described as a direct transition, since the momentum k does not change upon excitation via UV photons.[94]

The photon momentum in UPS experiments is very small compared to the momentum of the electron and thus can be neglected.[91] Taking these two assumptions into account, it can be concluded that the momentum of the electron in the initial state equals the momentum in the final state:

$$\underline{k}_{final} \approx \underline{k}_{inital} \tag{2.25}$$

This assumption is of great importance, because it predicts, that only direct transitions ($\underline{k}_{final} = \underline{k}_{inital}$) occur, whereas indirect transitions are forbidden ($\underline{k}_{final} \neq \underline{k}_{inital}$). In contrast, the excitation energy used in XPS studies is around 1.5 keV. Therefore, the momentum of the photon can not be neglected and non-vertical transitions occur. A straight forward interpretation becomes impracticable and thus XPS, although electrons in the valence range can be probed, should not be used to determine the valence band structure.[94]

The internal energy distribution of photoexcited electrons $N_{\text{int}}(E_f, \hbar\omega)$, where E_f is the final kinetic energy and $\hbar\omega$ the photon energy, is given in the reduced zone scheme by:

$$N_{\text{int}}\left(k_f, \hbar\omega\right) \propto \sum_{f,i} \left|\mu_{f,i}\left(\underline{k}_f, \underline{k}_i\right)\right|^2 \times \delta\left(E_f\left(\underline{k}_f\right) - E_i\left(\underline{k}_i\right) - \hbar\omega\right) \delta\left(\underline{k}_f - \underline{k}_i - \underline{G}\right) \quad (2.26)$$

$E_f\left(\underline{k}_f\right)$ and $E_i\left(\underline{k}_i\right)$ denote the energies of the final and initial bands; $\mu_{f,i}\left(\underline{k}_f, \underline{k}_i\right)$ is the transition matrix in the linear perturbation approximation with $\underline{A}$ as the vector potential of the exciting electromagnetic field and $\underline{p}$ is the momentum operator of the electron:

$$\mu_{f,i}\left(\underline{k}_f, \underline{k}_i\right) = \left\langle f \left| \underline{A} \cdot \underline{p} + \underline{A} \cdot \underline{p} \right| i \right\rangle \quad (2.27)$$

The first delta function in equation (2.26) imposes energy conservation during the excitation (first step of the model) and the second delta function ensures that the work function of the sample is taken into account in determining the kinetic energy of the electron outside the sample.

Second step:

The second step of the three-step model describes the diffusion of the electron to the surface. The yield of photoexcited electrons that reach the surface exhibiting an energy of $E_f\left(\underline{k}_f\right)$ is reduced by electron–electron interactions that lead to inelastic scattering of the photoexcited electrons (secondary electrons). Assuming that the scattering frequency $\frac{1}{\tau}$, with τ as the lifetime, is isotropic and depends on the kinetic energy E of the electron only, the inelastic mean free path $\lambda\left(E,k\right)$ is given by:

$$\lambda\left(E,k\right) = \tau v_g = \left(\frac{\tau}{\hbar}\right)\left(\frac{\partial E}{\partial k}\right) \quad (2.28)$$

v_g is the group velocity in the final state. The transport can be described by a coefficient $d(E,k)$ that depends on the mean free path $\lambda(E,k)$ and the optical absorption coefficient α:

$$d(E,k) \simeq \frac{\alpha\lambda}{1+\alpha\lambda} \tag{2.29}$$

This can be included in equation (2.26) leading to a relation that describes the amount of electrons diffusing to the surface.[94]

$$\begin{aligned} N_{\text{int}}(\underline{k}_f, \hbar\omega) \propto \sum_{f,i} \left|\mu_{f,i}(\underline{k}_f, \underline{k}_i)\right|^2 d(E,k) \\ \times \delta\left(E_f(\underline{k}_f) - E_i(\underline{k}_i) - \hbar\omega\right)\delta(\underline{k}_f - \underline{k}_i - \underline{G}) \end{aligned} \tag{2.30}$$

Third step:

A photoexcited electron that has been diffused to the surface must transmit into the vacuum, which is described in the third step of the model. In order to pass through the surface the electron has to overcome the surface dipole moment that is described by the work function:

$$E_{kin} - E_f(\underline{k}_f) = \phi \tag{2.31}$$

The formulation of the momentum for the three step model is rather complicated compared to the energy. The Figure 2.14 illustrates the ejection of an electron out of the solid into the vacuum using a vector model.

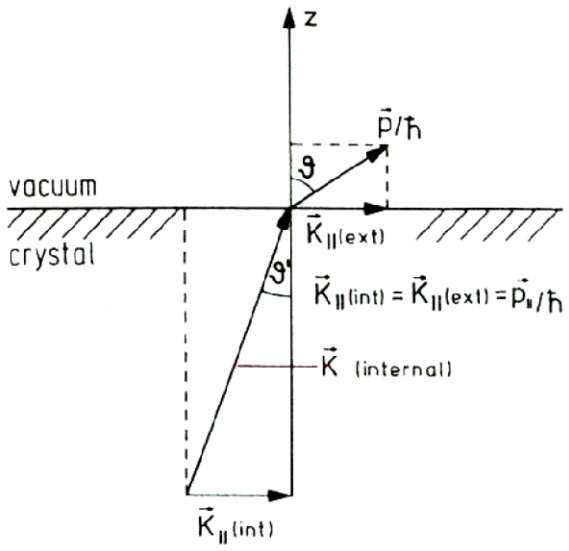

Figure 2.14 Vector model describing the escape of the excited electron through the surface. The momentum parallel remains conserved, since the translation symmetry holds parallel to the surface. However, the momentum perpendicular to surface changes, because the translation symmetry is broken in this direction.[94]

The momentum is split into a parallel and a perpendicular component. The translation symmetry must be taken into consideration in order to understand how the momentum of the electron is effected during the penetration through the surface. The translation symmetry parallel to the surface is conserved, whereas the symmetry perpendicular to the surface is broken. This means that the momentum parallel to the surface remains unaltered and thus still carries the same value as in the initial solid state (equation 2.32):

$$\frac{\underline{p}_{\parallel}}{\hbar} = \underline{k}_f^{\parallel} = \underline{k}_i^{\parallel} + \underline{G}^{\parallel} \tag{2.32}$$

In contrast, the component perpendicular to the surface is changed and its value becomes undetermined. In a free electron model with the bottom of the valence band lying at the minimum of the potential curve and the free electron model also holding for the ejected electron, the final momentum perpendicular to the surface is limited by the following equation:

$$\left(\frac{\hbar^2}{2m}\right) k_f^{\perp 2} \geq E_V - E_0 \tag{2.33}$$

Hence, $k_f^{\perp 2}$ is the momentum of the excited electron normal to the surface, E_0 is the bottom of the valence band and E_V the energy of the vacuum level. This leads to the conclusion that the escape angle differs from that inside the bulk as illustrated in Figure 2.14. The kinetic energy of the free electron is:

$$E_{kin} = \frac{\hbar}{2m}\left[\underline{k}_f^{\parallel 2} + \frac{\underline{p}_\perp}{\hbar}\right] = E_f\left(\underline{k}\right) - E_V \tag{2.34}$$

This equation contains the final momentum parallel to the surface $\underline{k}_f^{\parallel}$, however, it does not include $\underline{k}_f^{\perp}$ the component normal to the surface. In any UPS experiment performed with a fixed excitation energy (EDC, see chapter 2.2.1.1), the momentum perpendicular $\underline{k}_f^{\perp}$ remains undetermined and therefore the full vector $\underline{k}_f$ can not be examined.

In a real solid the wave function $\psi_f\left(\underline{k}\right)$ of a given state $E_f\left(\underline{k}\right)$ is not a single plane wave, but a Bloch wave containing plane wave contributions with a number of reciprocal lattice vectors $\underline{G}$:

$$\psi_f\left(\underline{k}\right) = \sum_G u_f\left(\underline{k}, \underline{G}\right) \cdot e^{i\left(\underline{k}+\underline{G}\right)\cdot \underline{r}} \tag{2.35}$$

Plane wave components of a single Bloch wave of a given kinetic energy E with the same value of $\underline{k}_i^{\parallel} + \underline{G}^{\parallel}$ leave the crystal in the same direction and hence are coherent. The total transmission for such a $\underline{k}_i^{\parallel} + \underline{G}^{\parallel}$ beam at a particular final state E_f is then expressed as the sum of the transmission factors for each plane wave:

$$\left|T\left(E_f, \underline{k}_i^{\parallel}\right)\right|^2 = \left|t\left(E_f, \underline{k}_f^{\parallel}\right)\right|^2 \left|\sum_{\left(\underline{k}+\underline{G}\right)>0} u_f\left(\underline{k}, \underline{G}\right)\right|^2 \tag{2.36}$$

The summation over $\left(\underline{k}+\underline{G}\right)>0$ takes into account that only states with components propagating towards the surface can transmit into the vacuum.

Summarizing all these relations, a final expression for the angle-resolved photoelectron energy spectrum that takes the three step model into account can be formulated:

$$\begin{aligned} N_{\text{int}}\left(E_{kin},\underline{k}_f^{\parallel},\hbar\omega\right) \propto & \sum_{f,i}\left|\mu_{f,i}\left(\underline{k}_f,\underline{k}_i\right)\right|^2 d\left(E,k\right)\left|T\left(E_f,\underline{k}_i^{\parallel}\right)\right|^2 \\ & \times\delta\left(E_f\left(\underline{k}_f\right)-E_i\left(\underline{k}_i\right)-\hbar\omega\right)\delta\left(E-\left[E_f\left(\underline{k}_f\right)-\phi\right]\right) \\ & \times\delta\left(\underline{k}_f^{\parallel}-\underline{k}_i^{\parallel}-\underline{G}^{\parallel}\right)\delta\left(\underline{k}_f^{\parallel}-\frac{\underline{p}_{\parallel}}{\hbar}\right) \end{aligned} \qquad (2.37)$$

The first delta function describes the conservation of energy for the excitation process, the second takes the work function into account, the third describes the direct transition (conservation of momentum) and the fourth the conservation of the momentum parallel to the surface during the escape of the electron from the surface.[94]

2.2.1.6 Angle-Resolved UPS (ARUPS)

If the sample can be rotated, angle-resolved measurements become feasible. Experimental results for angle-resolved UPS spectra are of great interest, because they allow one to determine a two dimensional band structure and are consequently of great interest for theoreticians.

In the nanocatalysis laboratory the crystal holder can be rotated, however, since the crystals are not fixed in the rotation axis of the manipulator, the position can not be kept constant for different angles (x- and y-coordinates change for different angles) as seen in Figure 3.2. Thus, angle-resolved experiments can not be performed with the present setup. A new sample holder would be need to be designed to achieve rotation at constant x and y-axis values.

The major aim is to detect clusters on a given support material. If we take the considerations into account that have been done in the last chapter, we remember that the interpretation of UPS spectra is based on the three step model. In this model it is assumed that the translation symmetry is broken perpendicular to the surface and that it remains conserved parallel to the surface as illustrated in Figure 2.15. This would than allow the determination of the two dimensional band structure.[96]

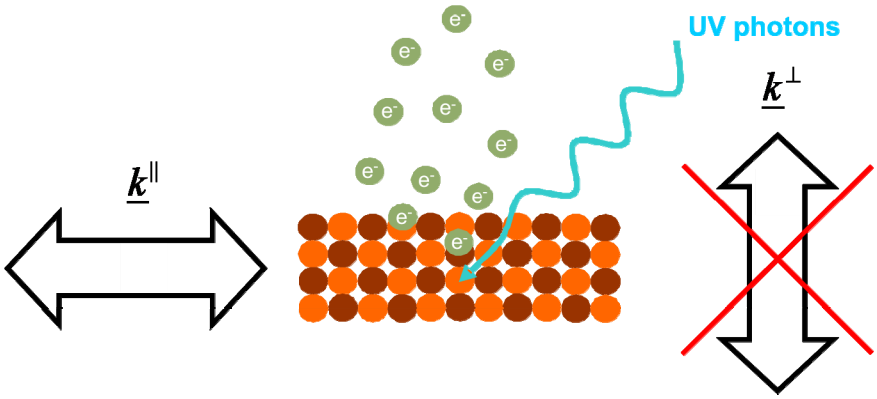

Figure 2.15 Symmetry analysis of a clean MgO surface. The translation symmetry is broken perpendicular to the surface and remains unaltered parallel to the surface.

Assuming that small metal clusters are deposited onto a flat perfect MgO film it becomes obvious that the translation symmetry remains conserved for the MgO film but it is not conserved for the cluster layer (see Figure 2.16). Consequently, the momentum parallel $\underline{k}^{\parallel}$ and perpendicular to surface $\underline{k}^{\perp}$ become undeterminable and an interpretation of the results can not be achieved.

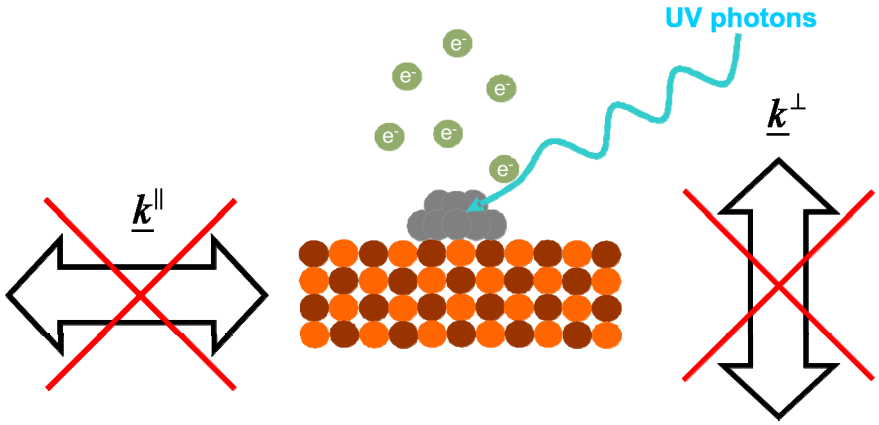

Figure 2.16 Symmetry analysis for deposited clusters. The translation symmetry is broken in both directions. Thus, the momentum vector is undetermined for this case.

In conclusion, angle-resolved will not be performed in the future, because no additional information can be gained from angle-resolved experiments. In order to determine the full band structure theoretical calculations would need to be performed additionally.

2.2.2 Metastable Impact electron spectroscopy (MIES)

In MIES experiments a metastable rare gas atom is used instead of photons as energy projectiles to probe a surface. This method has the advantage that in contrast to a UV photon the rare gas atoms can not penetrate into the surface, because they are too large and the kinetic energy is too low to induce sputtering processes (≈ 0.1 eV).[97] Thus, MIES probes the uppermost layer exclusively.[98] However, ionization can occur via different processes, which leads to the fact that MIES spectra are challenging to interpret.

2.2.2.1 Singlet vs. Triplet state

A MIES source for metastable He* atoms produces the singlet (2^1S_0) as well as the triplet (2^3S_1) state. Both exhibit different excitation energies, the singlet state has an energy which is 0.8 eV higher than the one for the triplet state.

The distance from the source to the sample is roughly 0.5 m and the velocity of the metastable atoms is 2000 m / s. Using these values, it can be calculated that it takes the metastable atoms about $2.5 \cdot 10^{-4}$ s to reach the surface. The chopper frequency used in the presented work is 900 Hz. Thus, every $\approx 10^{-3}$ s photons and He* strike onto the surface and eject electrons. This excludes further excitation of the He beam, by a following photon beam shot.[83]

The rates for a 2^1S_0 to decay to the ground state (fluorescence, F) and deexcite to a 2^1S_3 via intersystem crossing (ISC) are $k_F = 10^6 - 10^9$ s^{-1} and $k_{ISC} = 10^6 - 10^{11}$ s^{-1}. Therefore it can be assumed that no metastable atoms in the 2^1S_0 state reach the surface, because either they deecxite via fluorescence or they deexcite to the triplet state via intersystem crossing (ISC).

2.2.2.2 Overview of the different photo ionization mechanisms of MIES

Figure 2.17 summarizes all different mechanisms which have to be taken into account for the interpretation of MIES spectra. As mentioned before, the source creates singlet as well as triplet metastable atoms. However, due to the deexcitation rates of fluorescence and intersystem crossing, only triplet states reach the surface and lead to photo ionization processes.

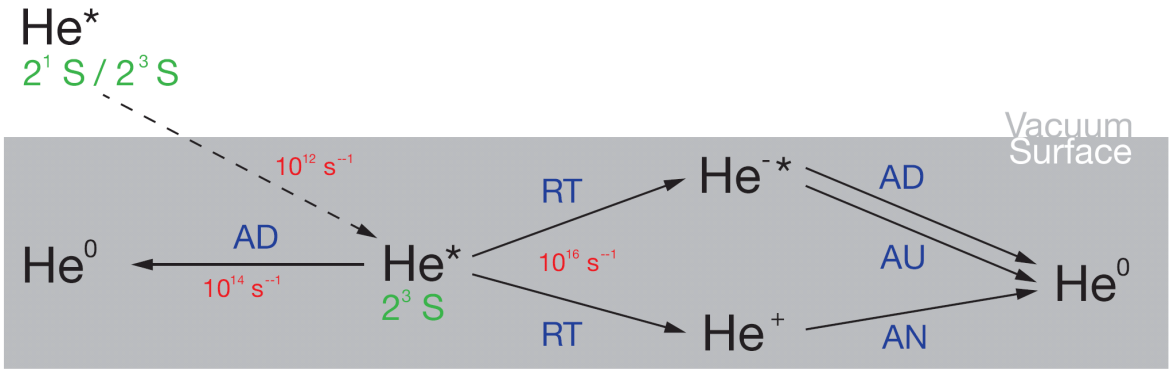

Figure 2.17 Different interaction paths for the dexcitation of a metastable atom on a surface, with their corresponding rates.[83]

Depending on the electronic properties of the sample two processes can occur in the first interaction step, either Auger Deexcitation (AD) or a Resonance Transfer (RT). AD leads directly to the ground state. This process can occur for all surfaces no matter which electronic properties the sample exhibits. A look at the rate constants shows that Auger Deexcitation (AD) is about two orders of magnitudes, slower than the Resonance Transfer (RT). The RT mechanism depends on the energy level of the Fermi edge (or the VBM for insulating materials) with respect to the level of the 2s-electron of the metastable.

The RT process leads either to a negatively charged metastable or to a positive ion. In the case of the cation the deexcitation into the ground state proceeds via Auger Neutralization (AN), whereas for the negatively charged ion again one of two possible Auger Decay Processes (AD or Autodetachment (AU) leads to the ground state.

For better illustration in the following chapters the different deexcitation mechanisms are explained in further detail.

2.2.2.3 Auger Deexcitation (AD)

The AD process of the metastable does not depend on the work function of the solid. Hence, it occurs for every material: Metals, semi-conductors and insulators.[99]

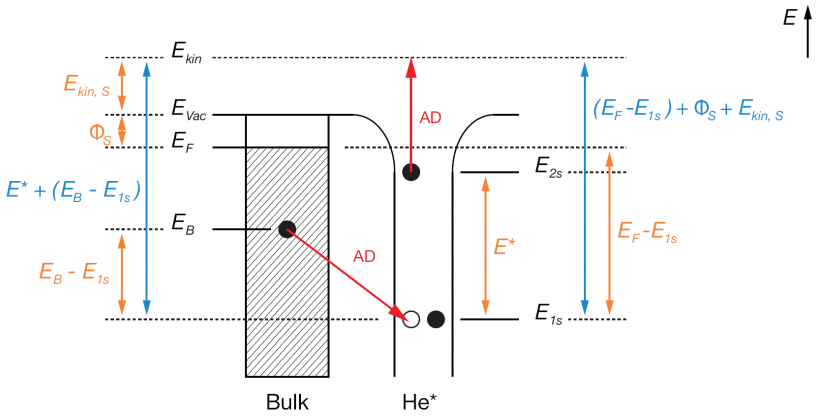

Figure 2.18 Illustration of the AD process with the corresponding energies. A surface electron tunnels into the 1s state of the helium atom and the 2s electron is ejected.[83]

In an AD process (Figure 2.18) an electron of the surface with a certain binding energy E_B tunnels into the free 1s-state of the metastable He*. In an intramolecular Auger decay the 2s-electron is emitted into the vacuum with an energy of $E_B - E_{1s}$. Thus, it can be said that the emitted Auger electron carries the information of the surface electron, which has tunneled into the 1s state.

From the sketch it can be easily seen that the following equation holds:

$$E^* + \left(E_B - E_{1s}\right) = \left(E_F - E_{1s}\right) + \phi_S + E_{kin,S} \tag{2.38}$$

The resulting kinetic energy of the sample and kinetic energy detected by the analyzer are defined as follows:

$$\Rightarrow E_{kin,S} = E^* - \phi_S - \left(E_F - E_B\right) \tag{2.39}$$

$$\Rightarrow E_{kin,A} = E^* - \phi_A - \left(E_F - E_B\right) \tag{2.40}$$

If the excitation energy E^* is replaced by the term $E = h\nu$ in formula 2.40 one obtains the same equation for $E_{kin,S}$ as for UPS (see equation 2.14).
From spectra which originate only from AD processes, the width of the spectrum can be determined similar to in UPS experiments and the work function can be evaluated. 2.39 is rewritten to:

$$E_{kin,S} + \phi_S = E^* - (E_F - E_B) \tag{2.41}$$

Inserting this into 2.40 one obtains the same formula for $E_{kin,A}^{min}$ as for UPS (equation 2.19):

$$E_{kin,A}^{min}\left(E_{kin,S} = 0\right) = \phi_S - \phi_A = \Delta\phi \tag{2.42}$$

Using the assumption of $E_B = E_F$, the maximum kinetic energy is:

$$E_{kin,A}^{max}\left(E_B = E_F\right) = E^* - \phi_A \tag{2.43}$$

Finally, combining equation 2.42 and 2.43 leads to the spectrum width ΔE_{AD} . However, this relation holds only if the spectrum is determined by AD processes:

$$\Delta E_{AD} = E^* - \phi_A - \phi_S + \phi_A = E^* - \phi_S \tag{2.44}$$

2.2.2.4 Resonant Transfer (RT)

The second decay process that can occur for the metastable atom on a surface is Resonant Transfer (RT). With decreasing distance between the metastable atom and the surface the overlap between the wave functions of surface and metastable increases. According to Fermi's golden rule the tunneling probability for electrons into resonant states increases.

Depending on the work function of the sample two different mechanisms can be observed. Either the 2s-electron can tunnel into an unoccupied state of the surface or an electron from an occupied surface state tunnels into the half-filled 2s-level of the metastable atom. For simplification it can be said that either a positively charged or a negatively charged He atom is created by RT. The RT process occurs with a rate of $\approx 10^{16}s^{-1}$ and is fast in comparison to the AD ($\approx 10^{14}s^{-1}$).[100] Different deexcitation mechanism are then observed depending on whether a positively or a negatively charged He state appears. They will be discussed in the following sections.

2.2.2.5 Resonant Transfer (RT) followed by Auger Neutralization (AN)

If the resonant transfer occurs from the 2s state of the He* into an unoccupied state of the solid, a positively charge He^+ ion is generated that is deexcited via an electron transfer from the solid into the 1s state of the He*. This process, called Auger Neutralization (AN), is limited to materials where the valence band (VB) maximum lies below the 2s-level of the He*. Otherwise the RT process occurs from the material electronic states into the 2s level of the He*. Furthermore, unoccupied states must be available close to the energy level of the 2s state. These requirements are only fulfilled for conductors or semiconductors exhibiting a work function value greater than 3.8 eV. The process is summarized in Figure 2.19.

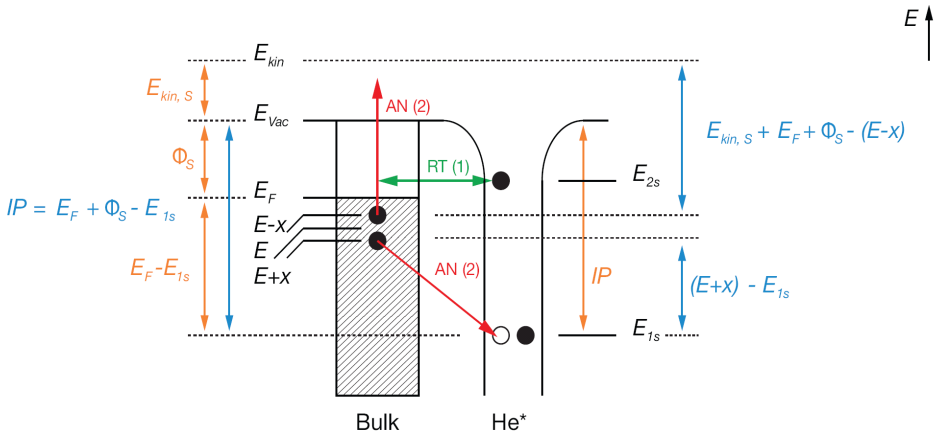

Figure 2.19 Illustration of RT process followed by an AN. The 2s electron tunnels into an unoccupied surface state. A surface electron tunnels into the 1s state neutralizing the helium atom and a second surface electron is emitted into the vacuum.[83]

The ionization potential (IP) can be derived as followed:

$$IP = \phi_s + E_F - E_{1s} \tag{2.45}$$

The process is driven by the electron that tunnels into the 1s state, because the energy gained in this process leads to ejection of an electron from the material. Thus, the energy consumed for the ionization process equals the energy that is set free due to the tunnelling process of the surface electron into the 1s state. The energy balance for this mechanism is:

$$E_{kin,S} + \phi_S + E_F - (E - x) = (E + x) - E_{1s} \tag{2.46}$$

If this equation is combined with 2.44, a relation for the kinetic energy of the sample can be formulated:

$$E_{kin,S} = IP - 2(\phi_S + E_F - E) \tag{2.47}$$

A similar relation can be gained for the kinetic energy of the analyzer by substituting $E_{kin,S}$ with the following equation that has already been introduced in the previous chapter about UPS (2.15):

$$E_{kin,S} = E_{kin,A} - \phi_S + \phi_A \tag{2.48}$$.

Thus, the correct kinetic energy detected by the analyzer is:

$$E_{kin,A} = IP - \phi_S - \phi_A + 2(E_F - E) \tag{2.49}$$

The electron emitted from the Fermi edge exhibits the maximum kinetic energy $E_{kin,A}^{max}$:

$$E_{kin,A}^{max}(E = E_F) = IP - \phi_S - \phi_A \tag{2.50}$$

The minimum kinetic energy $E_{kin,A}^{min}$ is the same as previously shown for UPS and AD:

$$E_{kin,A}^{min}\left(E_{kin,S}=0\right)=\phi_S-\phi_A \tag{2.51}$$

Combining these equations, a relation for the width of the spectrum ΔE_{AN} can be formulated:

$$\Delta E_{AN}=E_{kin,A}^{max}-E_{kin,A}^{min}=IP-2\cdot\phi_S \tag{2.52}$$

2.2.2.6 Resonant Transfer (RT) followed by Autodetachment (AU) or Auger Deexcitation (AD)

For materials exhibiting low work function values (< 2.2 eV) an electron from an occupied state (below the Fermi level) can tunnel resonantly into the 2s-level of the metastable atom (RT). However, this process is restricted to metals and semi-conductors, because for insulators the energy of the upper level of the VB lies below the 2s-state of the metastable He*.

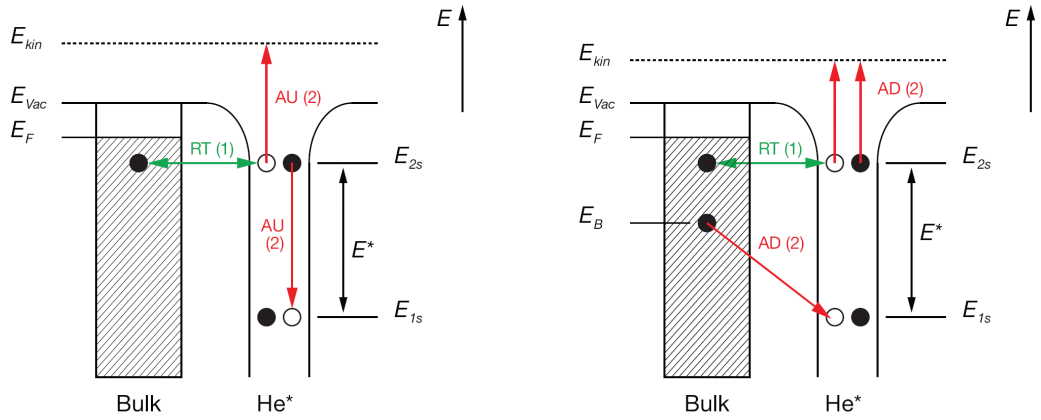

Figure 2.20 Illustration of a RT followed by either an AU (left) or an AD (right). In both cases a surface electron tunnels via RT into the 2s state of the helium atom. In the AU process the transferred electron is ejected while the other 2s electron falls into the 1s state. In the case of an AD process the transferred electron and the 2s electron are emitted, while a bulk electron tunnels into the 1s state of the helium atom.[83]

A negatively charged He^{*-} is created that can either relax via an Autodetachment (AU) or Auger Deexcitation (AD) as seen in Figure 2.20.

In the case of RT followed by AU, the He* relaxes in an intramolecular Auger decay into the unoccupied 1s-state. The released energy is transferred to the second 2s-electron, which is subsequently emitted. In a MIES spectrum this process can be identified by a sharp peak close to the Fermi edge, because this mechanism can only occur if the 2s state lies below the Fermi edge, which is rarely observed.

In contrast to the aforementioned AU, an intermolecular Auger process takes place for the RT followed by an Auger Deexcitation (AD) in which the 1s hole gets filled by a surface electron and both 2s electrons are ejected.

3 Experimental

3.1 Cluster source

The experimental setup used in the presented work, is schematically shown in Figure 3.1. The first part is the cluster source. Using a Nd:YAG diode pumped laser (*InnoLas* DPSS Spitlight; 532 nm; 100 Hz; 70 mJ) high energy laser pulses are focused through a viewport onto a rotating target of the desired metal.[39]

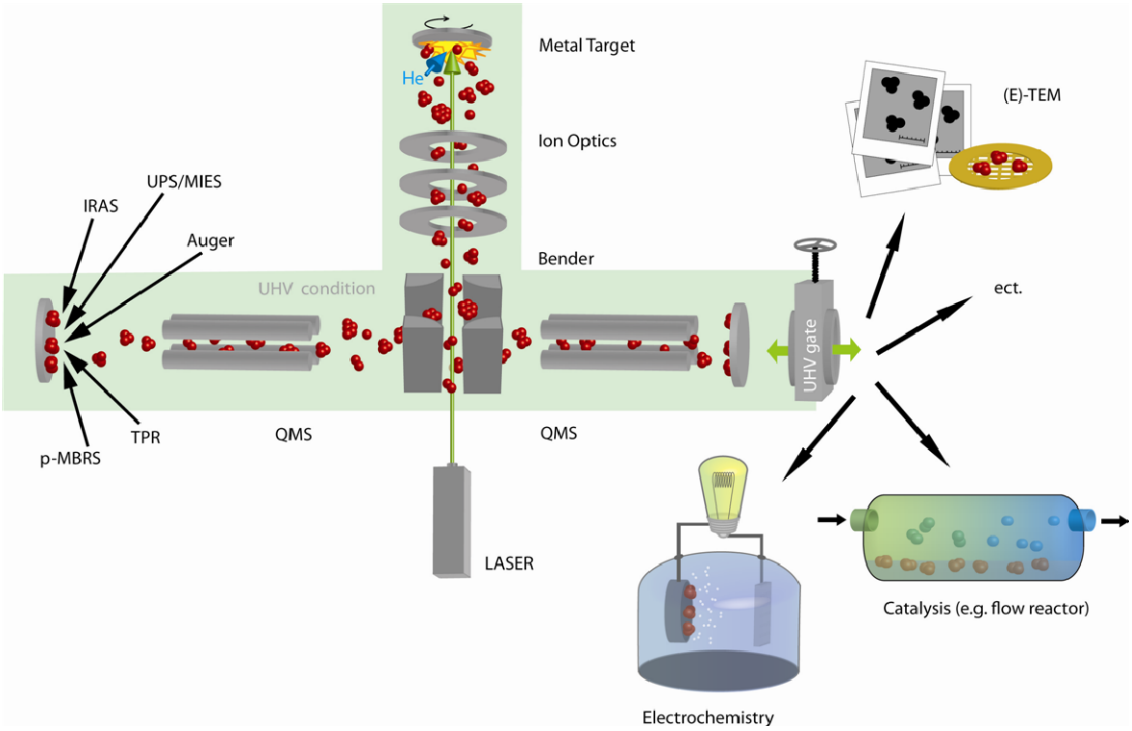

Figure 3.1 The experimental setup can be divided into three compartments. The middle part is that clusters source. Clusters are generated and guided to the bender. At the bender the cluster beam can be guided either to the left side, which is the UHV chamber or to the right side which allows transferring of cluster samples.

Induced by the laser pulse a metal plasma is formed, which is thermalized by a helium pulse. Through supersonic expansion of the metal-helium vapor a cluster beam of different masses and differently charged states with a narrow kinetic energy distribution is formed. The cluster beam is guided through a skimmer, an octopol and Einzel lenses through the differentially pumped apparatus. The next step is the bender which consists of a quadrupole turned by 90° upwards. At this part of the setup the positively charged clusters

are either guided to the left to perform experiments under UVH conditions or the right to prepare samples that can be transferred to ambient conditions. Negatively charged ions are bended in the opposite direction and neutral clusters fly straight onto the viewport through which the laser beam enters the apparatus. Depending on the settings of the bender a certain mass to charge ratio is guided through the next ion optic because the trajectory of the beam has to fit to the voltages applied to the quadrupole. Thus, a certain mass distribution is allowed to pass. The width of the distribution is given by the size of the bender exit plate. Subsequently, on both sides of the setup, the cluster beam enters a quadrupole mass spectrometer (Extrel). The spectrometer can operate either in a mass-unselected "RF only" mode, or in a mass-selecting mode. In the "RF only" mode the size-selection is exclusively determined by the bender settings, whereas in the "mass-selecting" mode the resolution can be increased up to single mass selection.
The following steps, which include the deposition of the clusters and different experiments of this work, are described in the following section.

3.2 Vacuum chamber

On the left side of the apparatus the cluster beams enters a 4000 amu mass-limited mass-spectrometer (Figure 3.1). Subsequently, the mass-selected clusters are deposited onto a thin MgO film grown on a Mo(100) single crystal. In the vacuum system many different experiments can be performed in order to characterize either the support or the deposited clusters.
In the following chapter all important data about the samples used in this work are summarized. Afterwards the experimental details of the different electron spectroscopic methods, used in the presented work, are described, followed by the different reactivity characterization techniques and the IRAS setup.

3.2.1 Sample

3.2.1.1 Crystal holder

All vacuum experiments presented in this work have been performed on MgO support grown on a Mo(100) crystal. The nanocatalysis setup is equipped with a threefold crystal holder, which has been described in detail previously.[101] The holder is welded to a manipulator that allows moving of the samples vertically in z-direction and horizontally in x- and y- directions. Furthermore, the manipulator can be rotated (360°). This enables the position of the sample holder can be controlled in all directions.

The Mo(100) single crystal is fixed with two tantalum wires which are spot-welded onto two tungsten rods of the sample holder. Applying a current to the tantalum wires the crystal can be heated resistively. The temperature is measured by using a type C thermocouple. It should be mentioned that for a molybdenum single crystal this type of thermocouple has to be used, because the Mo crystal must be heated to 1700 K for cleaning purposes and no other thermocouple type allows measurements in that temperature range. A picture of the crystal holder in the main chamber can be seen in Figure 3.2.

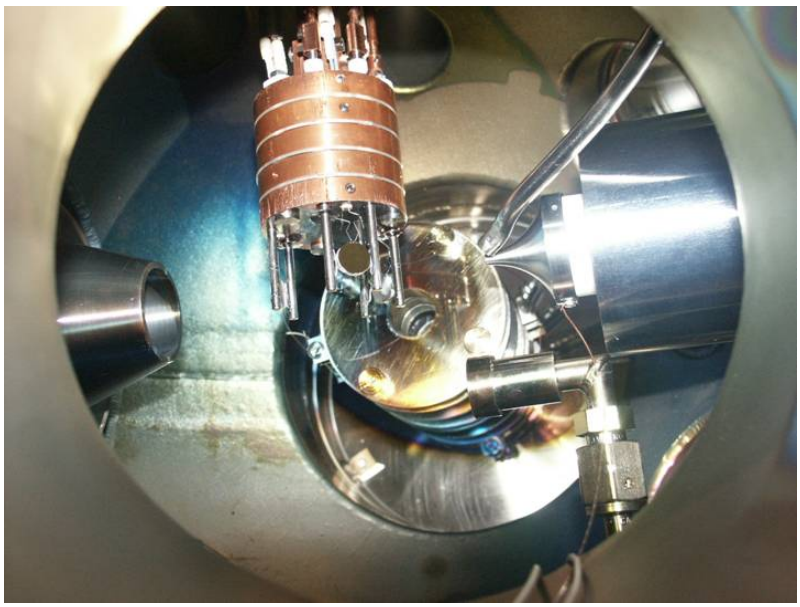

Figure 3.2 In the middle of the chamber is the sample holder with three crystals mounted to it.

3.2.1.2 Crystal cleaning

In order to clean the crystal a home-built electron gun is used (see Figure 3.3). It consists of a coiled tantalum wire, which is spot-welded onto two rods. These rods are screwed onto a ceramic holder that is connected to an in-out moveable manipulator. Two copper wires which are insulated by ceramics connect the rods with two copper feed-throughs. A current is applied to the tantalum filament in order to use the e-gun.

Figure 3.3 The left picture shows the e-gun as it is attached to the vacuum chamber. On the right side the e-gun is represented without the shielding. It consists of a tantalum wire spot welded onto two rods.

To clean the crystal the electron gun is moved close to the backside of the Mo(100) single crystal, the crystal is grounded and a current is applied to the filament. The emitted electrons are focused onto the crystal; the shielding is floating and charges up during operation. Hence, the shielding acts as a focusing element. In order to reach high temperatures the applied current is additionally biased with 3 kV.
The cleanliness of the crystal is measured by means of auger electron spectroscopy (AES). A typical spectrum is presented Figure 6.1.

3.2.1.3 Preparation of MgO film

Magnesium is evaporated by use of a home-built evaporator. A Mg ribbon is used to form a small magnesium block, which is fixed in a tantalum wire coil. This coil is spot-welded onto two metal rods to which a current can be applied. The current which has to be applied to the tantalum wire depends on the resistance.

It has been shown in the past that applying a power of 4 W usually leads to a constant, acceptable evaporation rate. At the same time a constant oxygen background is set ($p = 5 \cdot 10^{-7}$ mbar), the sample is heated to $T = 350$ K and moved in front of the magnesium evaporator. The quality is measured by means of Auger electron spectroscopy (AES) (see Figure 6.1).

3.2.2 MIES/UPS

Since a MIES/UPS source is based on a discharge lamp, the different working conditions of a discharge are described. Furthermore, all improvements of the source and the data acquisition method are specified in detail.

3.2.2.1 General aspects of a DC discharge source

Figure 3.4 (left) shows the normal configuration of a DC glow discharge lamp, a long glass cylinder with the positive anode at one end and a negative cathode at the other end. Conditions to maintain the discharge are pressure ranges between 10 mTorr and 10 Torr as well as a potential of a few hundred volts. The figure also shows the quite complicated behaviour of a discharge with its light and dark areas that depend on the pressure and voltage with respect to both size and intensity.

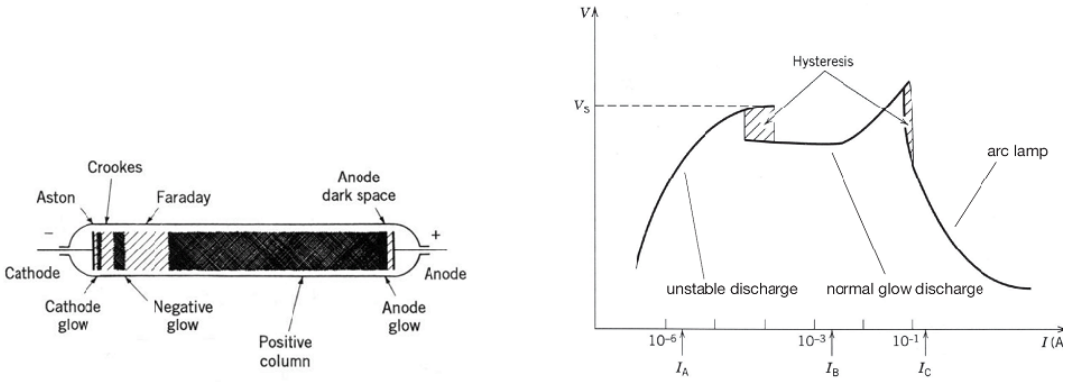

Figure 3.4 The different domains of a DC glow discharge are shown on the left side of the Figure 3.4. The voltage-current characteristic is presented on the right side. The normal glow discharge is the range for the correct working conditions of a MIES/UPS source.[102]

On the right side of Figure 3.4 the voltage-current characteristic of a discharge is shown. In the low current range no stable discharge can be achieved. For increasing currents the voltage increases monotonically until a transition is reached (with hysteresis) and the normal glow discharge is established. This plateau is the range, in which stable discharge conditions can be achieved (around I_B). The current can be varied over a broad range without any voltage changes. The normal glow discharge range is followed by a voltage increase (I_c) and a subsequent rapid voltage decrease. In this region the discharge is no longer a cold discharge, but rather in an operation mode similar to an arc discharge.[103]
The requirements for the MIES/UPS discharge source (cold cathode) are stable working conditions, which are only the case in the region of the normal glow discharge. Depending on the geometry of the source, one has to find the right parameters for a normal glow discharge, which enables stable photon and metastable atom emission for spectroscopic measurements.

3.2.3 First MIES/UPS source version

The MIES/UPS source built by Kempter *et al.* at the TU Clausthal-Zellerfeld is based on a source, which has been first reported at the end of the 1970s. In order to separate the electrons emitted by photons and those emitted by metastable He* atoms a chopper was used to apply a time of flight separation (TOF) of both excitated species before they reach the surface.

The first cold cathode source for metastable atoms has been designed by Leasure *et al*. and Farey *et al.*.[104, 105] An illustration is given in the following figure.

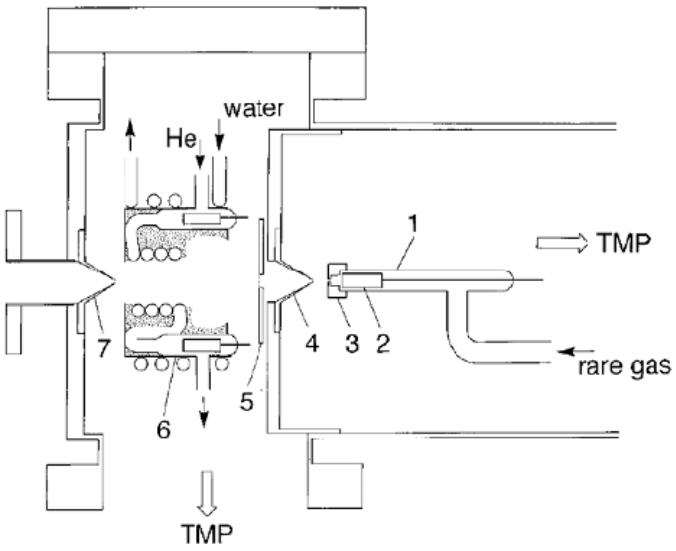

Figure 3.5 First MIES source: cold cathode; (1) pyrex tube, (2) tanatalum-cathode, (3) boronitride-nozzle, (4) skimmer, (5) repeller grid, (6) quench-lamp, (7) skimmer.

The discharge occurs between a tantalum hollow cathode (2) and a stainless steel skimmer (4) across a pressure gradient (created by differential pumping). Electrons and He^+ ions (due to discharge) are removed with a repeller grid (5).

3.2.4 MIES/UPS source developed by Kempter *et al.*

The source developed at the TU Clausthal-Zellerfeld (see Figure 3.6) is based on the above described source. The major improvement of this source in comparison to the first, is the use of a second discharge, which doubles the yield of the photons and increases the amount of metastable atoms by a factor of around 30.[106]

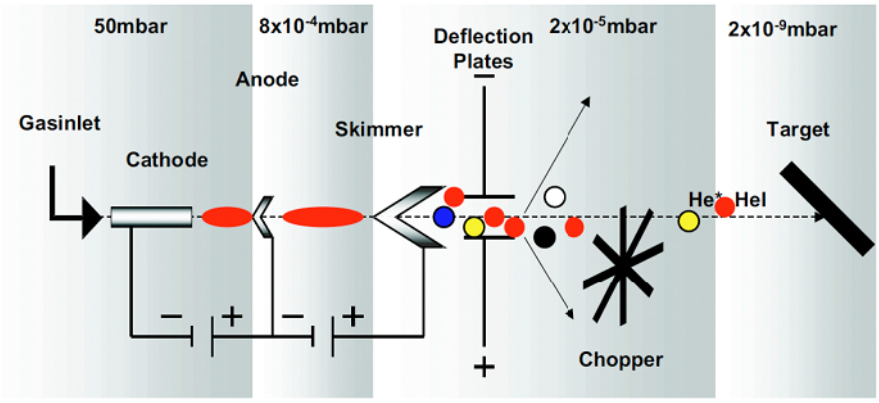

Figure 3.6 MIES/UPS source with two discharges developed by Kempter *et al.*

The first part of the source (Figure 3.6) is the discharge chamber, in which the He is injected (p = 50 mbar) through the cathode; the actual discharge is maintained by a DC voltage (–200 V) applied between cathode and anode.[107] The anode separates the buffer chamber from the source chamber. In the source chamber, the second discharge is ignited, by applying another DC voltage (+250 V) between the anode and the skimmer. Furthermore, the pressure of the source chamber is kept low ($p = 8 \cdot 10^{-4}$ mbar). This leads to a reduced collision probability between the metastable atom and hence, deexcitations due to collisions are minimized.

In the last part of the source, which is the buffer chamber ($p = 2 \cdot 10^{-5}$ mbar), the deflector removes undesired charged particles (electrons and He^+), from the particle flow. Finally, the beam continues through a chopper in order to perform a TOF separation.[106]

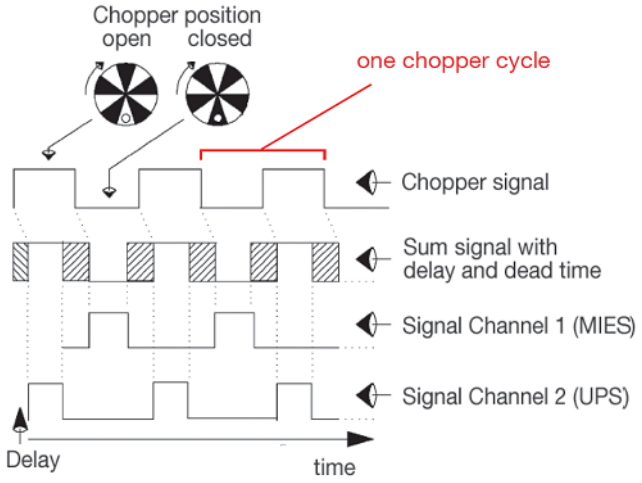

Figure 3.7 Principle of TOF separation. The chopper frequency must be optimized to achieve a proper separation of MIES and UPS signals as shown in the sketch.

The metastable atoms and photons which leave the source enter the UHV-chamber and hit the surface with an angle of approximately 50°. The kinetic energy of the emitted electrons is then detected by a hemi-spherical analyzer (the same analyzer is used for Auger electron spectroscopy) and the signals are recorded by a computer. The electrons, originating from ultraviolet photons or metastable He* atoms, can be separated by a home-built analyzing system, for a given chopper frequency.

In order to adjust the chopper to the right frequency, one has to calculate the time of flight of the metastable atoms. Furthermore, the distance between the chopper and the sample has to be known. Assuming a distance of 0.5 m and a metastable velocity of 2000 m/s a frequency of 1000 s^{-1} can be calculated. However, one chopper cycle includes an opening gate and a closing gate. Thus, the frequency has to be doubled to 2000 s^{-1}.

3.2.4.1 MIES/UPS source of the nanocatalysis laboratory

The source which has been used in this work is based on the source constructed at the TU Clausthal-Zellerfeld. However, some parts have been redesigned, because the source could not be operated under stable conditions. A drawing of the current source, used currently in the nanocatalysis laboratory, is shown in Figure 3.8.

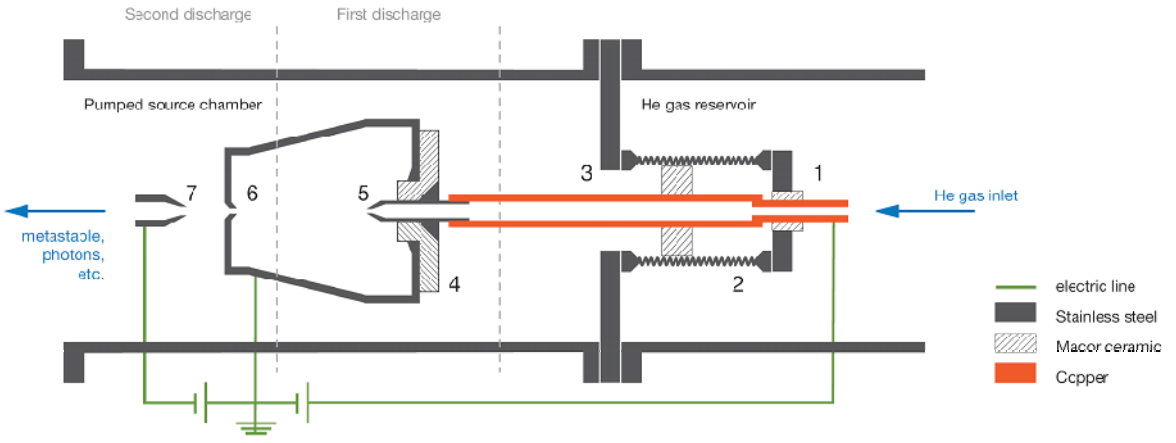

Figure 3.8 Improved source of the nanocatalysis laboratory. 1) drilled current feed through CF-16, 2) bellow CF-16, 3) reduction flange CF-100 to CF-16, 4) spacer, 5) cathode nozzle (first discharge), 6) anode skimmer plate, 7) skimmer (cathode).[83]

The major problem of the old setup was to supply the source with He. As seen in Figure 3.8, the helium has to flow through the cathode (5). At the same time the cathode (5) is part of the first discharge and thus a voltage is applied between skimmer plate (6) and the cathode (5). Since the skimmer plate (6) is grounded, the cathode (5) must be insulated form the ground to enable applying of a voltage. In the old setup the cathode (5) was connected to the gas inlet with a plastic tube. However, in the nanocatalysis laboratory the plastic tube melted during the operation mode and hence the setup had to be improved.
The problem was overcome by use of a commercial copper feed-through, which is drilled in the center of the copper rod as marked red in Figure 3.8. However, using this approach a different problem arises, because the ceramic part of the feed-through is extremely fragile. During the operation mode heat expansion of the feed-through has to be taken into account and thus, an expandable element has to be added to compensate any expansion. The drilled feed-though (1) is fixed on a bellow (2). The cathode nozzle (5) and the feed-through (1) are screwed together via a copper tube. To avoid electrical contact between the copper tube and the bellow and thus shorting the circuit, a round ceramic is fixed onto the copper tube.
The nozzle is a stainless steel tube with a thread on the outside of the tube. It is screwed into the stainless steel counterpart of the ceramic (4). The distance between the cathode and the skimmer plate must be adjusted by varying the position of the cathode with respect to the ceramic counterpart. Using a nut, the position of the tube in the ceramic counterpart is fixed.
For a complete installation the cathode has to be connected with the copper feed-through by a copper tube, as already mentioned above.It has to be confirmed that the length of the complete cathode feed-through system is adjusted correctly. The bellow should be under small bending stress ensuring that the cathode nozzle is sitting tightly in the ceramic (4). Otherwise the nozzle is able to move freely in the ceramic and the distance between the cathode and the skimmer plate is changed in comparison to its initially set value.

3.2.4.2 Data acquisition

A flow-chart (Figure 3.9) summarizes how data acquisition of the different electron spectroscopy methods is achieved.

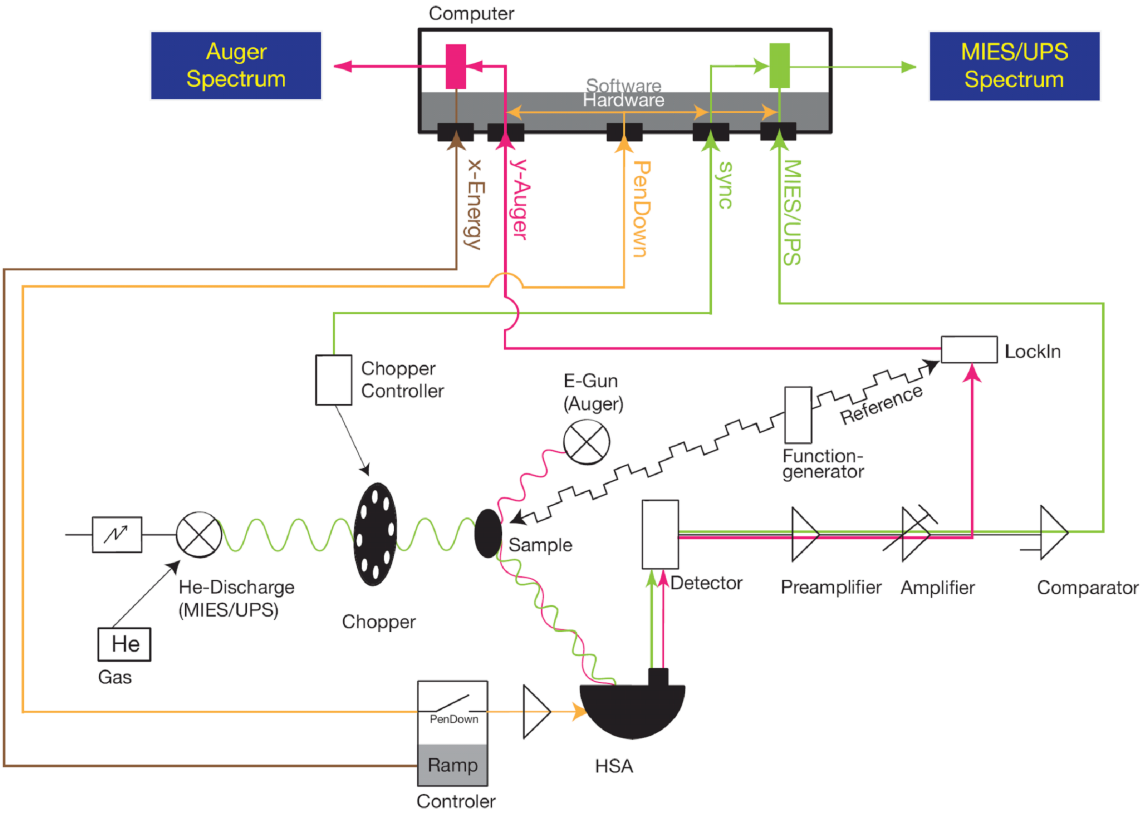

Figure 3.9 Scheme of the data acquisition of the different electron spectroscopic methods applied in the nanocatalysis laboratory.[83]

For MIES/UPS the source (discharge lamp) produces metastable atoms and photons which are guided through a chopper. The controller of the chopper motor creates a synchronization signal, which is sent to the data recording computer. After the interaction of the photons and metastable helium atoms with the surface of the sample has occurred, some ejected electrons enter the hemispherical analyzer (HSA). Only electrons of a given energy (the so-called pass energy, PE) are allowed to arrive at the detector slits. At the detector the signal is then passed through a preamplifier, an amplifier and a comparator. Finally, the signal is recorded by the data acquisition computer.

When the measuring ramp of the hemispherical analyzer is started a “PenDown” signal is sent to the computer. This allows synchronizing the analyzer with the chopper, since both are recorded by the data acquisition computer. The data recording is achieved by means of an in-home design LabView program.

3.2.4.3 MIES/UPS post-detection data treatment

As discussed in chapter 3.4.3, the general idea of UPS and MIES signal detection was to separate the signals via the use of TOF separation (see Figure 3.7). However, the conditions for the use of the TOF separation could not be achieved in the nanocatalysis laboratory setup.

Specifically, the distance between chopper and sample (crystal) was too short to perform a TOF separation as previously presented in Figure 3.7. The ratio of pumping is different as well; the nanocatalysis setup exhibits a lower pumping speed resulting from a bigger chamber volume. In light of this, the same pressure conditions are not achievable.

To overcome the problem that the typical time of flight separation posed, a new measurement approach has been developed. The idea of the new method is that the shape of the UPS signal is determined by the chopper frequency. Thus, if the two signals are mixed together in a controlled way the UPS signal can be subtracted from the sum-signal. The premises for the successful application of this method are as follows:

1. The UPS signal has to reach its saturation level before the MIES signal starts. When the rising edge is known the UPS signal can be calculated.
2. It must be ensured that each of the mixed UPS/MIES signals is followed by the gate where no counts are detected. Otherwise the UPS signal can not be extracted properly, as it is always perturbated by a MIES background.

For the nanocatalysis setup a chopper frequency of 900 Hz is the right value for a successful realization of the above described data analysis.

The software interface shows a window in which a couple of frames are added. In order to extract the two spectra the beginning of the signal has to be set manually (see window 2).

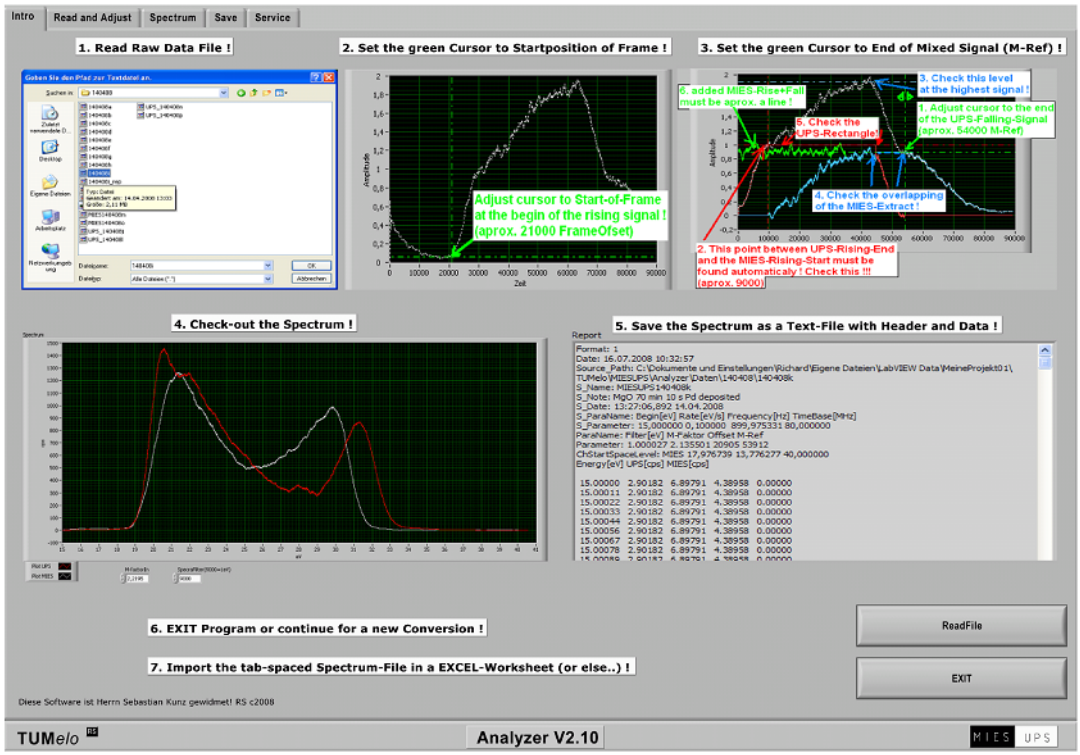

Figure 3.10 Screenshot of the data treatment program interface. The different steps that have to be accomplished to obtain a meaningful spectrum are explained in the corresponding text frames.

In window 3 the end of the UPS signal has to be defined. It can be identified as the end of the trailing edge. Two guide lines, described in the software, help to set the two points correctly. Based on this procedure the correct spectra can be extracted from the raw data without the use of a real TOF separation. The method offers an additional advantage by using the whole signal for the data analysis. The application of the real time of flight technique, in comparison, is limited to small windows, which have to be set to avoid the signals influencing (cross-talking) each other.

In conclusion, it can be said that the TOF separation failed in the nanocatalysis laboratory due to the above mentioned reasons. However, by developing a new measuring technique the problem could be overcome.The electron yield for UPS as well as MIES could additionally be increased, since the new method allows the extraction of each signal from the sum signal without any losses.

3.2.5 AES

In order to emit Auger-electrons from the sample, an electron gun is used. The electrons are guided to the surface of the sample via ion optics. The electrons, which have been emitted from the surface, are detected after passing through the same hemispherical analyzer as discussed previously. The signal then passes through a preamplifier and an amplifier before reaching the LockIn amplifier. Using a function generator, a 3 V AC voltage is applied to the sample. Furthermore, the generated signal is sent as the reference for the electrons to the LockIn amplifier. When the phase of the LockIn amplifier is adjusted with respect to the electrons emitted from the surface, the amplified signal is recorded by the same data acquisition computer used for MIES/UPS. A “PenDown” signal is generated and sent to the computer when a measurement is started, setting the start of the data recording by the computer simultaneously. The data acquisition is achieved by an in-house-designed LabView program.

It should be mentioned that an Auger-spectrum is always presented as the first derivative of the electron intensities, since the desired Auger peaks appear on top of an intensive secondary electron shoulder.

3.2.6 Hemispherical analyzer

The intensity of the emitted electrons with respect to energy of the electrons is recorded by the same hemispherical analyzer (HSA) (VSW Scientific Instruments Ltd., HA150) for all three electron-spectroscopy methods. However, there are two different operation modes: The fixed analyzer transmission (FAT) is used for MIES/UPS whereas the fixed retarding ratio (FRR) is used for AES.

For spectra recorded in the FAT modus, the arriving electrons are slowed down or accelerated by a variable counter field at the entrance of the analyzer. The so called pass energy E_0 is kept constant, thus the energy resolution ΔE is constant, too. The pass energy for MIES/UPS in this work was set to $E_0 = 10$ eV and the scan rate was 0.1 eV / s .

In the FRR mode the analysis is performed by varying the pass energy. This is realized by a constant entrance field generated by the lens system, which keeps the retardation factor $R = \frac{E_{kin,A}}{E_0}$ constant.

3.2.7 TPD/TPR (temperature programmed desorption / temperature programmed reaction)

TPD/TPR experiments are performed using a commercial quadrupole mass spectrometer (Balzers QMG 421). The crystal is placed close to the front of the mass spectrometer, minimizing the distance that the desorbing molecules have to travel to reach the detector of the QMS. A voltage of -150 V is applied to a skimmer, which is mounted in front of the spectrometer to avoid electron-stimulated desorption. To ensure that the reactants are pumped off as fast as possible, the mass spectrometer is additionally pumped by a 60 L / s Pfeiffer turbo pump (TMU 071P).

The crystal is heated resistively by the output of a power supply (HP-6032A), which is checked by a temperature controller (RHK Technology, TM 310). The temperature controller is triggered by a home-built LabView program. The thermocouple signal of the temperature controller is sent to the QMS, where it is monitored by the mass spectrometer software (Balzers, Quadstar 421 Version 2.0). During the presented work the temperature controller broke down and a new system has been installed, which was not applied in the experiments presented in this work.

The voltage signal measured by the thermocouple is converted into the real temperature by a DAT 4135/AC DATEXEL converter. The signal is sent to a Eurotherm PID controller (2404/2408) and displayed. The controller is connected to the same power supply which has been used before (HP-6032A) in order to heat the crystal. The mass spectrometer records the temperature signal during the measurement for TPD/TPR experiments.

3.2.8 Molecular beam doser

Molecules for TPD/TPR and MIES/UPS experiments can be dosed onto the sample using a doser, which is positioned underneath the skimmer of the mass spectrometer. The doser consists of a metal tube which is connected to the gas-line (see at the right side of Figure 3.2). It can be separated from the gas-line by closing a valve and pumping by a turbopump after opening a second valve. The doser is in principle a small gas reservoir that can be filled with a certain gas at a given pressure and be pumped by a turbopump in order to evacuate it. The doser has a small hole at the front end, so that depending on the pressure that is set in the gas-line a certain flux can be achieved. The pressure in the gas-line is measured by a baratron with an accuracy of ±1mTorr .
The doser has been calibrated previously so that the flux can be calculated for a given molecule mass, back pressure and time, using the following equation:[101]

$$dN = 2.5 \cdot 10^{13} \cdot p_G \Delta t \frac{1}{\sqrt{m}} \qquad (3.1)$$

In the presented work the dosage is given in the unit of monolayer ML, whereas one ML is related to the amount surface atoms of a MgO surface, which is $2.25 \cdot 10^{15}$ atoms / cm^{-2}.

3.2.9 Pulsed molecular beam reactive scattering (p-MBRS) experiments

In order to determine the reactivity of mass-selected clusters, two pulsed molecular nozzles are attached to the main chamber. In a reactivity study the reactants are pulsed onto the surface of the model catalysts under isothermal conditions and the product molecules are recorded by the same mass spectrometer (Balzers QMG 421) as used for TPD/TPR experiments.The software supplied with the QMS cannot be used in these experiments, because of its slow response time. The signal is taken from the preamp and monitored directly by a stand-alone storage oscilloscope.[108]

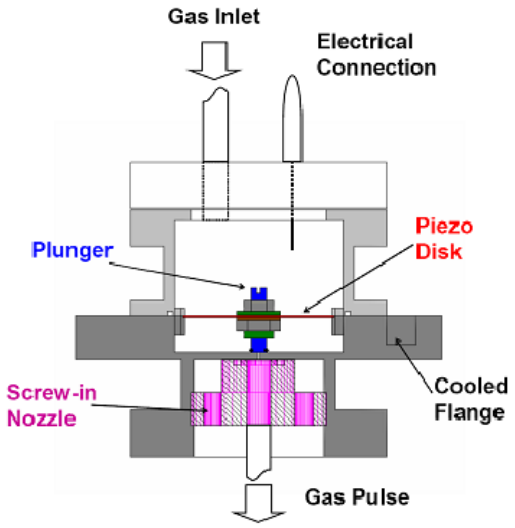

Figure 3.11 Sketch of a pulsed valve. The plunger is sitting on a pin hole. If a voltage is applied, the piezo disc bends, the pin hole is not sealed by plunger and a certain amount of gas from the reservoir is dosed onto the surface.

The construction of a pulsed valve (PV) is shown in Figure 3.11. The two PVs are connected to the same gas-line that is used for the reactant dosage in TPD/TPR experiments and oxygen dosage during the MgO film preparation. The main part is a piezo element glued onto a round-shaped, thin titanium plate. A plunger with a small, hard viton gasket is screwed onto the piezo disc so that the viton gasket seals a pin hole that connects the PV via the screw-in nozzle with the main chamber.[109] A cable is soldered onto the piezo element and connected to a feed-through. A potential can be applied to the PV with respect to the ground (main chamber), which leads to a bending of the piezo element. The viton gasket is moved back from the pin hole and the reactants flow through this hole into the main chamber. A home-built piezo-pulser is used in order to apply short pulses (20–800 µs) up to frequencies of 120 Hz. The most difficult aspect of the pulsed valve setup adjusting the screw appropriately. The plunger must sit on the pin hole, so that it seals the PV and no leaking occurs; however, if it is fixed too tight, the movement of the piezo element is too short to allow an opening of the viton gasket.[101]

In terms of this PhD project the pulsed valve setup has been improved in order to enable the use of high frequency pulses. As mentioned previously the pulsed valves were connected to the old gas-line setup in order to supply them with the reactant gas. In order to achieve stable conditions a high back pressure had to be set, because then the amount of gas taken from the reservoir is small and the change of the back pressure can be neglected.

This led to pulses of large amounts of reactants with respect to the pressure conditions of a UHV setup. An increase in pressure of up to 10^{-6} mbar per pulse was observed.

If a constant low back pressure is to be realized a different approach must be applied. Therefore, a small chamber behind the pulsed valve was built, which is continuously pumped by a turbo pump. This allows the generation of a low pressure in the chamber. However, the gas flux in the chamber must still be controlled so that the pressure in this chamber becomes tunable, because the turbo pump has a constant pump rate. The problem was solved by applying a gas flux regulator.

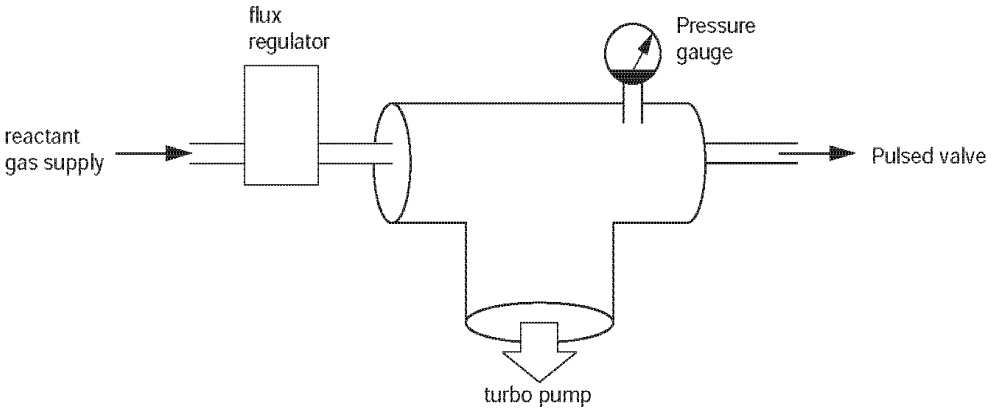

Figure 3.12 Sketch of the continuously pumped gas reservoir system that has been developed within the scope of this work. Depending on the settings of the flux regulator, a low back-pressure can be achieved for the pulsed-valve, since the chamber is pumped by turbo pump.

For the final solution a stainless steel T-piece was chosen as the chamber body, with a Varian turbo pump (TV 81-M) attached to it. The two remaining flanges are connected to one of the pulsed valves at one side and to a MKS (1179B11CR1BV) 10 sccm flux regulator on the other side. The pump is running continuously and a pressure of low 10^{-7} mbar is reached in the chamber (without bake-out). Under operating conditions a gas bottle behind the flux regulator is opened and the pressure in the T-piece is adjusted by tuning the flux of the gas. This setup allows one to manipulate a flux through the system that is high enough, to enable a constant flux for each pulse through the pin hole into the main chamber, when the PV is pulsing.

3.2.10 Infrared-Reflective Absorption Spectroscopy (IRAS)

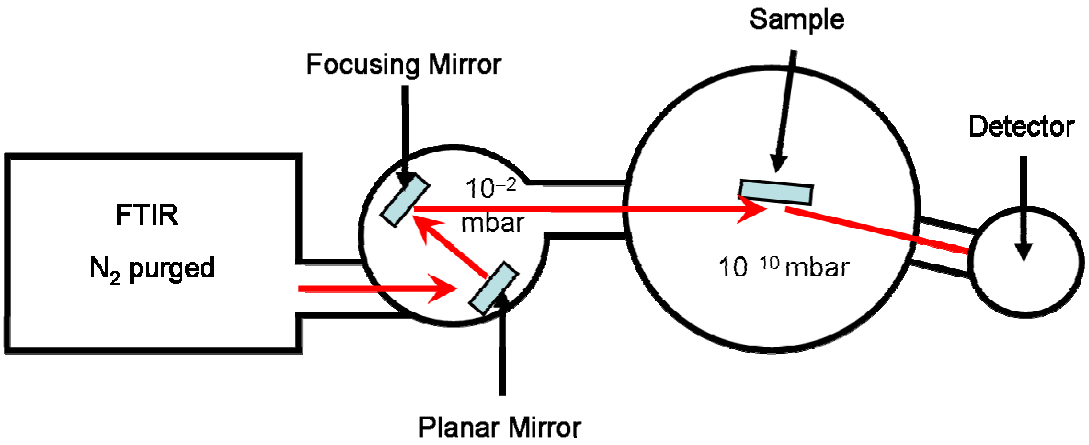

Figure 3.13 IRAS setup used in the nanocatalysis laboratory. The beam is guided from the nitrogen purged spectrometer into a small chamber, which is pumped to 10^{-2} mbar and that contains two mirrors. The second mirror is a focussing so that the beam is focussed onto the sample. The reflected beam is guided into the detector.

IRAS is a very useful technique in surface science to gain information about the surface structure by measuring the vibrational frequency of probe molecules that are adsorbed on the surface.

The nanocatalysis laboratory includes a Thermo Nicolett FTIR spectrometer, which is used in an external mode. The optical path of the IR beam is illustrated in Figure 3.13. The spectrometer is nitrogen purged; the ejected beam is guided into pumped chamber (10^{-2} mbar) that contains a planar mirror onto a focusing mirror. The beam is subsequently reflected from the focusing mirror into the UVH chamber (10^{-10} mbar) onto the crystal. The distance between focus mirror and sample is adjusted to fit to the focusing length of the mirror. The beam is reflected from the crystal into the external detector, where it is recorded by the spectrometer software.

3.3 Transfer system

On the right side of the apparatus the cluster beam enters a mass-spectrometer with a mass limit of 9000 amu, after leaving the bender. Subsequently, after passing a stack of Einzel lenses the clusters are deposited onto the surface of a given sample. The sample is mounted

onto a rotatable, motor-driven sample holder, which is electrically insulated from the vacuum setup. Thus, a voltage can be applied to the sample in order to accelerate the clusters to the surface. Furthermore, the neutralization current of the cluster beam can be measured and the cluster coverage estimated.[110]

After deposition has been completed, the cluster sample is driven into a vacuum lock. The vacuum lock is separated from the preparation chamber via a pneumatic gate. The vacuum lock itself is pumped by a turbo pump that can be separated from the lock, via a vacuum gate valve. Thus, the lock can be separated from all pumps and subsequently vented allowing the removal of the prepared samples. Using this experimental setup, cluster depositions can be performed continuously and extremely efficient without breaking the vacuum.

3.4 Three electrode setup

An electrochemical cell consists normally of two electrodes. One acts as the cathode[1] and the other as the anode[2].[111] If the two electrodes are connected electrically a current flows leading to a chemical reaction and a galvanic cell is generated that can be used to gain energy. If a potential is applied, the reaction is reversed and electric energy is converted into chemical energy; at both electrodes reactions occur when a current flows. Usually one focuses on a specific cell-reaction and thus, a standard electrode has to be used in order to allow comparison of the single cell reactions.[112]

The value of interest is the potential at a given current for a specific cell and its reaction. However, if a current flows the measured potential includes contributions from the overpotential of both electrodes and the solution. In order to overcome this problem and to measure just a half-cell reaction, a three electrode setup is applied, consisting of the working electrode (the sample), an auxiliary electrode (for the second cell reaction to establish a current flow) and a reference electrode (to determine the potential at zero current). At typical setup and its circuit diagram are shown in Figure 3.14.

[1] The cathode is the electrode at which reduction occurs.
[2] The anode is the electrode at which oxidation takes place.

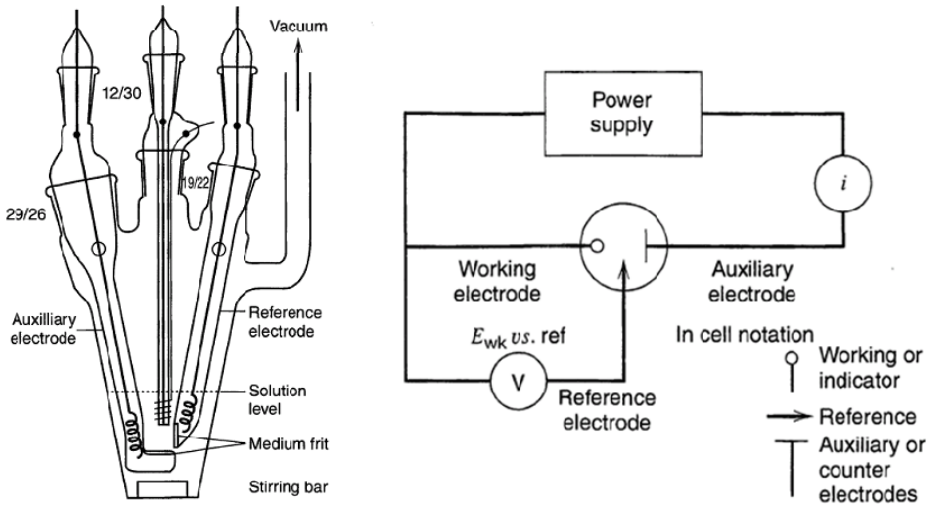

Figure 3.14 A typical three-electrode setup (left) with is corresponding electric circuit diagram (right).[113]

The device used to measure the potential difference between the working electrode and the reference electrode has a high input impedance, so that a negligible current is drawn through the reference electrode. Consequently, its potential will remain constant and equal to its open-circuit value.

One important source of error during the measurement is the fact that a voltage drop will appear in the electrolyte arising from Ohm's law as seen in Figure 3.15.

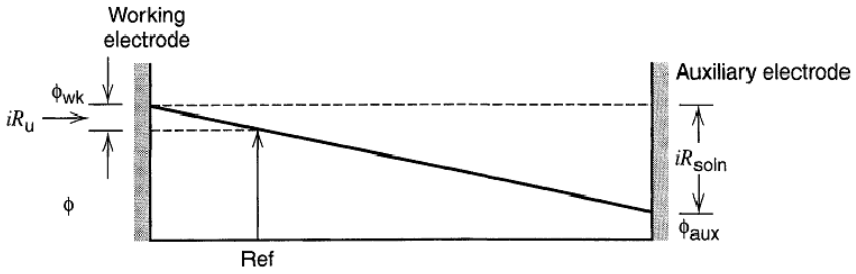

Figure 3.15 Voltage drop appearing between two electrodes in an electrolyte.[113]

From this sketch it can be seen that the reference electrode should be placed as close as possible to the working electrode to avoid the detection of additional potential differences arising from the electrolyte.

To achieve this requirement, the working electrode and the reference electrode are connected by a Haber-Luggin capillary that is placed close to the working electrode surface.[113]

4 The effect of CO poisoning on the reactivity of small size-selected Pd_n (n = 8, 13, 30) clusters.

4.1 Experiments and results

As mentioned in chapter 2.1.3 the effect of CO poisoning on small mass-selected palladium cluster has been investigated by means of TPR, p-MBRS experiments and IRAS. In the following the results of the experiments as well as the experimental procedures will be described.

4.1.1 TPR

The technical details of TPD/TPR experiments have been discussed previously in chapter 3.2.7. In the context of this work TPR experiments for Pd clusters have been performed in two different ways.

Procedure 1:

1. O_2 dosage at 100 K.
2. CO dosage at 100 K.
3. Temperature ramp from 100 K to 700 K.

Procedure 2:

1. CO dosage at 100 K.
2. O_2 dosage at 100 K.
3. Temperature ramp from 100 K to 700 K.

In Figure 4.1 the detected CO_2 signal intensities of Pd_{30} (representative for different cluster sites) are plotted with respect to the temperature. The results for procedure 1 are shown as a green curve, whereas procedure 2 is plotted in blue.

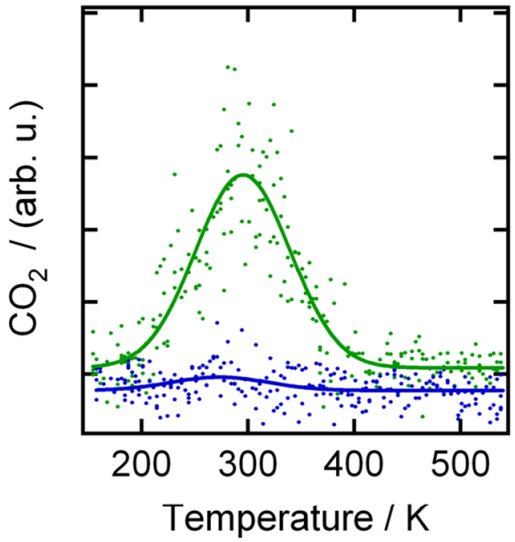

Figure 4.1 TPD spectra of the two different procedures described in the text. The green curve represents a TPD for oxygen precovered clusters. No CO poisoning can be observed for this procedure. The blue curve represents a TPD for CO precovered clusters. CO poisoning occurs.[114]

For procedure 1 it can be seen that a CO_2 signal appears around 200 K, it reaches a maximum at 300 K and vanishes completely from 400 K on.
However, if the reactants are dosed in the order described as procedure 2, nearly no signal is observed over the complete temperature range.

4.1.2 p-MBRS (at isothermal conditions)

The reactivity under isothermal conditions has been investigated using p-MBRS experiments, as described in chapter 3.2.9. Both reactants (CO and O_2) were pulsed alternately with a frequency of 1/3 Hz and a phase shift of π. The total amount of reactants pulsed onto the surface was identical and more than $5 \cdot 10^{15}$ molecules/pulse was used to ensure that the surface of the catalyst was fully saturated by each reactant pulse. Consequently, an oxygen pulse strikes onto a CO precovered clusters and an oxygen pulse strikes onto a CO precovered clusters. In both cases is CO_2 formed and the signals originating from either CO precovered clusters or oxygen precovered clusters is recorded by an oscilloscope. A typical example for two pulses is given in Figure 4.2 that shows a CO_2 signal originating from a CO pulse onto oxygen precovered clusters and a second signal which arises from an oxygen pulse that strikes onto CO precovered clusters.

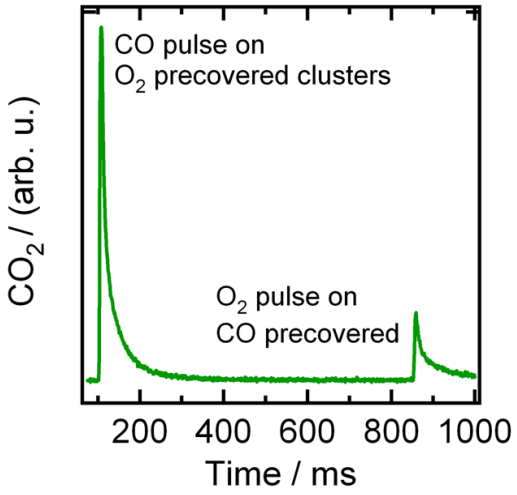

Figure 4.2 Representative CO_2 pulses obtained for oxygen precovered clusters (right) and CO precovered clusters (left).

10 pulses were recorded and baseline-corrected. The integral of the averaged pulse was calculated as the magnitude of the CO_2 intensity and the uncertainty of the integral was determined as the error for the data treatment procedure. It should be mentioned, that the first three to four pulses were neglected, because they differ extremely in intensity and thus no constant experimental conditions were reached. Two possible reasons are: either the steady state conditions are not fulfilled in the beginning of the experiments or the piezo disc has to warm up, so that the gas flux becomes equal for each pulse.

All experiments were carried out at constant temperatures so that the reactivities were determined for isothermal conditions. The results are presented in Figure 4.3.

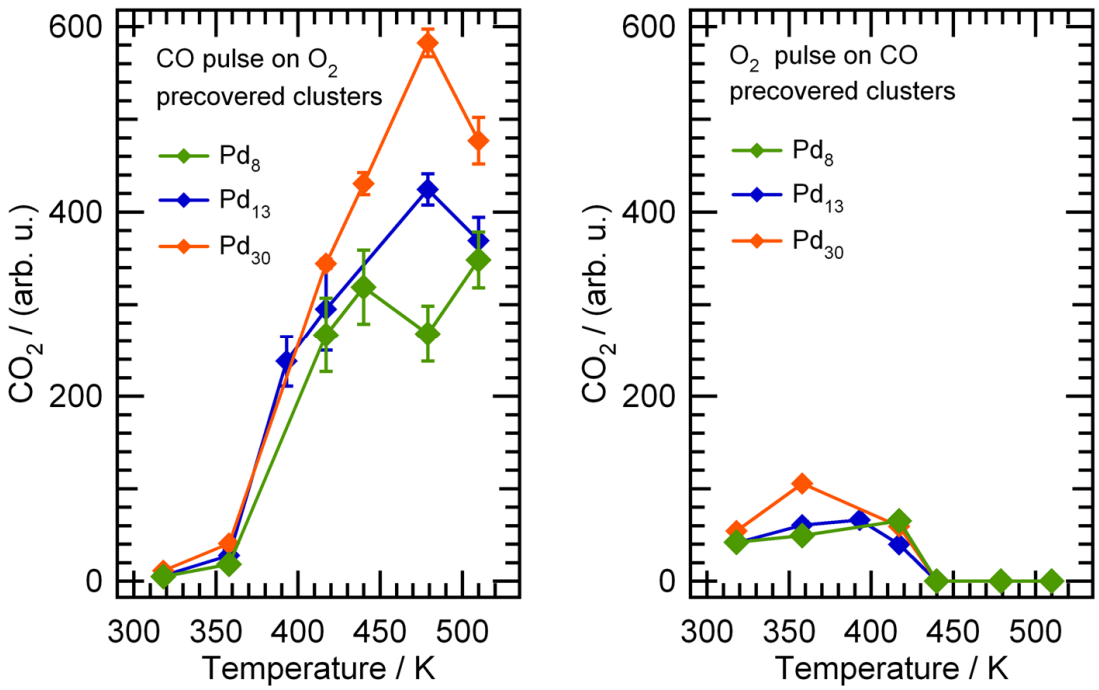

Figure 4.3 Pulsed molecular beam experiments of various cluster sizes (Pd_9, Pd_{13}, Pd_{30}) at different temperatures; CO pulse on oxygen precovered clusters (left). Oxygen pulse on CO-precovered clusters (right).[114]

On the left side the reactivities elucidated for oxygen precovered clusters are presented. For the different cluster sizes no signal is observed at temperatures around 300 K. The CO_2 yield starts to appear around 360 K and increases sharply from this temperature on. Measurements above 500 K were not performed, because cluster agglomeration can not be excluded at these temperatures.

The right side of Figure 4.3 shows the CO_2 yield for an oxygen pulse striking onto CO precovered clusters. Even at low temperatures (300 K) CO_2 is detected and the amount remains nearly constant up to a temperature around 420 K. Above these temperatures the signal vanishes and no CO_2 is detected anymore.

A comparison of the two graphs with each other shows that the CO_2 yield at low temperatures is higher for CO precovered clusters in comparison to the oxygen precovered. However, the situation changes above 360 K and for higher temperatures the oxygen precovered clusters show much higher CO_2 yields, while the CO precovered clusters are not reactive.

4.1.3 IRAS

In addition to the above described TPR and p-MBRS experiments, IRAS measurements have been performed to verify the temperature dependency of the CO adsorption properties on small palladium clusters. Representative results for Pd_{13} are shown in Figure 4.4.

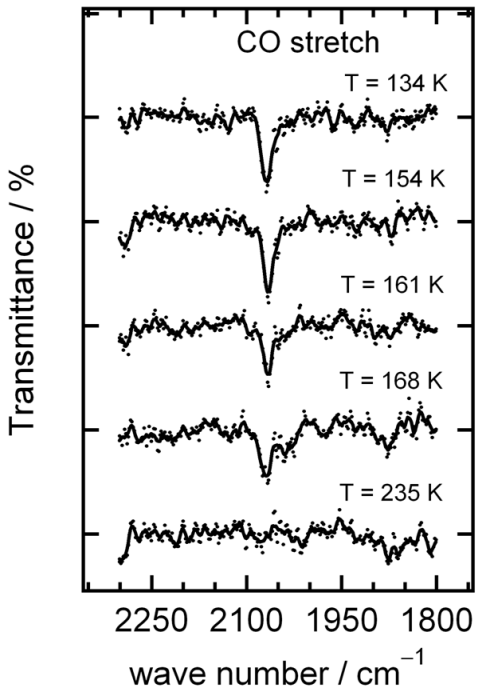

Figure 4.4 Spectra of CO adsorbed on Pd_{13} clusters annealed to different temperatures. All spectra were recorded at 100 K.

The experiments have been carried out as followed: CO was dosed at low temperatures (100 K) and a spectrum was recorded. Then the temperature was increased to 156 K for 10 s. Afterwards, the sample was cooled down to ≈ 100 K and the spectrum that is assigned to 156 K was recorded. The same procedure has been applied for the other temperature dependent spectra. At low temperatures only one band is observed (≈ 2060 cm^{-1}) that can be related to linearly bonded CO. The signal intensity starts to decrease from 161 K on and disappears completely at 235 K. At 168 K a signal seems to appear around 1970 cm^{-1}, which can be related to bridge bonded CO.[115] However, since the signal to noise ratio is quite low, this band should not be stressed.

In conclusion, most CO is linearly bonded and desorbs at relatively low temperatures, because the adsorption strength is weak.

4.2 Discussion

TPR experiments have shown that the order of reactant dosage influences the outcome of the experiment. When oxygen is dosed first and CO second (procedure 1), a CO_2 signal in the range between 200 and 400 K was detected, whereas if CO is dosed first and oxygen second (procedure 2) no signal is observed.

The adsorption strength of the two reactants on MgO is quite low (0.1 eV for oxygen and 0.4 eV for CO). At dosing temperatures of approximately 100 K no oxygen sticks on MgO and TPD studies of CO on MgO have shown that CO desorbs below 100 K.[116, 117] Thus, it can be assumed that the reactants adsorb exclusively on the clusters and not on the support. This means that reverse spill-over effects are neglected in the following discussion.

It should be taken into consideration that CO is known to adsorb via chemisorption on palladium with high heats of adsorption (150 kJ/mol), as well as oxygen, which adsorbs molecularly at low temperatures and dissociatively at higher temperatures.

If oxygen is dosed first, it will adsorb in a molecular state on the clusters, because the dosage temperature is low. When CO is subsequently dosed, it can adsorb for two reasons, either the molecularly adsorbed oxygen does not form a dense layer[1] or some weakly adsorbed oxygen gets substituted by CO.[68] It is certain that both reactants are present on the clusters after the dosage procedure, because the TPR experiment shows that CO_2 is formed.

In contrast the second dosage procedure shows no CO_2 formation. When CO is dosed on the bare palladium clusters it adsorbs molecularly. From single crystal studies it can be concluded that CO adsorbs with the carbon atom bonded to the metal surface and the oxygen atom pointing in the opposite direction.[118] Thus, it forms a closed, dense layer on the clusters. In contrast to CO, oxygen needs more space to adsorb and a closed CO layer does not offer any free adsorption sites for oxygen. Thus, at low temperatures a CO poisoning effect is observed in TPR experiments.

[1] because it adsorbs with the bonding axis parallel to the surface, hence it needs a lot of space and can not form a close-packed layer

In comparison to TPR, p-MBRS experiments give more insight into mechanistic details at elevated temperatures. The reactivity measured for oxygen precovered clusters allows examination of the oxygen activation on small metal clusters, because the CO pulse strikes oxygen saturated clusters. Thus, the CO_2 yield depends exclusively on the oxygen activation properties of the clusters. At low temperatures (300 K) no CO_2 is detected. From this it can be concluded that no oxygen activation occurs in this temperature regime. However, around 400 K the detected CO_2 amount increases drastically. Similar experiments have been performed for palladium single crystals. In a molecular beam study a constant oxygen background generated an oxygen precovered single crystal surface.[54] At a certain time *t* a molecular CO beam is switched on and the CO_2 yield is measured as a function of the time *t*. The initial CO_2 rate can be used to compare the observed cluster properties with single crystal properties. The results for both model systems are presented in Figure 4.5 for comparison.

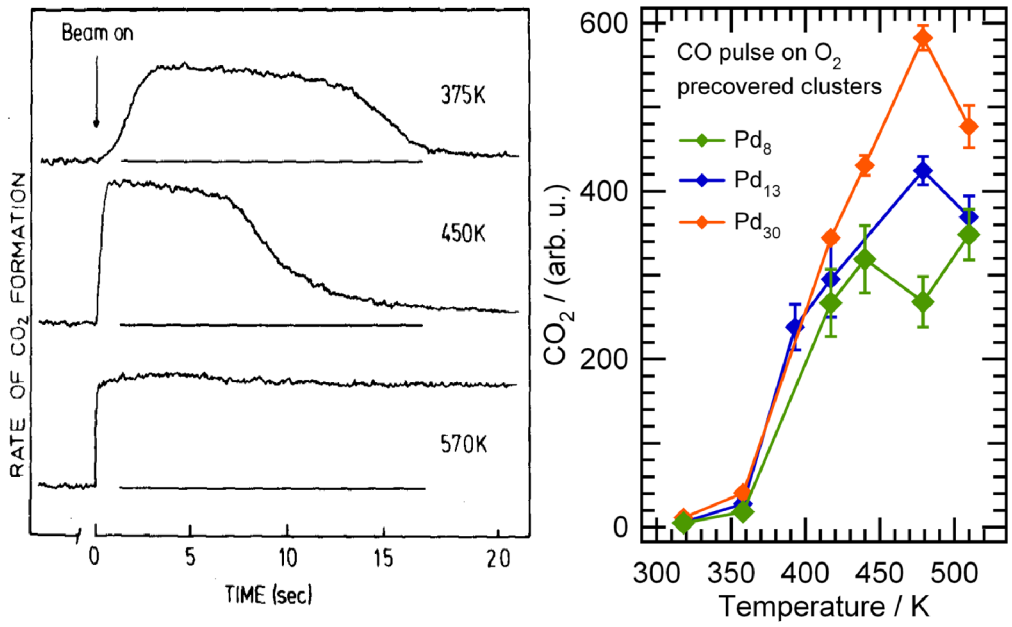

Figure 4.5 Comparison of time dependent CO_2 signals of an oxygen precovered Pd(111) single crystal and size-selected Pd clusters.[54, 114]

For both systems no CO_2 yield is measured at low temperatures. However, at temperatures around 450 K high CO conversion rates are measured for each catalyst. Another plot that allows for a good comparison of both systems is the maximum CO_2 rate at different temperatures as shown in Figure 4.6.

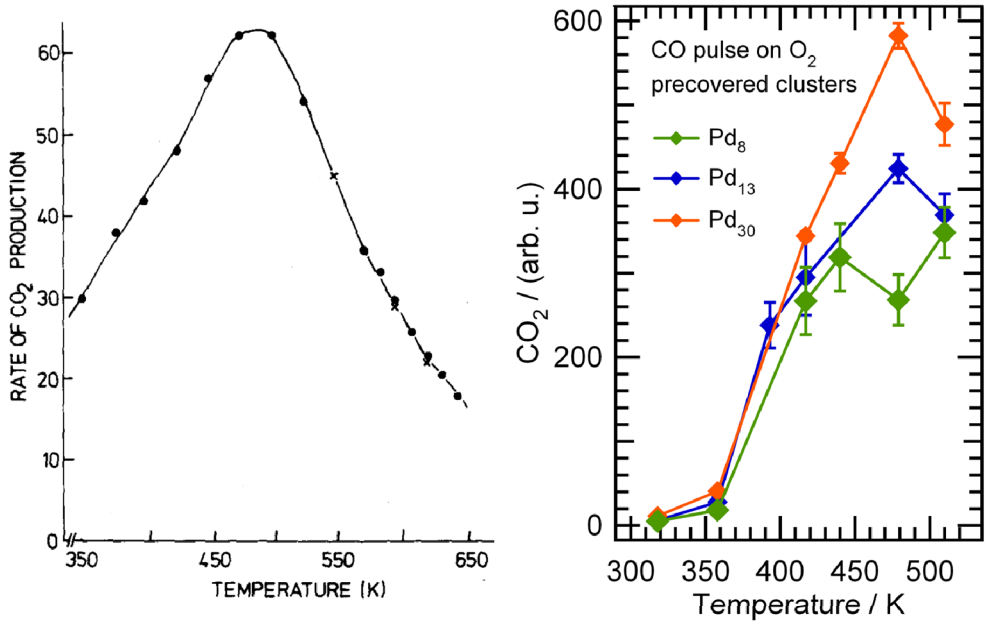

Figure 4.6 Comparison of maximum CO_2 rate determined for a Pd(111) single crystal from figure 4.5 with the integrated CO_2 of size-selected clusters.[54, 114]

Comparison of the two figures shows that the reactivity trend obtained for oxygen precovered Pd clusters is similar to the one observed for a Pd single crystal.

It has been shown for single crystals that oxygen is activated via dissociative adsorption, which depends on the temperature, because dissociation is an activated process with a distinctive activation barrier. From Figure 4.6 the same behavior is observed for cluster and single crystals, showing that oxygen activation occurs on clusters via dissociative adsorption at temperatures around 400 K, too.

In the next step CO precovered clusters are compared with a CO precovered single crystal. The chosen experiment to compare the two model systems has been performed in a similar way as the aforementioned experiment, but the order of the reactants is changed. A constant CO background is set and a molecular oxygen beam is switched on at a certain time *t*. Again, the initial CO_2 rate is used to compare the cluster experiments with single crystals. Figure 4.7 illustrates the results of the measurements.

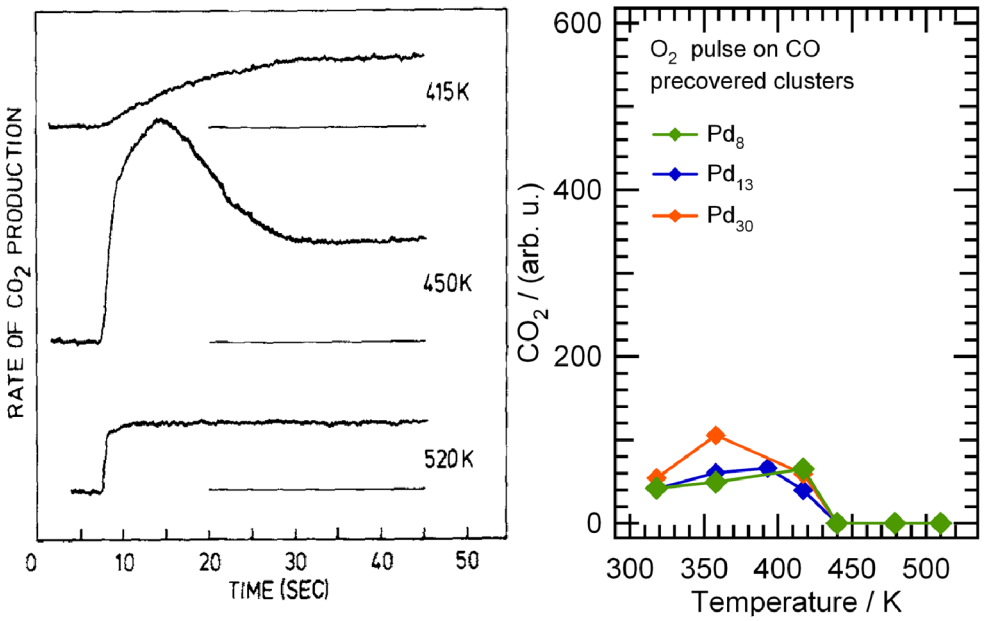

Figure 4.7 Time dependent CO_2 signal detected for a CO precovered Pd(111) single crystal and size-selected Pd clusters.[54, 114]

CO_2 is detected for small metal clusters at low temperatures up to 415 K. Above these temperatures no CO_2 is detected and it is assumed that no CO sticks on the clusters above 415 K. In contrast the single crystal studies show that at 415 K the CO_2 rate is strongly attenuated if the surface is precovered with CO and it takes a long time until the steady state is reached. At 450 K a transient regime is reached, however, the CO lifetime on the surface is still long and it takes even higher temperatures to avoid CO poisoning. Thus, it can be concluded that CO exhibits a weaker adsorption strength on clusters than on single crystals. The weak CO-cluster interaction has been additionally proven by IR spectroscopy. This fact results in a shift of CO poisoning to occur at lower temperatures on small metal clusters in comparison to single crystals.

The reactivity of a given catalyst for CO oxidation is determined by the following two key factors: Oxygen activation and CO poisoning

For a single crystal it can be concluded that oxygen activation occurs around 400 K and CO exhibits a long lifetime on the surface up to more than 450 K. Thus, although a single crystal would be reactive at temperatures around 400 K, because it activates oxygen, this regime is overlapped by CO poisoning, inhibiting the catalyst reactivity. These conclusions are summarized in the following sketch (Figure 4.8).

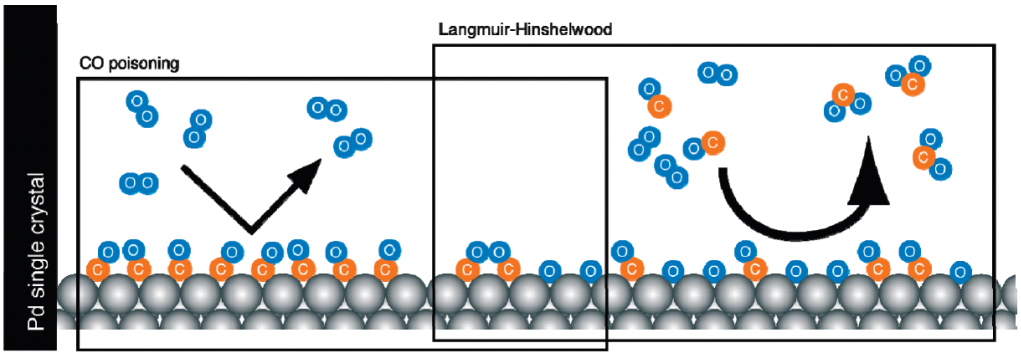

Figure 4.8 Temperature regimes can be defined for CO poisoning and oxygen activation. The regimes overlap for the case of a single crystal.

At temperatures above the CO poisoning limit CO oxidation occurs via the Langmuir-Hinshelwood mechanism. Oxygen adsorbs and dissociates, CO adsorbs as well, CO_2 is formed on the surface and subsequently desorbs.

For clusters the same oxygen activation properties are obtained, but CO poisoning is shifted to lower temperatures. The question then arises what happens at temperatures, where no oxygen activation or CO poisoning occurs?

In Figure 4.7, one sees that a reactivity is obtained at these temperatures ($T \leq 360$ K), however, only for CO precovered clusters. This leads to the conclusion that CO is involved in the activation of oxygen at low temperatures and that the mechanism differs from the normal Langmuir-Hinshelwood mechanism. This picture is additionally confirmed by a TPR study. One of the TPR spectra is shown in Figure 4.9; three CO_2 peaks can be identified.[119]

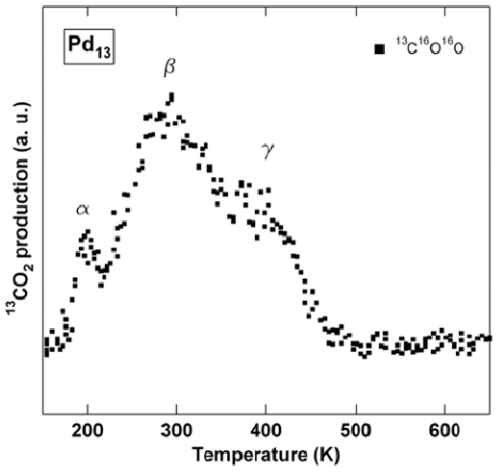

Figure 4.9 TPR spectrum of Pd_{13}. Three peaks can be identified.[119]

The gamma peak is assigned to the normal Langmuir-Hinshelwood mechanism which involves dissociation of oxygen; whereas the beta peak is originating from the same reaction mechanism observed in the p-MBRS measurements at low temperatures on CO precovered clusters.

Since CO must be present on the cluster surface to enable oxygen activation the mechanism is specified as a cooperative Langmuir-Hinshelwood mechanism. Two border cases are suggested:

1. CO interacts with molecular adsorbed oxygen and supports the dissociation of the oxygen bond. This is denoted as the direct promotion.
2. CO affects the cluster morphology or its electronic structure in a way that an adsorption site is generated on which oxygen activation occurs via dissociation.

The conclusions drawn for small metal clusters are summarized in Figure 4.10:

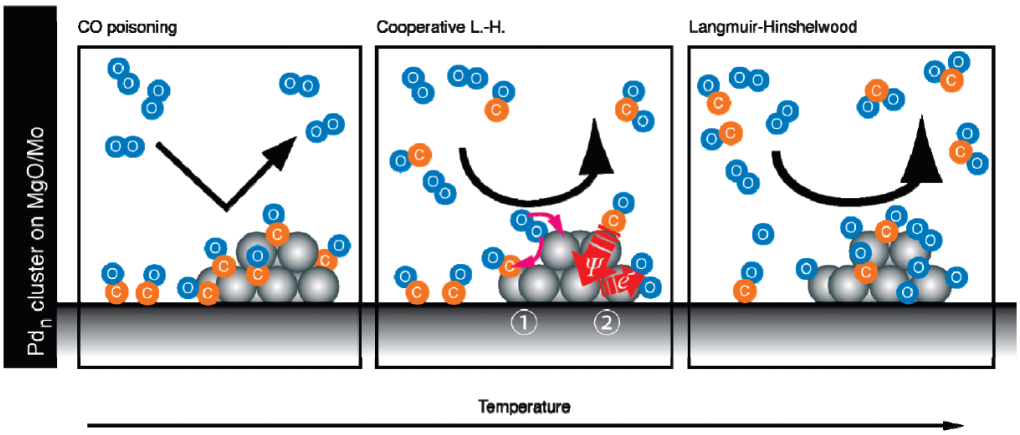

Figure 4.10 For small size-selected Pd clusters the temperature regimes for CO poisoning and oxygen activation do not overlap. Furthermore, an additional reaction window between the two different regimes opens up. (1) illustrates a "direct promotion" mechanism and (2) an "indirect promotion" mechanism.

At low temperatures the clusters are covered with CO, blocking the surface for oxygen adsorption. Consequently, the clusters are poisoned and no CO oxidation occurs. At higher temperatures, CO desorbs and free adsorption sites become available for oxygen adsorption. Nevertheless, CO must be present on the cluster surface to activate oxygen either via direct promotion (1) or indirect promotion (2), leading to a cooperative Langmuir-Hinshelwood mechanism. At temperatures above 400 K atomic, reactive oxygen is formed via dissociative adsorption on the clusters and thus, a typical Landmuir-Hinshelwood mechanism is observed.

4.3 Conclusion

It has been shown that small palladium clusters are active for CO oxidation over a broad temperature range. At high temperatures the reaction mechanism is assumed to be of Langmuir-Hinshelwood type, like that seen for palladium single crystals. Comparing the reactivity over a broad temperature range with the reactivity of single crystals shows that CO poisoning occurs on clusters as well, however, since the adsorption strength of CO is weaker on clusters CO poisoning takes place only at low temperatures. Due to this shift in temperature a reaction window is opened up, as seen in the middle of Figure 4.10, which seems to follow a different mechanism. This has been specified as a cooperative Langmuir-Hinshelwood mechanism.

5 Microkinetic simulations of mole fraction dependent reactivity properties of size-selected Pd_{13} clusters

The reactivity of Pd_{13} clusters has been studied with respect to the mole fraction of the reactants and the reaction temperatures.
Since these experiments have been described in detail before, they are only summarized briefly in the following chapter. In the second part, the performance of the kinetic simulations and their results are presented.

5.1 Results

5.1.1 Mole fraction dependent studies on size-selected Pd_{13} clusters

The cluster formation, their deposition and the crystal preparation have been performed, as described in chapter 3. A model catalyst of 0.47 % of a ML of Pd_{13} was prepared and the reactivity was investigated by means of a dual p-MBRS setup. Both reactants (CO and O_2) were pulsed simultaneously onto the model catalyst and the CO_2 yield was detected by a quadrupole mass spectrometer (Balzers QMS 421) and recorded by an oscilloscope (LeCroy Waverunner 6030).
As aforementioned the non-reactive reverse spill-over model only holds for steady state conditions. However, a constant reactant flux could not be achieved at the time when the experiments were performed. Thus, the peak maximum was taken as a pseudo-steady state rate, because the local pressure on the surface is high at this point and the maximum persists for more than 30 ms. The rate value was obtained by estimating the average of the measured data in the peak maximum range and standard deviation was taken as the error of the pseudo-steady state rate. A typical CO_2 signal is presented in Figure 5.1.[120]

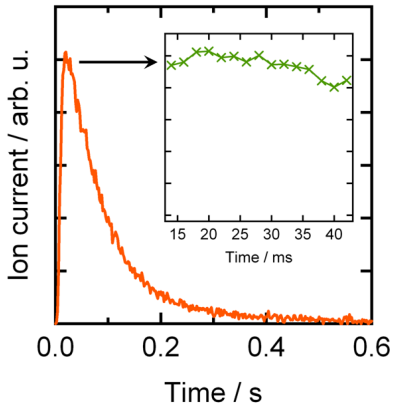

Figure 5.1 A typical CO_2 pulse recorded in mole fraction dependent measurements. The inset represents a close-up of the peak maximum.

Two values were determined in order to characterize the model catalyst's reactivity, namely the turn-over frequency (*TOF*) and the reaction probability (*RP*).

The turn-over frequency is the CO_2 production rate normalized to a characteristic value of the catalyst, e.g. the number of clusters, the real surface area of the catalyst, the catalyst mass or the reactive surface area.

In our studies the *TOF* was normalized to the total amount of deposited clusters *n* and the surface area *A* of the crystal ($A = 0.8 \cdot \mathrm{cm}^2$).

$$TOF(\mathrm{CO_2} \cdot \mathrm{s^{-1}} \cdot \mathrm{cm^{-2}} \cdot \mathrm{n^{-1}}) = \frac{1}{nA} F_{CO_2} \tag{5.1}$$

The *RP* is the ratio of the product flux (F_{CO_2}) and the reactant flux. In the presented work the CO flux (F_{CO}) was chosen as the reactant flux.

$$RP = \frac{F_{CO_2}}{F_{CO}} \tag{5.2}$$

In contrast to the *TOF*, the *RP* is a value that is dimensionless. Both values depend on the temperature and the mole fraction, however, in comparison to the reaction probability *RP*, the turnover frequency *TOF* depends on the coverage. Consequently, the *TOF* can be interpreted as a microscopic quantity, since it characterizes the reactivity of a single cluster

under given experimental conditions. In contrast, *RP* is a quantity that evaluates the reactivity of the whole catalysts without taking the cluster coverage into account and can thus be related to a macroscopic quantity. The results are presented in Figure 5.2., for both values for a model catalyst of 0.47 % ML of Pd_{13} supported on MgO/Mo(100).

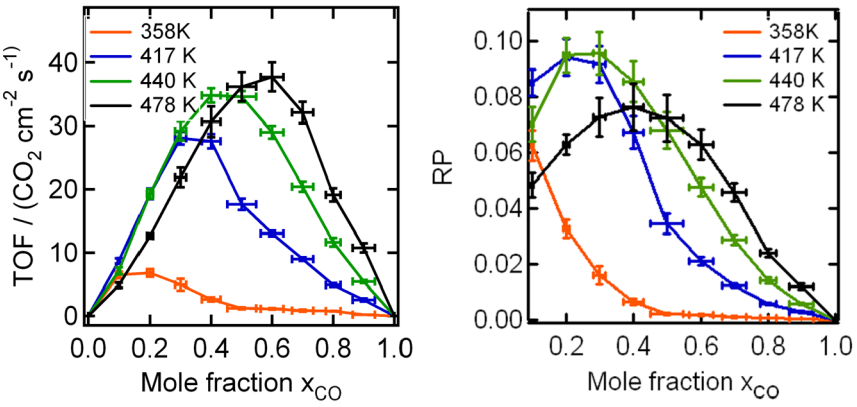

Figure 5.2 *TOF* (left) and *RP* (right) obtained for Pd_{13} clusters in mole fraction dependent measurements.[121]

From the graph illustrating the *TOFs* (left side of Figure 5.2), it can be observed that the *TOFs* increase with increasing temperatures, while the maximum is shifted to higher mole fraction values. For the highest temperature a maximum TOF value is obtained at a mole fraction of 0.6 that is close to the stoichiometry of the CO oxidation reaction.

In order to obtain *RPs*, the correct reactant flux values must be known. It has been mentioned before that the flux that strikes onto the surface does not equal the flux that reaches the clusters. Since the reverse spill-over model of Henry had been successfully applied to small metal clusters, the model was used in the mole fraction experiments in order to correct the flux that actually reaches the clusters. Thus, the reaction probability shown in Figure 5.2 is already corrected using the non-reactive reverse spill-over model.

For the *RPs* it can be seen that they do not increase continuously. The maximum value obtained for 478 K is less than the one determined for 440 K. However, the maximum of the *RPs* are also shifted to higher mole fraction values for increasing temperatures, as seen for the *TOFs*.

5.1.2 Micro kinetic simulations

Kinetic simulations of supported palladium clusters were performed using a Langmuir–Hinshelwood based formalism and solving the rate equations. Based on the work of Hoffmann *et al.* the calculations were performed in a first step for a model that describes single crystals or large facetted nanoparticles with a high surface density, since it has been shown in the past that those large particles exhibit single crystal like behavior for CO oxidation.[122]

The rate equations that were solved in the first step are,

$$r_{CO} = \eta_{CO} - k_{des}\theta_{CO} - k_L\theta_{CO}\theta_O \tag{5.1}$$

$$r_O = 2\eta_{O_2} - k_L\theta_{CO}\theta_O \tag{5.2}$$

$$r_{CO_2} = k_L\theta_{CO}\theta_O \tag{5.3}$$

with k as the rate constants, θ the coverages, r as the time dependent coverage θ of the molecule and η the flux values corrected for the reaction temperature and the coverage. The corrected flux values η are obtained as follows:

$$\eta_{CO,O_2} = F_{CO,O_2} \cdot S_{CO,O_2} \tag{5.4}$$

F_{CO,O_2} are the absolute reactant flux values and S_{CO,O_2} the sticking coefficients corrected with respect to the coverage and the reaction temperature, ($\Omega_{CO,O}$) is the saturation coverage of each reactant.):

$$S_{CO} = S_{CO,i}\left(1 - \frac{\theta_{CO}}{\Omega_{CO}} - \lambda\frac{\theta_O}{\Omega_O}\right) \tag{5.5}$$

$$S_{O_2} = S_{O_2,i}\left(0.78 - 7.4 \cdot 10^{-4} \cdot T\right)\left(1 - \frac{\theta_{CO}}{\Omega_{CO}} - \frac{\theta_O}{\Omega_O}\right) \tag{5.6}$$

For all rates an Arrhenius type temperature dependence was assumed:

$$k = k_i \exp\left(\frac{E_{act}}{kT}\right) \tag{5.7}$$

For the desorption rate of CO a coverage dependence of the activation energy was introduced,

$$E_{des} = E_{des,i} \exp\left(1 - \frac{\theta_{CO}}{w\Omega_{CO}}\right) \tag{5.8}$$

with *w* as a weighting factor. An increase of this value results in an increase of the CO poisoning effect on the reaction rates. However, a value of 10 has been shown in the past to be suitable for small nanoparticles, since the effect of CO poisoning has been shown to be less pronounced for small particles.[122]

The oxygen desorption was neglected in the calculations, because oxygen adsorbs dissociatively on palladium and exhibits a high heat of adsorption. Desorption takes only place if molecular oxygen is reformed, which occurs usually at temperatures above 800 K.

The coupled differential equations were solved numerically using an embedded Runge-Kutta Prince-Dormand algorithm. Adaptive step control was used to define the latter maintaining a local error of less than 1 x 10^{-6}. The numerical routines were provided by the GNU scientific library (GSL).[123] The values that have been used for the calculations are presented in table 5.1. Furthermore, the references of the different publications used are given.

Table 5.1 Values used for the mole fraction dependent reaction rate simulations.

Parameter	Value	Details
F_{total} / s^{-1}	$1 \cdot 10^{15}$	Experimental value[120]
$k_{L,i}$ / s^{-1}	$1 \cdot 10^{7.9}$	[122]
$k_{CO,i}$ / s^{-1}	$1 \cdot 10^{14}$	[122]
$E_{L,i}$ / $kJ \cdot mol^{-1}$	56	*Described in the text*
$E_{des,i}$ / $kJ \cdot mol^{-1}$	127	*Described in the text*
Ω_{CO}	0.5	[62]
Ω_{O}	0.25	[62]
$S_{CO,i}$	0.96	[124]
$S_{O,i}$	0.78	[124]
λ	0.3	[122]
N /(cluster $\cdot cm^{-1} \cdot s^{-1}$)	$2.2 \cdot 10^{15}$	[120]
$E_{ads}^{MgO} - E_{des}^{MgO}$ /($kJ \cdot mol^{-1}$)	0.25	[125]
Ω_{CO}^{MgO}	0.5	[121]
$r_{cluster}$ / Å	3.235	Pd_{13}
N_S / cm^{-1}	$1.06 \cdot 10^{13}$	0.47 % ML Pd_{13}
α	0.5	[125]

As mentioned before, the first simulations were performed to reproduce the mole fraction and temperature dependency of the CO oxidation reaction rates for a single crystals and/or large facetted nanoparticles of high surface density. The results for the turnover frequency and the reaction probability are shown in Figure 5.3.

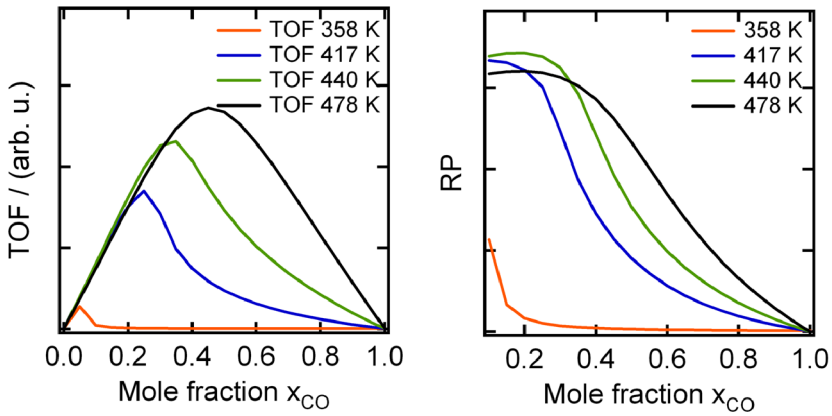

Figure 5.3 Mole fraction dependent *TOFs* (left) and *RPs* (right) obtained for a single crystal based model at different temperatures. Different colors are used for the four temperatures.[121]

The *TOFs* are rising with increasing temperatures, while the maximum is shifted to higher mole fraction values. For the highest temperature the maximum occurs at a mole fraction of 0.5.

In contrast to the *TOFs*, the *RPs* do not increase continuously. The maximum value obtained for 478 K is less than the one determined for 440 K. As seen before for the simulated *TOFs*, the *RP* maxima are also shifted to higher mole fraction values for increasing temperatures. The model catalyst investigated consists of 0.47 % ML of size-selected Pd_{13} clusters deposited on MgO. Thus, the catalyst is highly dispersed and support effects originating from the reverse spill-over of the reactants has to be taken into account.

Since the non-reactive reverse spill-over model proposed by Henry *et al.* had been successfully applied to small palladium clusters, it was decided to include this model into the micro kinetic simulations. The set of differential equations chosen for the single crystal or large nanoparticle calculations were extended as followed:

$$r_{CO} = \alpha_G \eta_{CO} - k_{des}\theta_{CO} - k_L \theta_{CO}\theta_O \tag{5.9}$$

$$r_O = 2\eta_{O_2} - k_L \theta_{CO}\theta_O \tag{5.10}$$

$$r_{CO_2} = k_L \theta_{CO}\theta_O \tag{5.11}$$

Additionally, a global sticking coefficient α_G that corrects the CO flux reaching the clusters is integrated in such a way that the flux based on the non-reactive reverse spill-

over is taken into account. Furthermore, the model of Henry was improved in order to take lateral interactions between the CO molecules on the support into account. In order to do so, the diffusion length is corrected, which has been defined before:

$$X_s = \sqrt{D\tau} = a \cdot \exp\left[\left(E_{ads} - E_{diff}\right)/2RT\right] \tag{5.12}$$

To include the coverage dependency, the adsorption energy E_{ads} and the diffusion energy E_{diff} are modified:

$$E_{ads} - E_{diff} = \Delta E\left(1 - \frac{\theta_{CO}^{MgO}}{\Omega_{CO}^{MgO}}\right) \tag{5.13}$$

This allows the determination of the global sticking coefficient α_G so that the differential equation can be corrected for CO spill-over (a detailed formulation of the following equation is given in chapter 2.1.4):

$$\alpha_G = \pi N_S\left[2\alpha R X_S P(R/X_S, L/X_S) + R^2\right] \tag{5.14}$$

Furthermore, the activation energy $E_{L,i}$ of the reaction was lowered by 4 kJ/mole and the activation energy for CO desorption $E_{des,i}$ by 9 kJ/mole. These changes take into account that most effects observed for single crystals are shifted to lower temperatures for small metal clusters, as seen for the CO adsorption strength in the previous chapter. The choice was arbitrary, but chosen in a way to achieve a good accordance of the simulations with the experimental temperature dependencies. It should be mentioned that O_2 spill-over has been neglected due to the low binding energy of oxygen on MgO in comparison to CO (see chapter 2).

The results of the simulation are presented in Figure 5.4.

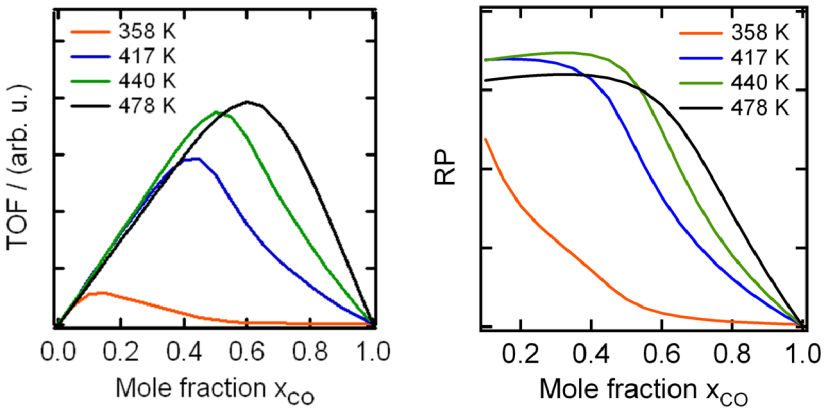

Figure 5.4 Mole fraction dependent *TOFs* (left) and *RPs* (right) obtained for a supported cluster based model at different temperatures. Different colors are used for the four temperatures.[121]

It can be seen that increasing temperatures lead to increasing *TOFs* in the second model, while the maximum is shifted to higher mole fraction values. For the highest temperature the maximum occurs at a mole fraction of 0.6.

The *RP* maxima are shifted to higher mole fraction values for increasing temperatures. However, the *RPs* do not increase continuously as seen for the *TOFs*. The maximum value obtained for 478 K is less than the one elucidated for 440 K.

5.2 Discussion

The discussion is spilt into three sections. First, the experimental results and the single crystal model are discussed and compared. Then the two models are compared with each other and finally the second model simulation is discussed with respect to the experimental results.

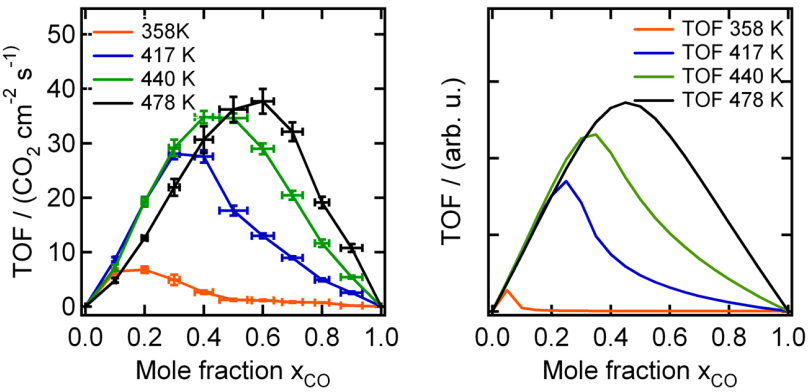

Figure 5.5 Comparison of the experimental *TOFs* (left) and the single crystal model (right). The graphs are normalized to the maximum experimental value at 478 K.

Comparing the experimental results with the single crystal simulation shows that the calculations seem to reflect the general trends observed for small metal clusters quite well. For increasing temperatures the maximum of the *TOF* shifts to higher values with respect to the mole fraction. Furthermore, the absolute values of the *TOF* maxima increase with increasing temperatures for both experiments and simulations. But the position of the *TOF* maximum cannot be reflected correctly in the model. A detailed look at Figure 5.5 shows that the maxima of the model are shifted to lower mole fraction values compared to the experiments.

The two plotted graphs are normalized to the experiment at the highest temperature (478 K) to enable a better comparison of the different temperature dependencies with respect to each other. This illustrates that the maxima of the single crystal calculations are shifted to lower *TOF* values for a given temperature in contrast to the experiments. Furthermore, the reactivity measured for supported cluster is under-estimated in the single crystal calculations at low temperatures (358 K).

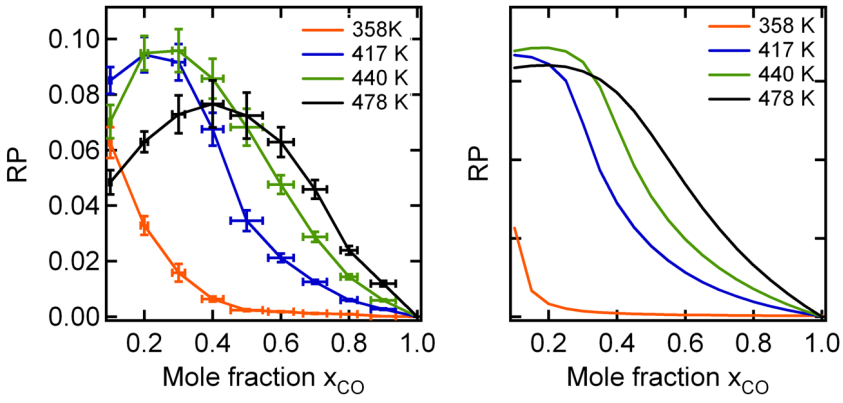

Figure 5.6 Comparison of the experimental *RPs* (left) and the single crystal model (right). The two graphs are normalized to the maximum values at 440 K.[121]

The *RBs* are normalized to the maximum value obtained in the experiment at 440 K. It can be seen that the general trends are again reproduced quite well. The maximum *RP* is shifted to higher mole fraction values for increasing temperatures and the order of the different measurements is reflected correctly.

As seen before for the *TOF* simulations, the *RPs* are under-determined at low temperatures (358 K), as well. However, for the other temperatures (417 K, 440 K, 478 K) the simulated

RPs are too high at small mole fraction values and the maxima of the different isothermal *RP* curves are shifted to lower mole fraction values in the model calculation. In the following the two different model calculations will be discussed and compared.

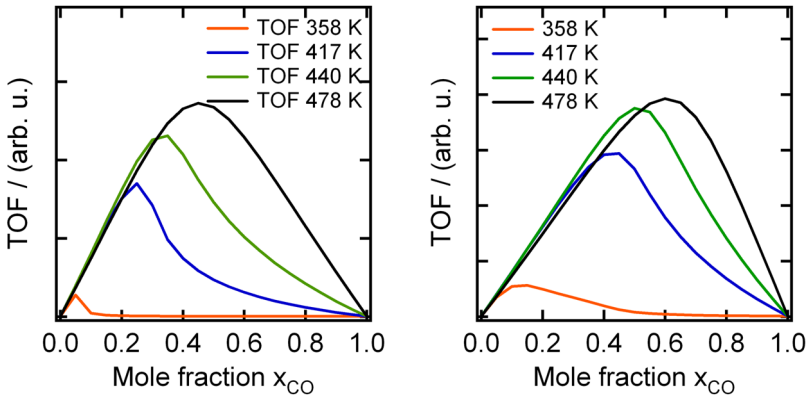

Figure 5.7 Comparison of the *TOFs* simulated for a single crystal model (left) and a supported cluster model (right). The graphs are normalized to the maximum of the experimental data at 478 K.[121]

The general *TOF* trends of the two simulations are in good agreement (see Figure 5.7). The *TOF* maximum is shifted to higher mole fraction values for increasing temperatures. Furthermore, the order of the curves does not vary upon including the non-reactive reverse spill-over model.

A detailed look at the different isothermal curves shows that the *TOF* maximum of the model including the reverse spill-over is shifted slightly to higher mole fraction values. For a better comparison, both graphs are normalized to the maxima of the two curves at 478 K (black). If one compares the black curves for each model with their corresponding simulations at 440, 417 and 358 K, one sees that the values for the model including the reverse spill-over exhibit higher *TOFs* with respect to the *TOFs* at 478 K for each model separately.

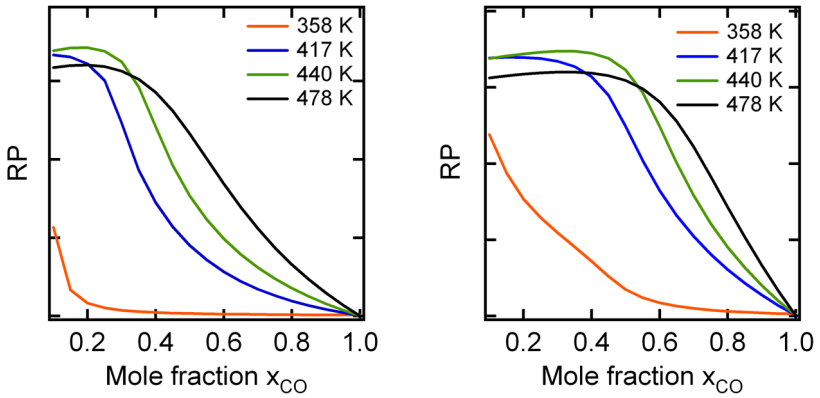

Figure 5.8 Comparison of the *RPs* simulated for a single crystal model (left) and a supported cluster model. The two graphs are normalized to the maximum value at 440 K.[121]

Figure 5.8 shows that the same trends are followed for the reaction probabilities *RPs* in both models. They rise with increasing temperatures up to 440 K and decrease at 478 K. The maxima are shifted to higher mole fraction values for increasing temperatures in both simulations. However, this shift is more pronounced for the simulation including the reverse spill-over model. Another difference, which can be identified, is that the *RPs* in the model without reverse spill-over is extremely limited at low mole fraction values. In the simulation with reverse spill-over included, however, the *RPs* are spread over a broader mole fraction range.

Finally, the results of the second simulation will be compared with the experimental results gained for Pd_{13} clusters on MgO.

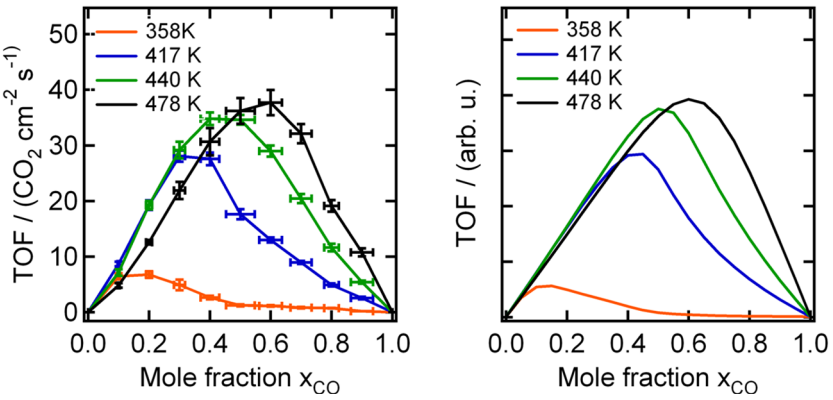

Figure 5.9 Comparison of the experimental *TOFs* (left) and simulated for a supported cluster model (right). The graphs are normalized to the maximum values at 478 K, respetively.[121]

It can be seen in Figure 5.9 that the model is in good accordance with the experimental results and the general trends are reflected very well. The *TOF* maximum of each isothermal curve seems to fit to those of the experiment, which was not the case for the simulations without reverse spill-over. Another interesting point to be mentioned is that the measurements performed at 358 K have been underestimated in the first simulation, whereas they are reproduced correctly in the simulation with reverse spill-over.

Thus, it can be stated that the integration of the non-reactive reverse spill-over model, has led to an improvement of the simulation. The experimental *TOFs* and their tendencies are reproduced better than for the single crystal or large facetted, high density nanocrystal model.

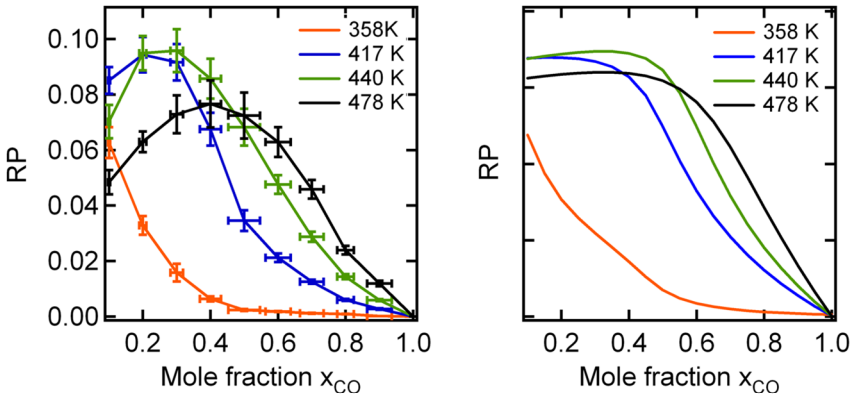

Figure 5.10 Comparison of the experimental *RPs* (left) and simulated for a supported cluster model (right). The graphs are normalized to the maximum values at 440 K.[121]

The shift of the RP maxima to higher mole fraction values leads to a better agreement as the model without reverse spill-over (see Figure 5.10). A great improvement is seen for the *RP* isothermal curve at 358 K. Before including the reverse spill-over, the *RP* at this temperature was under-estimated. A comparison of the experimental results with those obtained from the simulations shows that the curve shape can be well-reproduced by integrating the model of non-reactive reverse spill-over.

However, the experimental results at higher temperatures cannot be reflected as well as the results at 358 K in the range of small mole fractions. Nevertheless, the position of the *RP* maxima are shifted to higher mole fraction values leading to an improvement for the simulated *RPs* of the model for small metal cluster *RPs*.

5.3 Conclusion

Mole fraction and temperature dependent micro kinetic simulations have been performed for a single crystal or large facetted nanoparticle (of high density) like model. A comparison with experimental results obtained for Pd_{13} shows that the general trends could be reflected quite well. However, the positions of the *TOF* and *RP* maxima could not be simulated correctly and the low temperature regime was under-estimated.

In a second step the activation barrier and the CO desorption barrier were lowered and the non-reactive reverse spill-over model developed by Henry *et al.* was implemented. For the turnover frequencies the integration of the model led to great improvements. The position of the maxima can be simulated correctly. Furthermore, the low temperature regime, which had been under-estimated in the first model, is well-reflected in the model including reverse spill-over.

Although the simulations and the experimental *TOFs* are nearly perfect, the same level of accordance can not be achieved for the *RBs*. Nevertheless, the implementation shows some improvements, especially for the lowest temperature (358 K), where the mole fraction dependency is well-described in this regime in contrast to the first model. Furthermore, a shift of the *RP* maximum to higher mole fraction values for increasing temperatures is achieved, agrees better to the experimental results than the first model.

6 Adsorption studies of organic molecules on MgO films

Within the scope of this work a MIES/UPS source has been installed and modified. The aim of this project is to apply these two surface sensitive spectroscopic methods to probe the electronic structure of small metal clusters deposited onto MgO films and to relate the findings to the chemical and catalytic properties of clusters. The modifications of the source allow performing of MIES/UPS measurements at the existing setup. Before cluster experiments will be performed, organic molecules adsorbed on MgO films have been studied in order to determine their properties and potential of the two methods for future applications.

6.1 Results

6.1.1 MgO characterization

6.1.1.1 Auger electron spectroscopy (AES)

The clean Mo(100) single crystal as well as the MgO film grown onto the single crystal are usually characterized by means of AES in order to probe the presence of impurities. Figure 6.1 shows a typical AES spectra of the Mo(100) crystal used in the presented work, after e−gun cleaning (blue line) and of a MgO film grown on the Mo(100) single crystal (green line).

The single crystal of Mo(100) shows the characteristic peak structure at 185 eV appearing from the Mo (MNN) Auger process and a minor feature at 500 eV, indicating the presence of small oxygen impurities. A complete crystal cleaning to remove oxygen impurities was not achieved, since the crystal is used to grow oxides films on the surface, acting as a support for the clusters. The values for both, the MNN transition of molybdenum as well as the oxygen feature are in good agreement with literature values.[126, 127]

In the spectrum of the MgO film grown on Mo(100) two main features can be observed, originating from oxygen (503 eV, KLL) and magnesium (1178 eV, KLL).

However, no contributions arising from impurities or contaminations are present. The values obtained as well as the peak intensities with respect to each other agree well with the aforementioned literature.

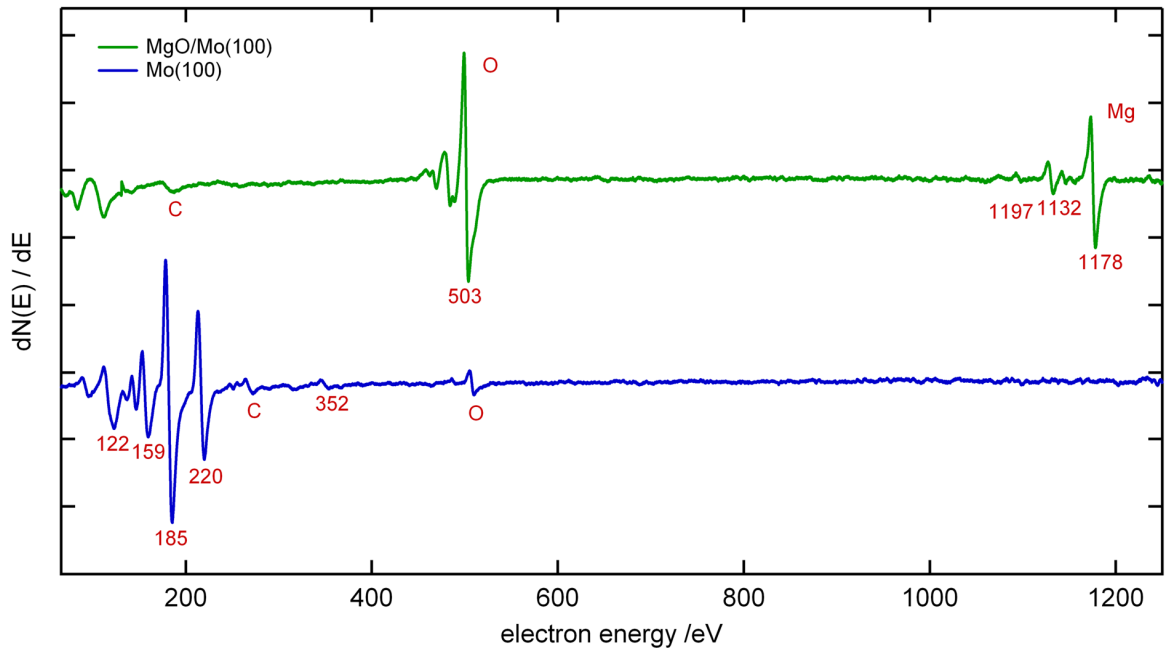

Figure 6.1 Typical Auger spectra recorded for a clean Mo(100) single crystal (bottom) and a MgO film grown on a Mo(100) single crystal (top). The experiments were performed using an excitation energy of 3kV.

6.1.1.2 MIES/UPS

Typical MIES and UPS spectra of MgO/Mo(100) taken at 100 K are presented at the left of Figure 6.2. The right part shows spectra of the same surface probed by means of MIES/UPS from the Kempter group at the TU Clausthal-Zellerfeld as a function of D_2O exposure.[128] The uppermost spectrum at 0 L presents the clean MgO/Mo(100) surface, which can be compared to the spectra recorded in the nanocatalysis laboratory.

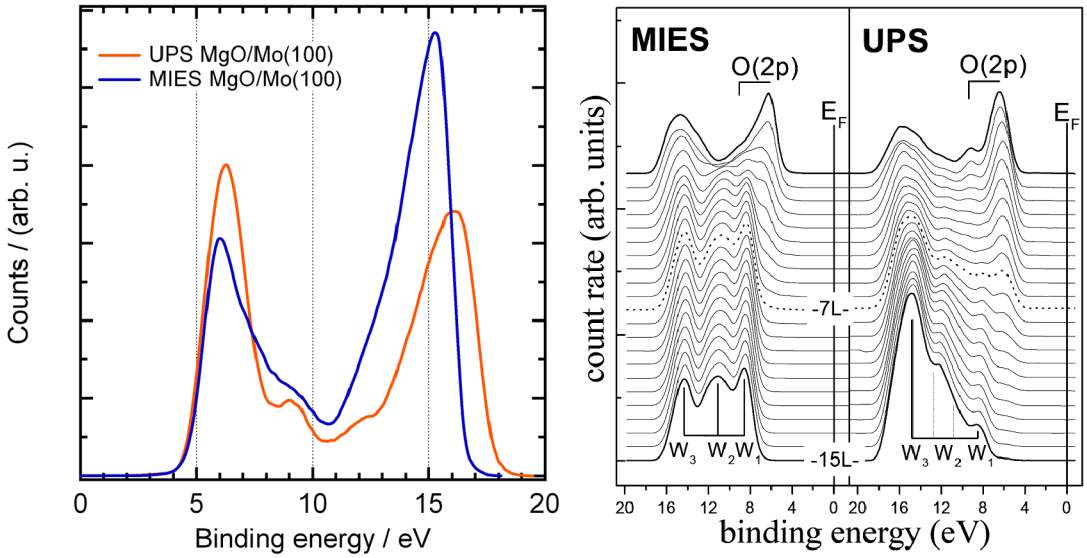

Figure 6.2 UPS and MIES spectra recorded in the nanocatalyis laboratory (left) and at the TU Clausthal-Zellerfeld (right).[83, 128]

At low binding energies the valence structures of the materials are visible. Electrons at high binding energies should not be discussed, as they originate from inelastic scattering processes (secondary electrons). Thus, the kinetic energy of these electrons is lowered by an indeterminable quantity. It has been shown in the past that the intensity of secondary electrons increases with increasing photon and metastable intensities. Therefore, optimum working conditions must be tuned for the source in such a way that the electron yield in the valence regime is high, while the secondary electron yield should be low.

The shape of the UPS spectra consists predominantly of the O(2p) peak structure, with two well pronounced peaks with maxima at 6.3 and 9.1 eV. The two peak structure originates from the two types of p-orbitals, present in MgO.[129] One oriented parallel and the other one oriented perpendicular to the surface plane. Both are ionized by the ultraviolet radiation and thus, become detectable using UPS.

The MIES spectra acquired for the MgO film are mainly the image of the MgO(100) (surface DOS) originating from the AD process (see chapter 2.2.2.3). Due to the insulating character of the clean MgO surface, no intensity between the Fermi edge and the VBM at 3.8 eV appears.

As no occupied states exist in resonance with the He 2s electron, the spectra are pure AD spectra and thus allow comparison between MIES and UPS once the difference in the excitation energy has been corrected (1.4 eV). It should be mentioned that different selection rules hold for either photoionization or AD and hence, the spectra do not contain the same information. AD is particularly sensitive to those orbitals that are oriented to the vacuum side, whereas UV photons probe the average over 2 to 3 adlayers (JDOS). All spectra presented in this work have been measured with MgO as a substrate; therefore no contributions from AC processes must be taken into consideration.

The structure of the MIES spectrum reflects the SDOS of the substrate due to the ionization of MgO valence band (VB) states. These states have mainly O(2p) character. In contrast to the above described two peak structure in the case of UPS only a single peak with a maximum at 6 eV is presented in the MIES spectrum. This is due to the fact that MIES ionizes one type of the aforementioned two types of p orbitals, preferably the one oriented perpendicular to the surface. Furthermore, the spectra show no indication for occupied point defect states (F-centers) in the lower part of the band gap.

Both spectra are in very good agreement with the literature with respect to the observed peaks and their binding energies. Furthermore, the obtained structures also agree well with calculations performed on those systems.[130, 131]

6.1.2 Adsorption properties of benzene on MgO

Since it was shown that the spectra gained for the system MgO/Mo(100) can be reproduced and that they agree well with spectra known from the literature, the adsorption of benzene on MgO/Mo(100) was studied as a next step, in order to test their reproducibility and to compare with literature spectra.

The MIES/UPS spectra of clean MgO/Mo(100) and the same surface covered with 3 L of benzene (saturated surface) are presented in Figure 6.3 and Figure 6.4. The features of the substrate spectra have been discussed in the previous section and are in good agreement. However, the second O(2p) peak in the UPS is only weakly pronounced, because the photon and metastable intensities were too high in these experiments. Thus, the spectra are

dominated by secondary electrons, which are superimposed over the valence structure. This is an example that illustrates the importance of optimizing the MIES/UPS source towards optimum conditions for gaining meaningful spectra.

6.1.2.1 UPS spectra of benzene adsorbed on MgO/Mo(100)

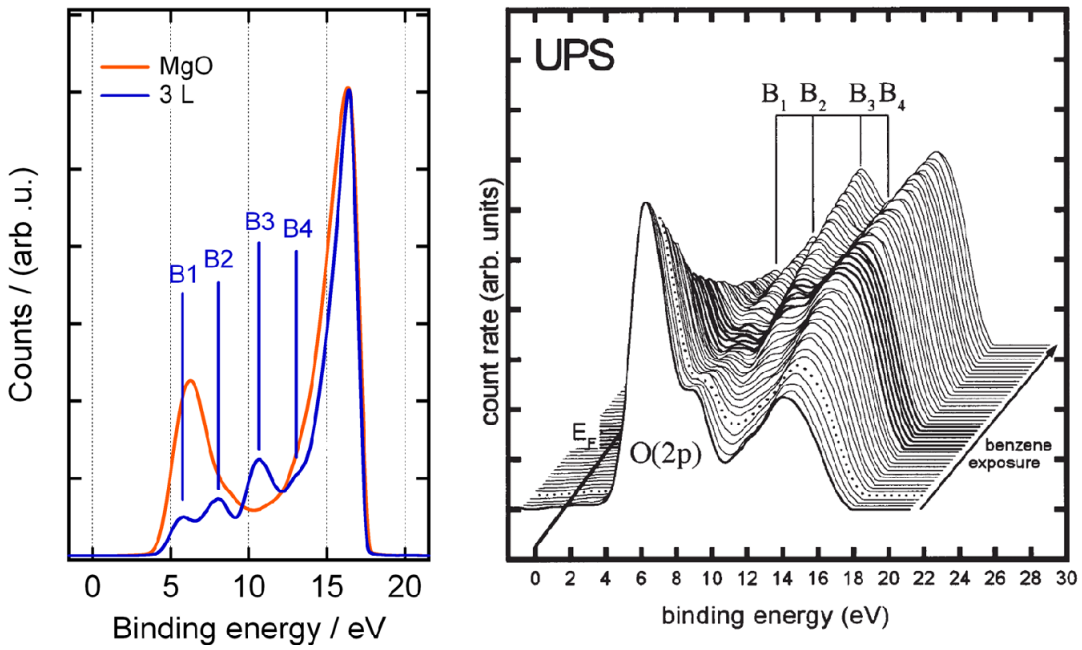

Figure 6.3 UPS spectra of benzene adsorbed on MgO recorded in the nanocatalysis laboratory (left) and at the TU Clausthal-Zellerfeld (right).[83, 132]

The UPS spectrum presented in Figure 6.3 exhibits four distinct peaks that are marked with blue vertical lines, at 5.5 eV (B1), 8 eV (B2), 10.5 eV (B3), and 13.5 eV (B4). The peaks are in agreement with those observed in literature spectrum (see right side of Figure 6.3). The lower intensity of electrons in the valence regime for the measurement performed in the nanocatalysis laboratory is due high UPS intensity of source, as mentioned previously.

6.1.2.2 MIES spectra of benzene adsorbed on MgO/Mo(100)

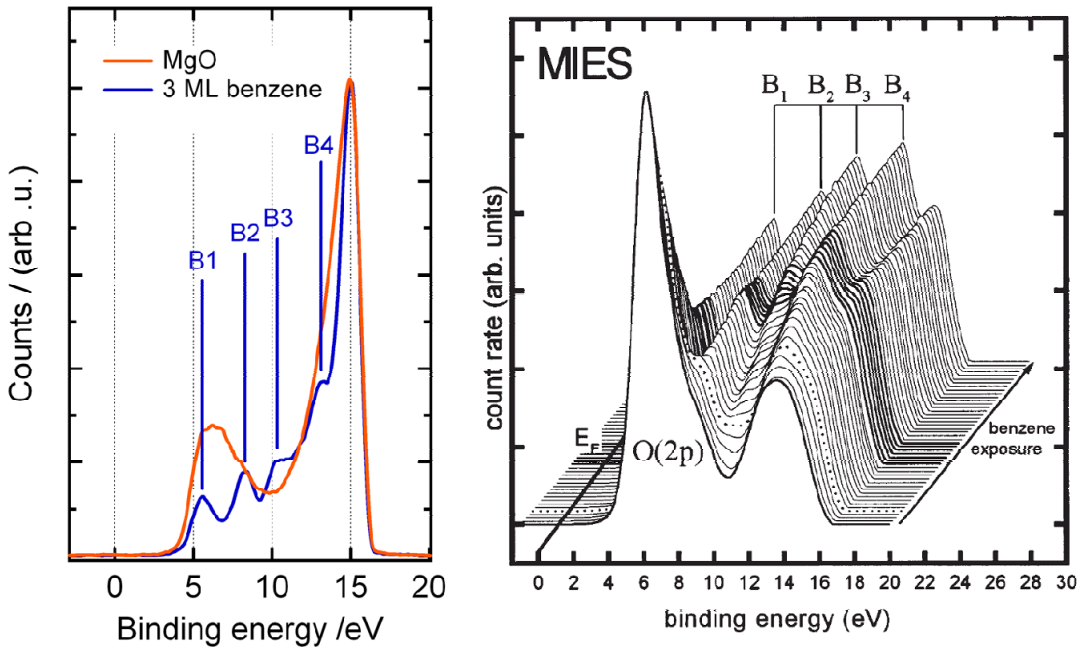

Figure 6.4 MIES spectra of benzene adsorbed on MgO recorded in the nanocatalysis laboratory (left) and at the TU Clausthal-Zellerfeld (right).[83, 132]

In the MIES spectra four distinct peaks, are seen; the features appear at the following binding energies: 5.5 eV (B1), 8 eV (B2), 10.2 eV (B3), and 13.5 eV (B4). A comparison of the spectra with those obtained from the literature shows that the peak positions are correct. The lower intensity of electrons in the valence regime for the measurement performed in the nanocatalysis laboratory is again due to a very high metastable intensity of source during the experiments.

In conclusion, it can be stated that the system MgO/Mo(100) has been characterized successfully by means of MIES/UPS and that the results agree with those obtained from the literature. Furthermore, a study, previously performed in Clausthal-Zellerfeld, of benzene adsorbed on MgO/Mo(100) was reproduced, proving the successful implementation of the MIES/UPS source in the nanocatalysis setup.[132]

6.1.3 Adsorption properties of cyclohexene on MgO

The adsorption properties of cyclohexene as an example for hydrocarbons were probed on MgO. In order to analyze the adsorption properties and the electronic structure of cyclohexene on MgO two series of MIES/UPS spectra were recorded. One series with low coverages in 0.01 ML steps (from 0.0 to 0.15 ML) and a second series with higher coverages in 0.1 ML steps (from 0.0 to 1.0 ML). Additionally, TPD experiments of different surface coverages of cyclohexene were performed in order to elucidate the adsorption strength of cyclohexene on MgO/Mo(100).

6.1.3.1 TPD studies

TPD spectra of different cyclohexene (m/e = 82) coverages adsorbed on MgO/Mo(100) were recorded with a temperature rate of 1 K / s in between 100 K and 400 K. It should be mentioned that the coverage value is related to CO adsorbed on MgO.[101] Since CO adsorbs linearly, it can be concluded that the coverage value underestimates the real cyclohexene coverage. The spectra are presented in Figure 6.5.

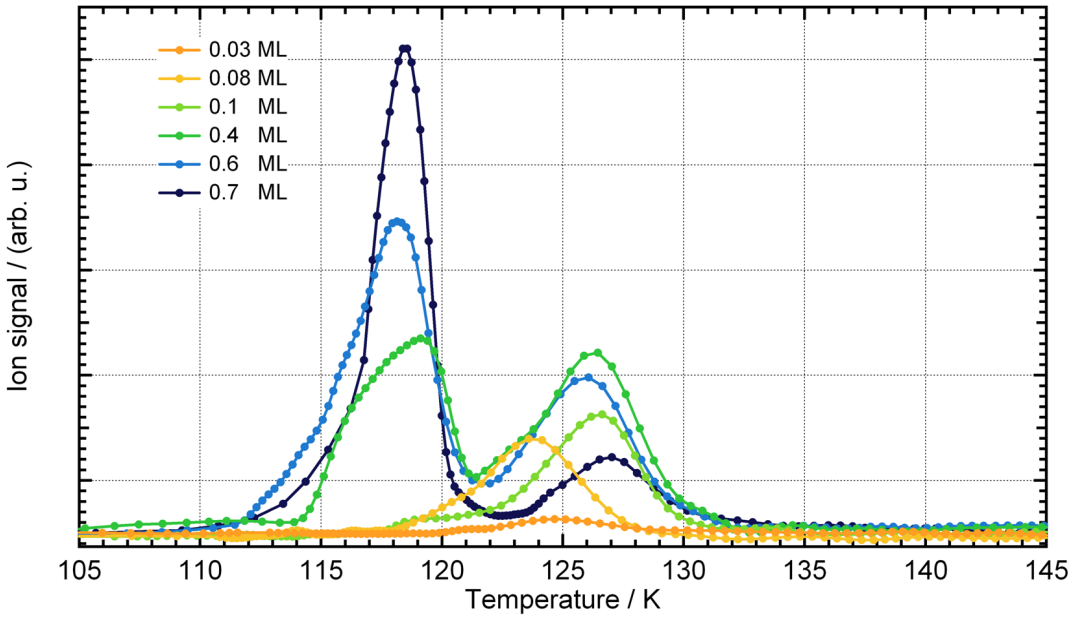

Figure 6.5 TPD spectra of different cyclohexene coverages on MgO.

For the lowest coverages (0.03 ML and 0.08 ML) only one peak is observed at 125 K. At 0.1 ML a shoulder appears at a temperature of 120 K that increases in intensity for higher coverages so that a large band is observed for 0.4 ML, 0.6 ML and 0.7 ML. Furthermore, for 0.7 and 0.6 ML the intensity of the second peak (at 128 K) decreases.

6.1.3.2 UPS spectra of various cyclohexene coverages on MgO/Mo(100)

Figure 6.6 and Figure 6.7 show the obtained UPS spectra for cyclohexene as a function of coverage.

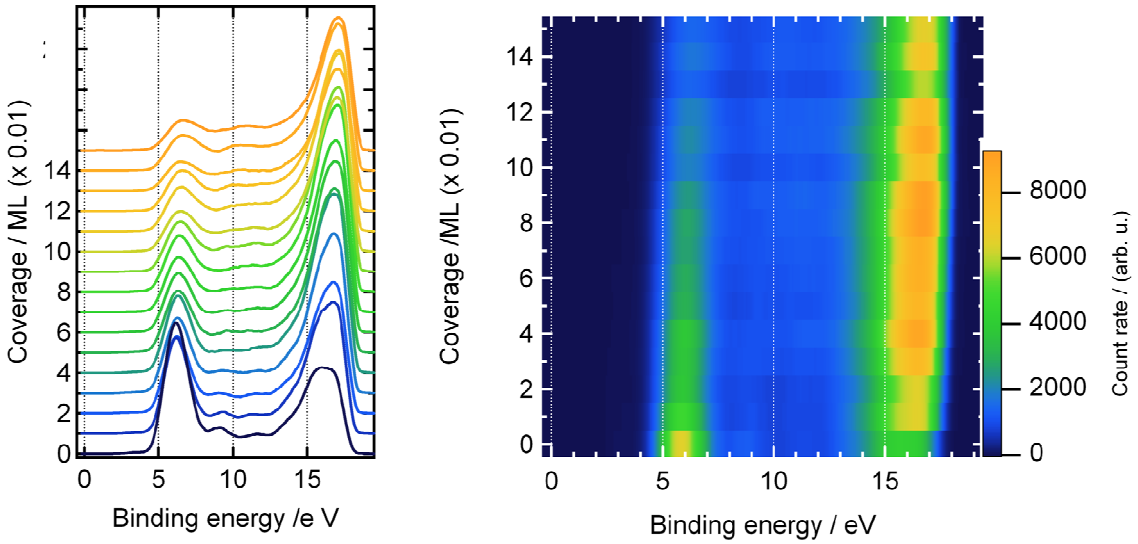

Figure 6.6 UPS spectra of different cyclohexene coverages on MgO (low coverage series). Waterfall plot (left), image plot (right).[83]

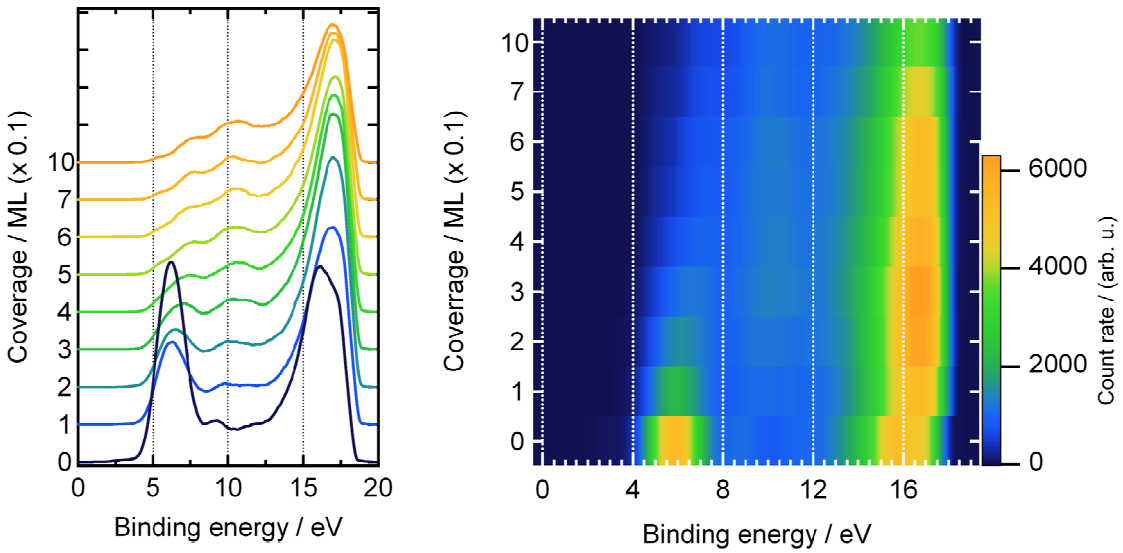

Figure 6.7 UPS spectra of different cyclohexene coverages on MgO (high coverage series). Waterfall plot (left), image plot (right).[83]

From the image plots (right side in Figure 6.6) of the low surface concentration series it can be seen that the spectrum width broadens for increasing cyclohexene coverages. In the image plot of the high coverages this observation is confirmed in the change found for the first dosing step of the clean substrate to a cyclohexene coverage of 0.1 ML. However, more important in this context is the change of the work function that will be shown in the next chapter.

The characteristic features of the surface, the O(2p) two peak structure (6 eV, 8 eV) decrease with increasing coverage. In the low coverage plot one can see that the O(2p) feature at 8 eV vanishes completely at a coverage of 0.8 ML; the band at 6 eV decreases as well and disappears at 0.4 ML. Two new peaks appear in the spectra at 7 eV and 10 eV (also visible in the image plot for high coverages) beginning at 0.5 ML and 0.12 ML, respectively.

The plot with low coverages shows continuous changes in the structure of the spectra. However, only attenuation of the MgO characteristics can be observed.

6.1.3.3 MIES spectra of various cyclohexene coverages on MgO/Mo(100)

The MIES spectra corresponding to the previously presented UPS spectra are shown in Figure 6.8 and Figure 6.9.

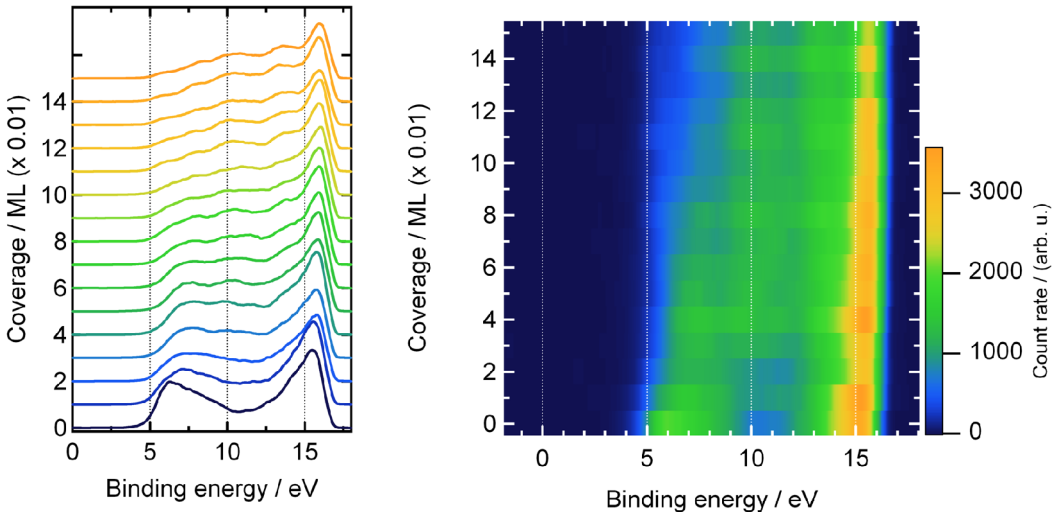

Figure 6.8 MIES spectra of different cyclohexene coverages on MgO (low coverage series). Waterfall plot (left), image plot (right).[83]

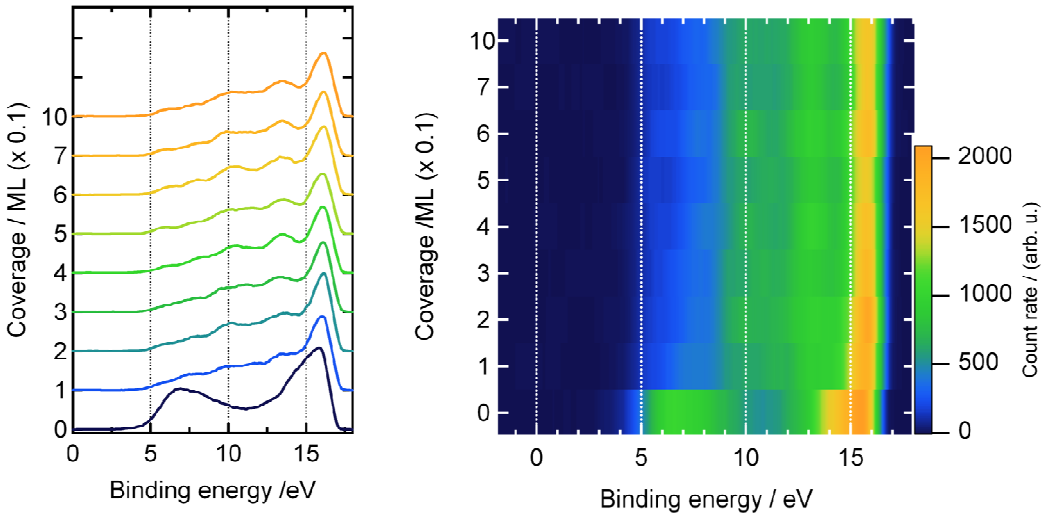

Figure 6.9 MIES spectra of different cyclohexene coverages on MgO (high coverage series). Waterfall plot (left), image plot (right).

The O(2p) peak of the MgO film at around 6 eV vanishes with increasing coverage and is no longer pronounced at coverages greater than 0.12 ML, which is well illustrated in the image plot for low coverages. Two principle features at 10 eV and 13 eV appear at 0.04 ML and 0.09 ML, respectively. Furthermore, two minor characteristics are apparent for

coverages higher then 0.14 ML; a minor peak at 8 eV and a less intense one at 5.5 eV. Above 6 ML no changes in the spectra are seen.

6.1.3.4 Work function changes extracted from MIES/UPS spectra

As aforementioned work function changes were determined for the two series of different surface concentrations (see Figure 6.10). MIES spectra are dominated by Auger Dexcitation (AD) processes allowing the extraction of the work function in the same way as for UPS spectra and the comparison of the values extracted form UPS and MIES spectra.

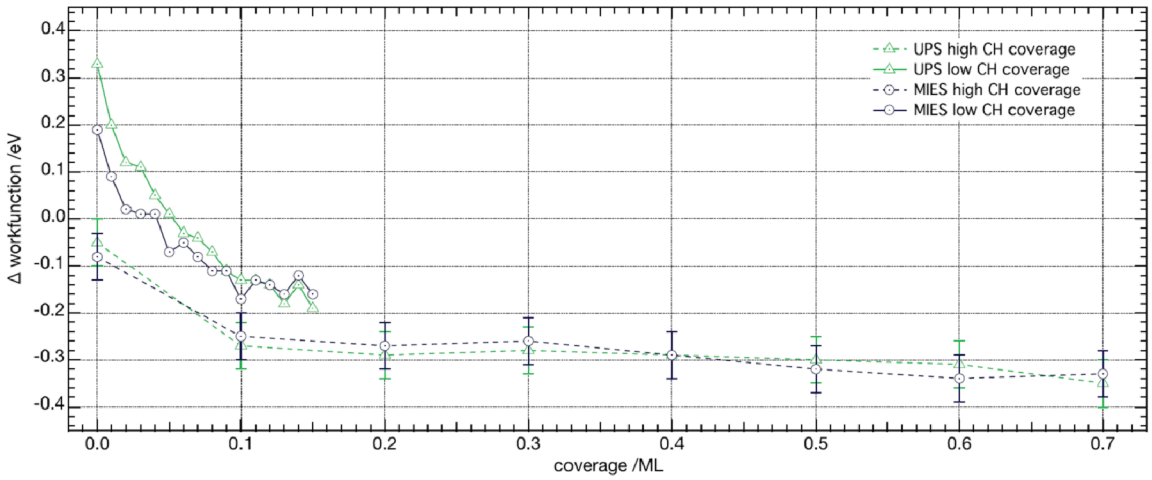

Figure 6.10 Change in the WF for increasing cyclohexene surface concentration.[83]

As absolute work function values can deviate to a large extend, even for the same experimental setup, only the changes of the work function will be discussed in this work.
As it can be seen from Figure 6.10 the work function decreases monotonously for every measurement with increasing cyclohexene coverage.

6.1.4 Adsorption properties of Trichloroethylene (TCE) on MgO

One future project of the Heiz group that is currently under construction will focus on the photochemical conversion of TCE. As a first step of the project the adsorption properties of TCE on MgO was investigated by means of MIES/UPS and TPD. Again, two series of MIES/UPS spectra were recorded: One at low coverages (from 0.00 - 0.15 ML in 0.01 steps) and a second at high coverages (from 0.0 - 1.0 ML in 0.1 ML steps). Additionally, TPD spectra of adsorbed TCE were taken, but only for the high coverages, because for small amounts of TCE the mass spectrometer signal is beyond the detection limit.

6.1.4.1 TPD spectra of various TCE coverages on MgO/Mo(100)

TPD spectra of TCE were recorded with a heating rate of 1 K/s at the mass of TCE (m/e = 132) for different TPD coverages in a temperature range between 100 K and 400 K. The results are presented in the following Figure.

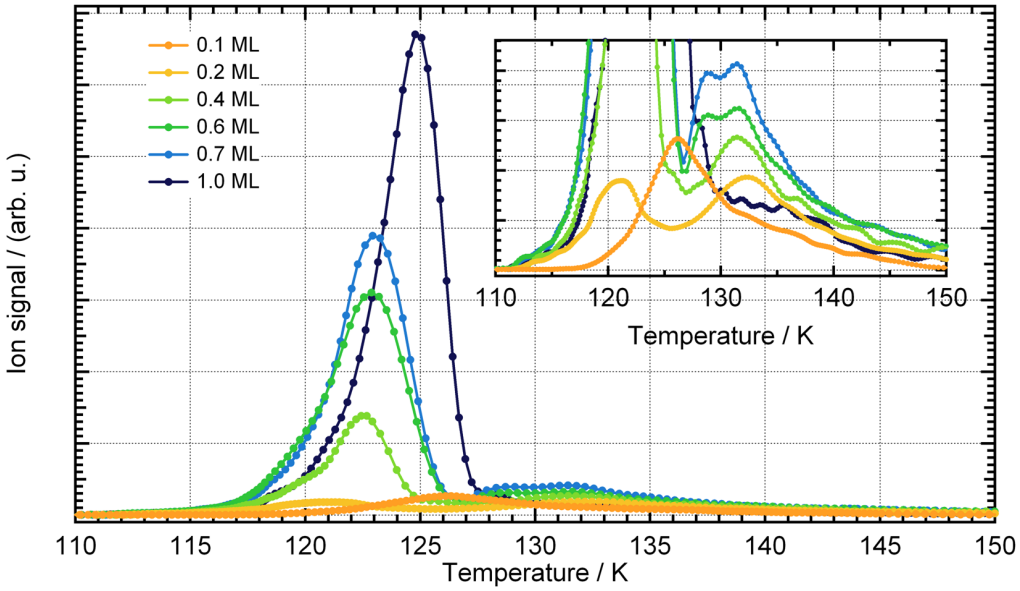

Figure 6.11 TPD spectra of different TCE coverages on MgO.[83]

In contrast to cyclohexene, three different temperatures at which TCE desorbs from the MgO surface can be assigned. For the lowest coverage of 0.1 ML only one peak at 126 K

is observed. An increase in surface concentration leads to a two peak structure for 0.2 ML with a maximum at low temperatures (124 K) and a second at 132 K. Further increase of the coverage up to 0.7 ML does not change the shape of the obtained spectra, however, the maximum of the first peak shifts to higher temperatures (from 121 K (0.2 ML) to 124 K (0.7 ML)), whereas the maximum of the second peak shifts to lower temperatures (from 132 K (0.2 ML) to 130 K (0.7 ML)). The intensity of both peaks increase with rising coverage. However, the increase in the first peak is more pronounced, compared to the one of the second peak. In the spectrum of the highest coverage (1 ML) the second peak is hardly observable and occurs only as a small shoulder of the first desorption peak.

In order to determine the accuracy of molecule dosing, the TPD spectra presented in Figure 6.11 were integrated and the resulting values plotted against the coverage calculated from the backpressure and the dosage time (see Figure 6.12).

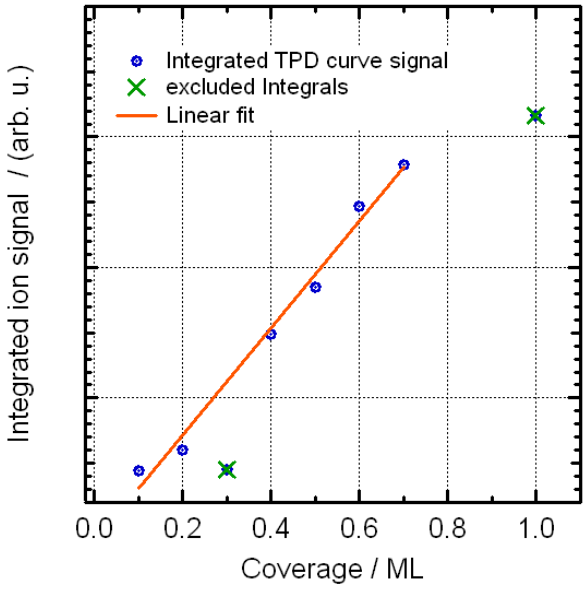

Figure 6.12 Integrated ion signal plotted for different dosages.

If a constant sticking probability is assumed, a linear curve has to be expected. As seen in Figure 6.12 only two measurements do not fit to the linear regression. Due to this reason the results for 0.3 ML are ignored in this work. Although the integral of 1.0 ML does not fit to linear regression, the TPD was not ignored, because it can still be used as a result for a TPD of a higher surface concentration than the ones between 0.1 ML and 0.7 ML.

In conclusion, the results confirm that the usage a molecular beam doser compared to the commonly applied Langmuir dosage procedure, is an improvement.

6.1.4.2 UPS spectra of various TCE coverages on MgO/Mo(100)

The obtained UPS spectra are presented in Figure 6.13 for high and in Figure 6.14 for low coverages.

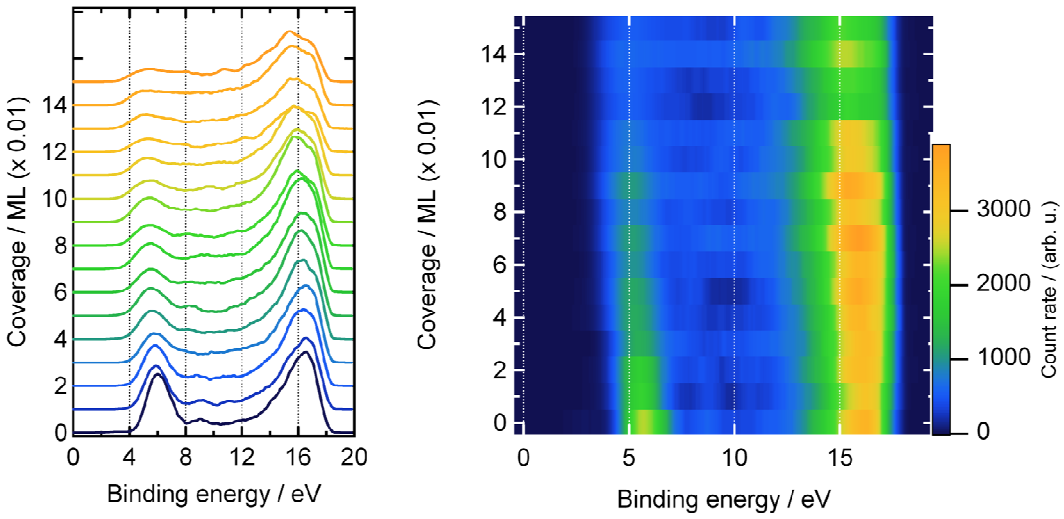

Figure 6.13 UPS spectra of different TCE coverages on MgO (low coverage series). Waterfall plot (left), image plot (right).

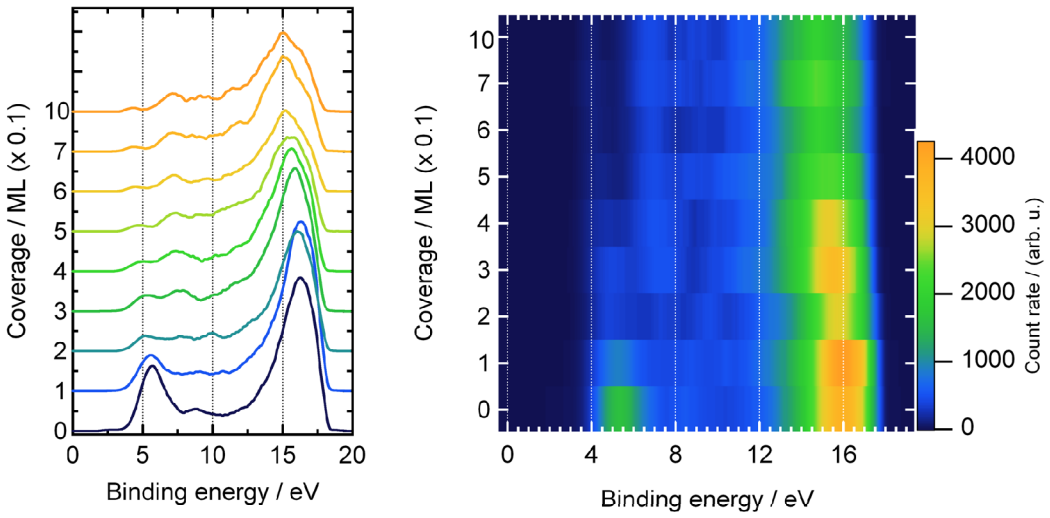

Figure 6.14 UPS spectra of different TCE coverages on MgO (high coverage series). Waterfall plot (left), image plot (right).

The O(2p) peak originating from the MgO surface at 6 eV decreases with increasing TCE surface concentration. At coverages above 0.1 ML the peak vanishes completely.

For higher coverages (from 0.3 ML on), two peaks can be observed close to position where the O(2p) peak was: one with a low intensity at 4.5 eV and a second exhibiting a higher intensity at 7 eV. The peak at 4.5 eV shifts towards lower binding energies down to 4 eV for further increasing coverages. Two more features can be seen at higher coverages: One at 11 eV that starts to appear at coverages above 0.1 ML and a second around 15 to 16 eV which is hardly seen, because it overlaps with the secondary electrons.

From the series at higher TCE loadings it can be concluded that no further change is observed for coverages above 0.3 ML.

6.1.4.3 MIES spectra of various TCE coverages on MgO/Mo(100)

The MIES spectra of the corresponding UPS spectra are presented in the following plots (Figure 6.15 and Figure 6.16).

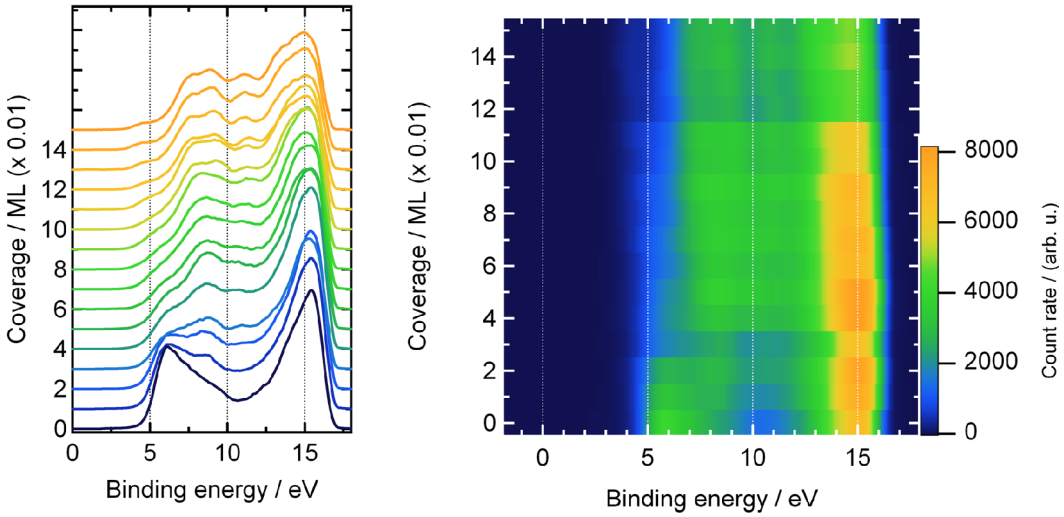

Figure 6.15 MIES spectra of different TCE coverages on MgO (low coverage series). Waterfall plot (left), image plot (right).

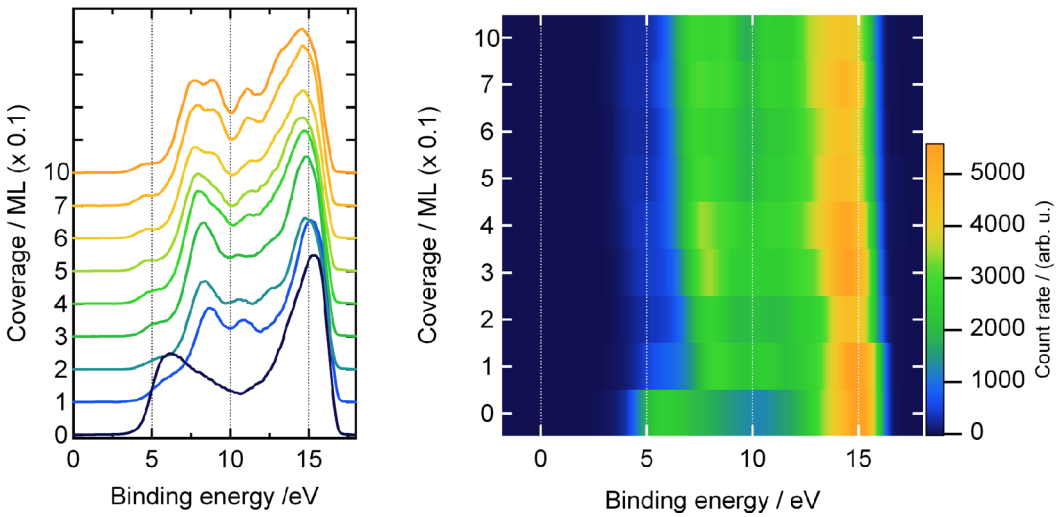

Figure 6.16 MIES spectra of different TCE coverages on MgO (high coverage series). Waterfall plot (left), image plot (right).

The MgO O(2p) peak that occurs at 6 eV disappears at a TCE coverage of 0.04 ML. In the same binding energy region (at 4.5 eV) a small increase in electron density is observed for 0.1 ML.

A feature at a binding energy of 8 eV appears already for the lowest coverage (0.01 ML). This band seems to split into two peaks (7.5 eV and 9 eV) at surface concentrations above 0.1 ML in the low coverage series. Surprisingly, the double peak structure is seen in the high coverage spectra only for surface concentrations above 0.6 ML.

Additionally two more structure changes can be seen in the spectra. From low coverages (0.03 ML, very distinct at 0.1 ML in high coverage plot) a clear visible peak at 10.5 eV appears.

In the high coverage spectra this peak shifts slightly with increasing loading (from 0.4 ML on) to higher binding energies of around 11 eV.

6.1.4.4 Work function changes extracted from MIES/UPS spectra

As for the cyclohexene experiments, the change of the work function with respect to TCE coverage has been determined, too. The results are shown in Figure 6.17.

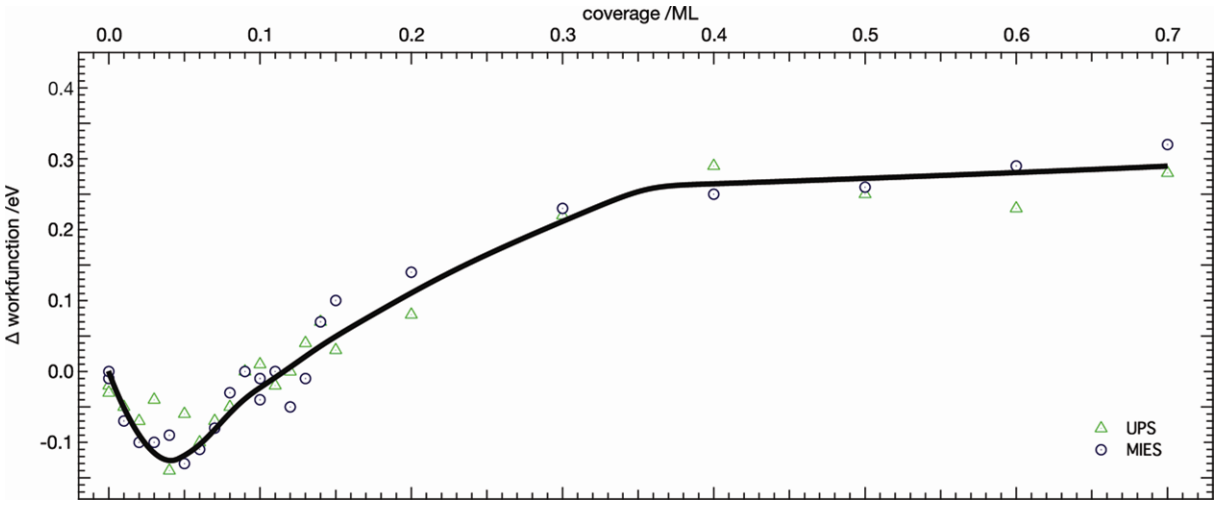

Figure 6.17 WF change for increasing TCE surface concentrations. The black line is a guide to the eye.[83]

Interestingly, the value decreases in the beginning and reaches a minimum around 0.04 ML. Further increasing of the surface concentration leads to an increase of the work function until a saturation level is reached for surface concentrations higher than 0.4 ML.

6.2 Discussion of adsorption studies of organic molecules on MgO/Mo(100)

The adsorption of benzene on MgO/Mo(100) has bee successfully reproduced proving that meaningful MIES/UPS studies can be performed in the nanocatalysis laboratory. The following chapter will focus on the discussion of cyclohexene and TCE adsorption on MgO/Mo(100).

6.2.1 Cyclohexene adsorption on MgO/Mo(100)

From the TPD data the following conclusions can be drawn in order to explain the adsorption mechanism of cyclohexene on MgO/Mo(100).

For low coverages up to 0.1 ML one single adsorption state exists, corresponding to only one type of adsorption, which can be seen in the TPD. Further increase leads to two

desorption peaks at different temperatures (118 K and 126 K) and thus to two distinctive adsorption states.

The state which desorbs at higher temperatures (126 K) is related to a physisorbed state of cyclohexene on the MgO surface, because the desorption temperature is low in comparison to a chemisorbed states that exhibits π–back donation from the metal to the LUMO.[133]

At a certain coverage the lateral interaction between the adsorbed molecules in the physisorbed layer increases, so that a dense layer is formed that avoids further adsorption of cyclohexene. The peak at lower temperatures can be attributed to cyclohexene condensed on the physisorbed layer. Up to 0.4 ML both adsorption states show increasing population which can be derived from an increase in intensity for both peaks in the TPD spectrum. Hence, it is assumed that the physisorbed layer gets compressed at higher coverages by the condensed cyclohexene layers, leading to a higher concentration of the physisorbed state.

The MIES data show that for increasing surface concentration a continuous change of the electronic structure of the surface up to a coverage of 0.6 ML. Above 0.6 ML no changes are observable, leading to the conclusion that the surface is saturated with cyclohexene.

Similar observations are made for the UPS spectra. The spectrum shape does not change as the coverage increases. Thus, in both cases a saturation of the surface with cyclohexene can be concluded.

The work function change shows a monotonous decrease with increasing coverage. The gradual decrease can be explained considering the fact that cyclohexene has a very small permanent dipole moment. Thus, the orientation of the adsorbed molecules does not influence the surface dipole moment. The decrease in the work function is only due to the increasing thickness of the cyclohexene layer, which is non-polar in comparison to the MgO surface. In conclusion, a model for the adsorption of cyclohexene can be proposed as followed:

Up to a coverage of 0.1 ML (defined by the molecular beam doser) cyclohexene physisorbs on the MgO surface (single peak in the TPD). With increasing coverage a second state appears, which is attributed to condensation of cyclohexene on top of the first (physisorbed) layer. Whether an approaching molecule condensates or physisorbs, depends on the amount of energy released by adsorption and the repulsive forces of already physisorbed molecules.

At a certain point (0.4 ML) the surface is saturated with physisorbed molecules and only condensation (also possible in multilayers) occurs. This can be concluded from the increase of the first TPD peak, furthermore the decrease of the second TPD peak (at higher temperatures) suggests that the condensation is much more favourable. Thus, fewer molecules are physisorbed in comparison to lower coverages.
Furthermore, no changes in UPS or MIES can be extracted for coverages higher than 0.4 ML, leading to the conclusion that the surface and the three top layers do not change upon further cyclohexene adsorption.

6.2.2 TCE adsorption on MgO/Mo(100)

As already mentioned above, three different desorption peaks can be distinguished in the TPD spectra. For the lowest coverage at 0.1 ML only one peak is observed, which is assigned to physisorbed TCE on the MgO surface. At 0.2 ML the peak observed for 0.1 ML seems to split into two peaks, due to the increasing coverage. Hence, it is concluded that physisorbed as well as condensated TCE on the physisorbed layer is observed. Interestingly, a clear temperature shift of the stronger bonded state to higher temperatures (from 126 K to 132 K) and thus even stronger bound TCE is recognized.
For increasing coverages it seems that the physisorbed layer becomes higher populated, since the integral of the second peak rises. However, the temperature maximum is shifted to lower temperatures. Therefore, it is concluded that the increasing population of the physisorbed state leads to a weakening of the adsorption strength due to lateral interaction between the physisorbed TCE molecules. Furthermore, at very high surface concentrations (1.0 ML) the physisorption peak shifts to 128 K and it becomes difficult to distinguish it from the condensed layer.
The spectra recorded for various TCE coverages are hard to discuss without any theoretical support. However, the change of the work function is a very useful tool in terms of discussing the adsorption properties. As already seen in Figure 6.17 the value decreases to a minimum at 0.04 ML, reaches the same level as MgO for 0.1 ML, and shows saturation at a coverage of 0.4 ML exhibiting a higher work function than clean MgO. Since the saturation level shows an increase in the work function in comparison to MgO, it can be

concluded that TCE has a higher surface dipole moment than clean MgO. However, the question arises why the work function decreases for low coverages (< 0.1 ML).

It is assumed that at low surface concentrations the TCE molecules lie flat on the surface with their dipole moment perpendicular to the normal vector of the surface. When the physisorbed layer gets further compressed, the dipole moment and hence the molecules start to organize in a way that the dipole moment is shifted more and more parallel to the surface normal vector. This leads to an increase of the work function.

The different aspects which could be gained from TPD as well as UPS and MIES experiments are summarized in Figure 6.18.

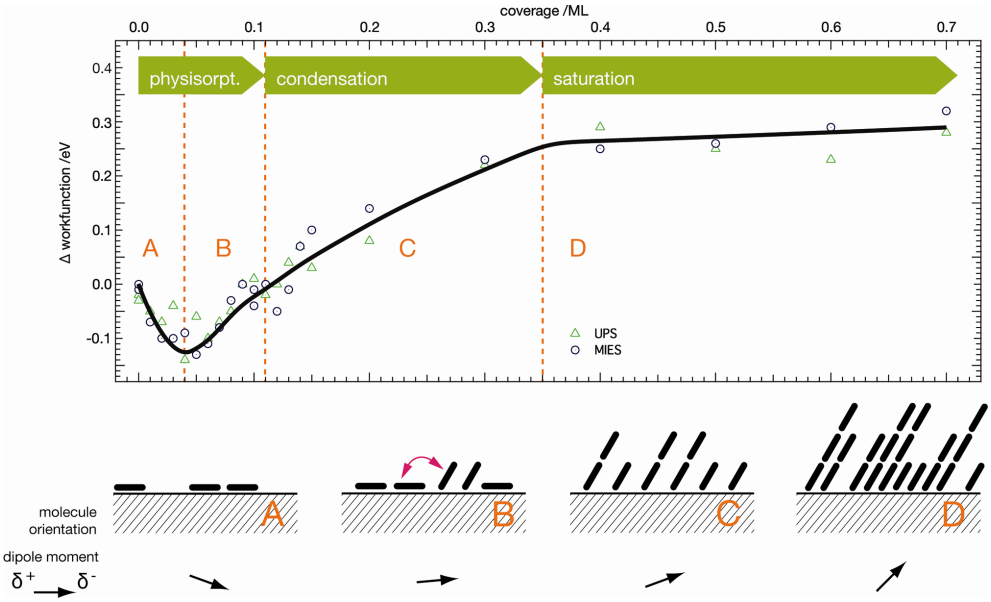

Figure 6.18 Assumed four step adsorption model for TCE on MgO.[83]

The adsorption properties can be divided into four different regions depending on the coverage. For region A it is concluded that only flat lying TCE is present. This agrees with the TPD and UPS/MIES data, since only one state is found for which a work function decrease is observed.

In region B the work function value shows an increase. Hence, it is concluded that the molecules start to rearrange in such a way that the dipole moment is aligned more and more with the surface normal vector.

Region C exhibits two peaks in the TPD and thus it is assumed, that TCE condensation on top of the physisorbed layer occurs at these surface concentrations. Further dosage in

region C leads to an increasing population of both states. Since the molecules in the physisorbed layer are now shifted towards the vacuum side additional free spaces become available. However, they depend on the strength of lateral interaction. This explains the shift in the TPD of the physisorbed peak maximum, because an increase in lateral interaction results in a decrease of adsorption strength.
In region D the increase in physisorbed molecules does not influence the work function anymore, since the adsorbed layers have reached a thickness at which only condensed TCE can be probed in UPS and MIES.
An alternative explanation of the observed results is currently discussed in cooperation with Yuri Suchorski from the TU Wien.

6.3 Conclusions and outlook

The studies of benzene adsorbed on MgO have shown that the spectra published by Kempter *et al.* could be reproduced in the nanocatalysis laboratory, proving the successful implementation of the MIES/UPS source.
The adsorption properties of cyclohexene and trichloroethylene were investigated by means of MIES/UPS and TPD. Whereas the interpretation of cyclohexene is rather straight forward due to its simple electronic functionality, the results of TCE are complicated and challenging to interpret. Based on the experimental results, a four step adsorption model has been proposed to explain the results presented in this work.
Recently, spectra for unselected Pd clusters at various coverages have been measured. The results are presented in a waterfall plot in Figure 6.19.

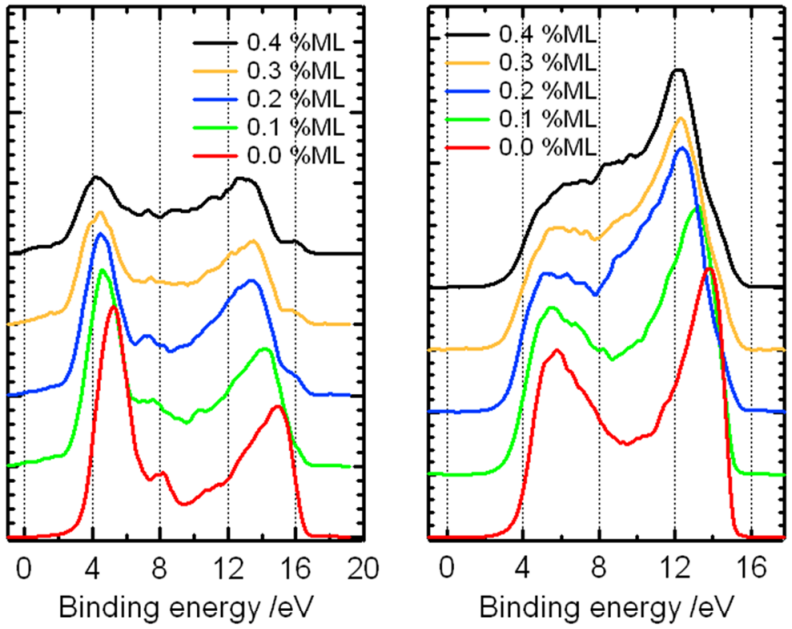

Figure 6.19 Spectra of different unselected Pd cluster coverages (0.0-0.4%ML in steps of 0.1%ML). The UPS spectra are shown on the left side and the MIES on the right side.

An interesting results is seen if the graphs are plotted without an offset (Figure 6.20):

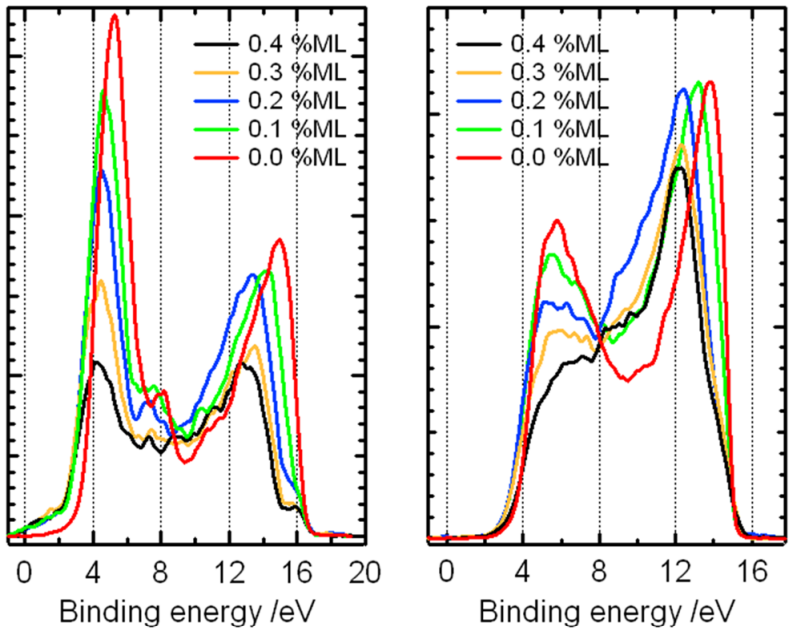

Figure 6.20 Same spectra of different unselected Pd cluster coverages (0.0-0.4%ML in steps of 0.1%ML) as shown in Figure 6.19, but plotted without an offset. UPS spectra are illustrated on the left side and the MIES on the right side.

A look at high binding energies of the UPS spectrum (left side of Figure 6.20) shows an interesting result. Instead of only one cut-off, two cut-offs seem to appear for increasing Pd cluster coverages. The same holds for the MIES spectra (right side of Figure 6.20); however, the effect is more pronounced in the UPS spectra. This observation is in contrast to results obtained for Pd deposited on MgO via metal evaporation, where only one cut-off was observed.[134]

This is only a first interesting result gained via MIES/UPS for deposited clusters, which is not understood at the moment. Further studies are in progress on order to understand this effect.

7 Cluster under ambient conditions

Within the scope of the presented work the developed and constructed transfer system has been applied to deposit clusters, to transfer them to ambient conditions and electrochemical measurements have been performed to test their potential for catalytic studies under ambient and industrial relevant conditions.

7.1.1 Size control

In a first step of this project Transmission Electron Microscopic (TEM) experiments were performed to prove whether clusters can be deposited and transferred. The microscope used is limited to a particle size of 1 nm in diameter; the mass-spectrometer with the higher mass-limit available from EXTREL, is working up to masses of 9000 amu. Since platinum has been used in this project, the highest mass that could be selected was Pt_{46}. Assuming a spherical shaped cluster form the diameter of a Pt_{46} cluster would be around 0.8 nm. Thus, the application of the mass-spectrometer in the mass-selection mode would give clusters that are smaller than the detection limit of the used TEM. In order to deposit clusters that are large enough to be detected, the mass-spectrometer was operated in the ion-optic mode and the size-selection was solely achieved by the settings of the quadrupole bender.

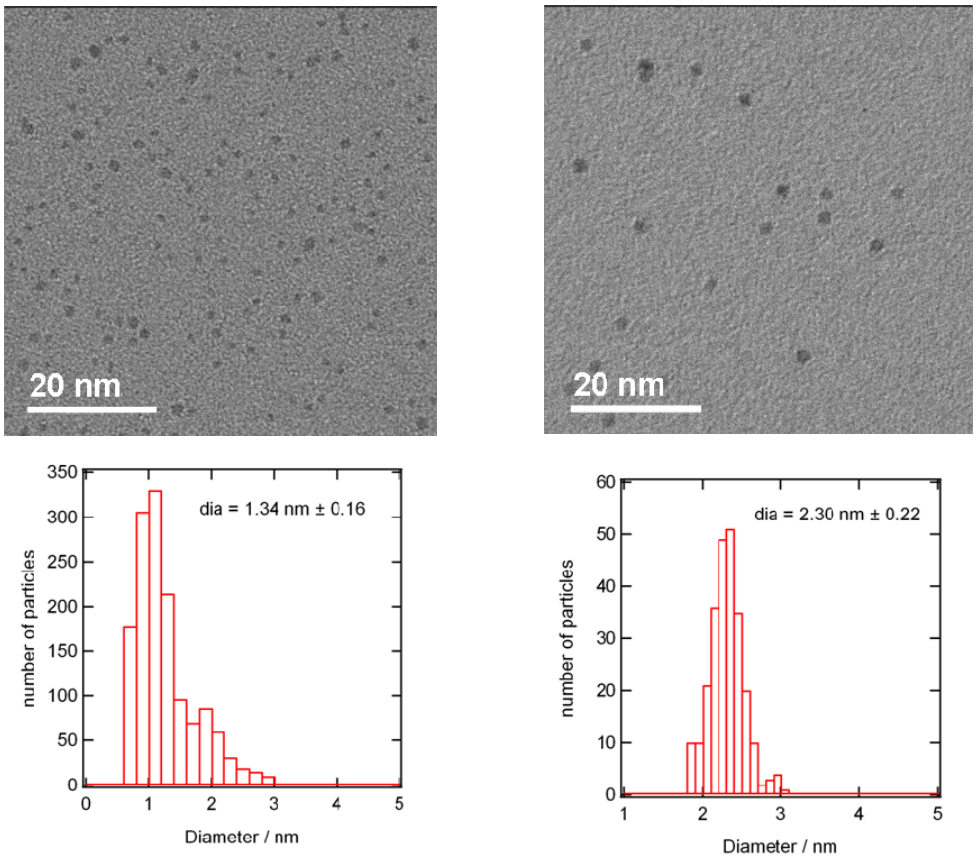

Figure 7.1 TEM images and their corresponding histograms demonstrating the size control by varying the electrostatic settings on the bender system.[135]

In Figure 7.1 typical TEM images are presented for deposited clusters at different bender settings. Comparison of the right and the left picture illustrates that the cluster size can be varied by changing the electrostatic settings of the bender. A statistical analysis of the cluster diameter shows an average diameter of 1.34 nm for the left sample and 2.30 nm for the right. The average error is less than 10 % for both samples.

7.1.2 Coverage control

The great advantage of cluster deposition in comparison to nanoparticles prepared via physical vapor deposition is the independent control of size and the coverage.

In Figure 7.2 TEM images of the same cluster size but different coverages are presented with two different magnifications (A, B and C are images of samples with different

coverages, D, E and F are respectively the same samples taken at higher magnification.) The coverage is varied by changing the deposition time.

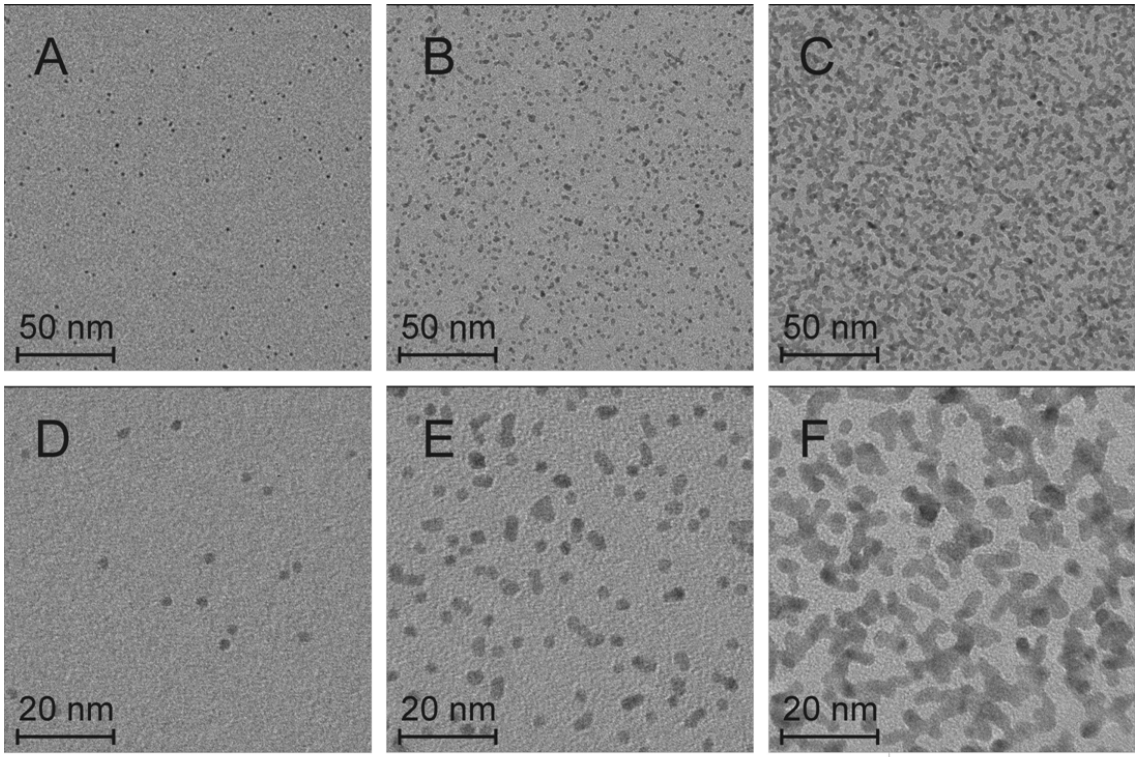

Figure 7.2 TEM images of different deposition times. (A) and (D) short deposition time, (B) and (E) medium, (C) and (F) long. The images demonstrate the coverage control that can be achieved using cluster deposition.

From image A and D it can be seen that for short deposition times isolated, spherical-shaped clusters are found, which are randomly-distributed on the carbon support. With increasing deposition time the cluster density increases on the surface (see image B and E) and larger particles can be observed that are not round-shaped. However, most of the clusters are sill isolated. If the deposition time is further increased, nearly no isolated particles are observed anymore. Instead larger particles are found that are not round in shape in contrast to the clusters of the other two samples.

7.1.3 Storage of deposited clusters under ambient conditions and in water

A typical cluster sample was characterized by TEM after deposition and subsequent transfer to ambient conditions (see A in Figure 7.3). A histogram is presented to illustrate the size distribution. It is noteworthy to mention in this context that the samples presented in Figure 7.3 were prepared using a flash-lamp pumped Nd:YAG laser in contrast to the rest of the samples presented in this work, which were prepared using a diode pumped laser for evaporation of the metal. Whereas the diode pumped laser exhibits a stable, small beam profile, the flash-pumped laser exhibits fluctuations in beam intensity and beam profile. Thus, the evaporation conditions are changing from pulse to pulse for the first type of laser and effects on the size distribution can not be excluded.

Image B presents sample A stored for seven days under ambient conditions. From the histogram it can be concluded that no distinctive change in size is observed. Even exposure to water does not affect the cluster size histogram as seen from image C.

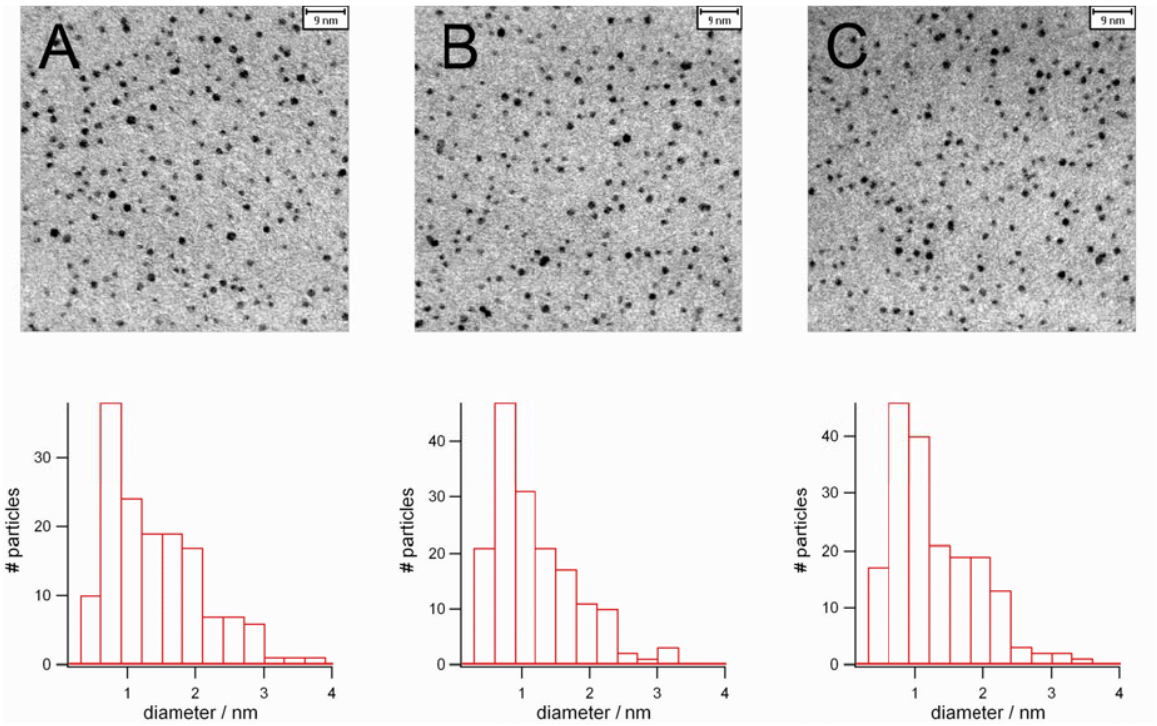

Figure 7.3 A typical cluster sample after transfer to ambient conditions (A), storage at ambient conditions for 7 days and storage in water for 1h.

7.1.4 Cluster sample under electrochemical conditions

In order to probe if small size-selected metal clusters can be applied as catalysts for electrochemical applications a TEM grid loaded with clusters has been kept in an argon purged electrolyte at 0.4 V for 1 hour.

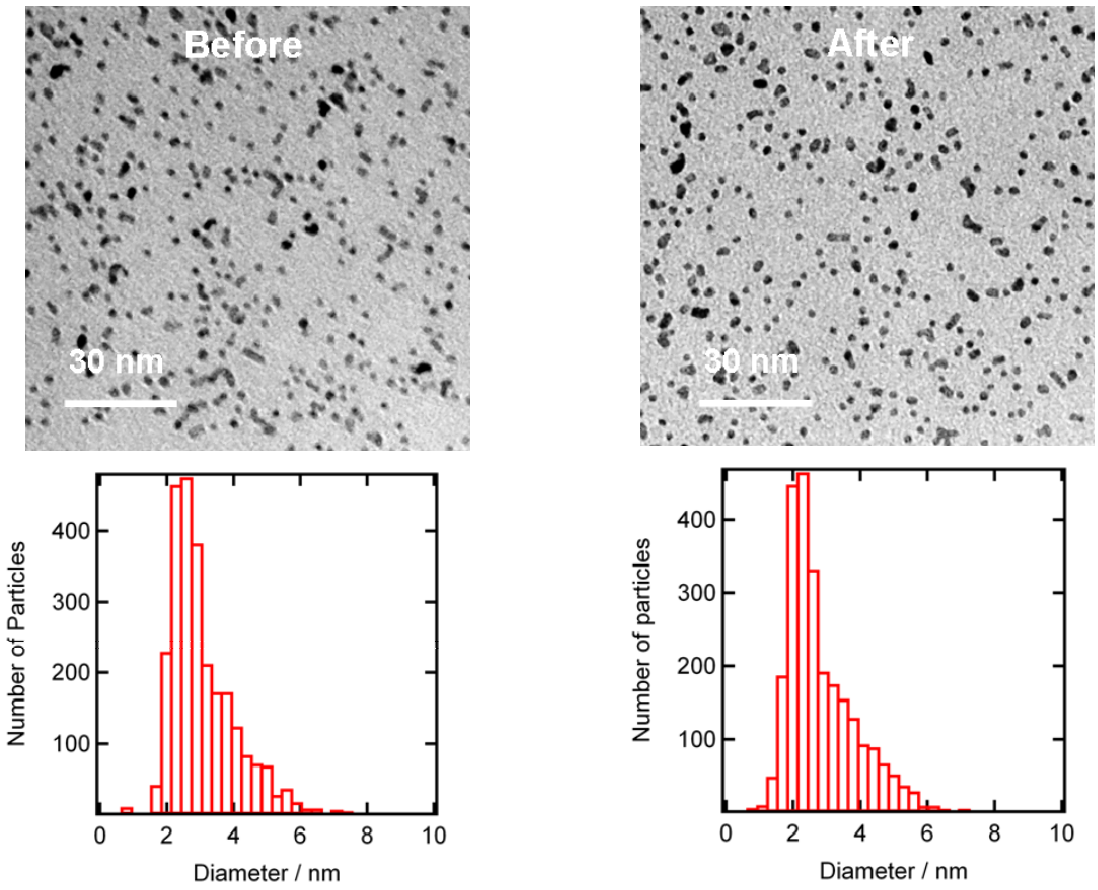

Figure 7.4 TEM images taken before (left) and after a soft electrochemical treatment (right). Clusters diameter remains constant at these conditions.

From the two histograms in Figure 7.4 it can be seen that the size does not change upon electrochemical treatment up to a potential of 0.4 V. Thus, further studies were performed in order to test the reactivity of small metal clusters under electrochemical conditions.

7.1.5 Deposition of cluster on glassy carbon

There are a few disadvantages in terms of reactivity studies using clusters deposited on TEM grids. The grid itself consists of a metal (usually gold or copper) and the clusters are not deposited exclusively on the carbon film but also on the metal grid. Furthermore, the coverages tested are low and hence, the detection of chemical conversions becomes hardly feasible. In order to overcome these limitations, glassy carbon samples were used as a support material for the metal clusters, assuming that the properties are comparable with those of TEM grid carbon films.

As mentioned previously the cluster concentration on the surface can be determined by integrating the neutralization current (chapter 3.1). An approach that allows examination of the total metal surface area of a catalyst under electrochemical conditions is the CO stripping method. The electrolyte is purged with CO in order to saturate the platinum surface of the catalyst at potential of 0.0 V. Subsequently, after removing CO from the electrolyte by purging it with argon, the potential is swept and the current is measured. Integration of the current peak gives a quantity for the CO that has been sticking on the surface before the experiment was performed.

Both methods have been investigated in the presented work. A typical CO stripping experiment for a cluster sample and polycrystalline platinum are shown in Figure 7.5.

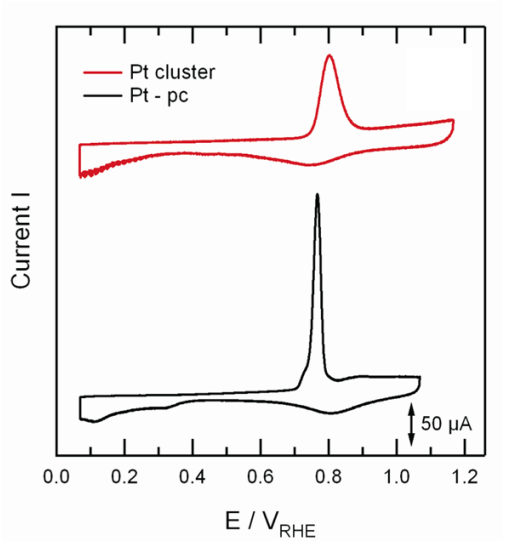

Figure 7.5 CO-stripping experiment performed for Pt clusters deposited on glassy carbon (red curve) and a polycrystalline Pt surface (black).

Comparison of the peak observed for Pt clusters with the one for a polycrystalline surface shows that the cluster peak is broadened and shifted to higher potential. A similar particle size effect has been shown previously for high surface area industrial catalysts and metal particles in the size-range of 2-3 nm deposited on gold.[136, 137]

In order to compare the two described methods, the values determined by CO stripping and integration of the cluster neutralization current, are plotted against each other in Figure 7.6.

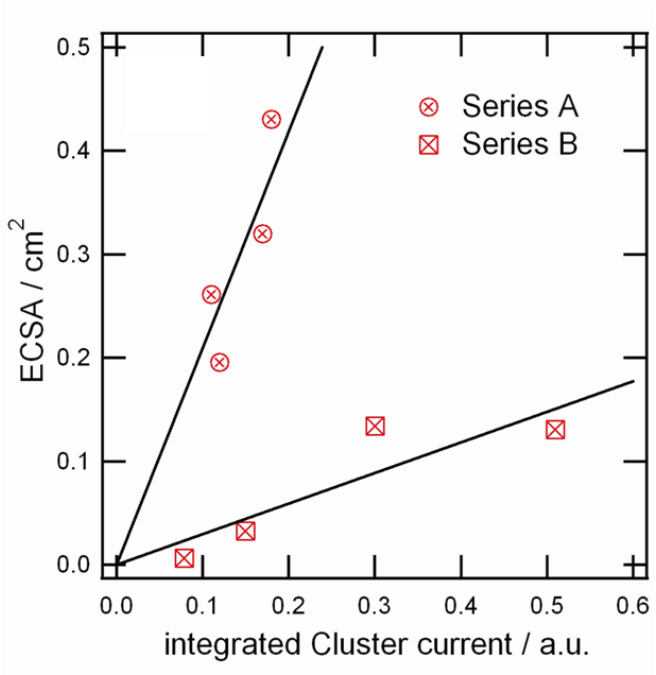

Figure 7.6 Cluster coverage determined via integration of the cluster neutralization current and CO stripping signal plotted with respect to each other. The electrochemical surface area (ESCA) is plotted on the y-axis and the integrated cluster neutralization current on the x-axis. Two different cluster sizes were measured. Series A represents a sample with the QMS operating in the ion optic mode (particle diameter ≈ 2.3 nm). The samples of series B were prepared with the QMS operating in the mass-selecting mode at a mass of 8970 amu leading to Pt_{46} cluster samples.

Series A has been evaluated for unselected clusters of different coverages and series B for different selected Pt_{46} surface concentrations. Furthermore, a linear fit has been performed for both series. It can be seen that the two methods correlate very well with respect to each other. Furthermore, this shows that electrochemical experiments can be performed using small size-selected metal clusters.

7.2 Discussion

The TEM images presented demonstrate clearly that samples of small metal clusters can be transferred to ambient conditions using the implemented transfer system. As the aforementioned TEM images show, samples that have been prepared with the quadrupole mass-spectrometer operating as an ion guide in order to prepare clusters that are large enough to get detected by TEM. By changing the settings of the electrostatic quadrupole bender, the cluster size has been tuned and the coverage can be controlled by varying the deposition time.

The samples are stable under ambient conditions, in water and in an electrolyte solution at a potential of 0.4 V.

Deposition of clusters on glassy carbon supports showed that electrochemical experiments can be performed. A shift to higher potentials and a broadening of the CO peak in the CO stripping experiment has been observed, which is in agreement with a previously observed particle size effect for high surface area catalysts and metal particles on gold (2-3 nm).[136, 137]

Furthermore, a comparison of the integrated cluster current and the integrated CO stripping signal of these samples shows that the different methods correlate very well. This enables a detailed characterization of the cluster samples for catalytic studies, since based on the neutralization current the cluster concentration becomes determinable. Additionally, the reactive surface area of cluster-based catalyst can be examined from CO-stripping experiments. In conclusion, this enables one to determine the reactive surface area per cluster, which is a very important characteristic for catalysis research and for comparison of the different cluster sizes in terms of reactivity.

7.3 Conclusion and outlook

The transfer of deposited, size-selected clusters on TEM grids and glassy carbon has been performed successfully. Furthermore, it has been shown that using cluster deposition for model catalyst preparation allows controlling of the size and coverage independently. Electrochemical experiments have been performed and promising results were obtained.[135, 138]

TEM grids for an environmental TEM (E-TEM) have been prepared and sent to a collaborating group (CNRS at Marseille). An E-TEM allows performing TEM studies at high pressures under reactive conditions. Thus, it is planned to study the morphology and shape of the clusters under reactive conditions.

Based on this work a collaboration has been started in November 2009 together with the group of Ib Chorkendorff from the DTU in Copenhagen. It is planned to deposit clusters onto small silicon based micro reactors.[139] The reactors are transferred to ambient conditions and sealed using a recently described anionic bonding method.[140] Catalytic studies of small size-selected clusters thus become feasible. Furthermore, clusters will be deposited on silicon based TEM grids in order to probe their stability on this support as well.

The main aim of this project is to establish cluster deposition for catalytic studies outside the vacuum in order to combine studies of small size-selected clusters in- and outside the vacuum. It is believed that a better understanding of the relation between size, electronic structure and catalytic properties can be achieved.

8 Conclusions

In the presented work three different topics have been investigated. The first part (chapter 4 and 5) focuses on the CO oxidation properties of small palladium cluster deposited onto MgO/Mo(100). Using a combination of different experimental UHV methods (TPR, p-MBRS, IRAS) it could be shown that CO poisoning is shifted to lower temperatures for small clusters, because the adsorption strength of CO on small clusters is weaker in comparison to single crystals and large facetted nanoparticles. In contrast, oxygen activation occurs at equivalent temperatures. This allows for performing the CO oxidation already at lower temperatures efficiently. These results are of great general interest, because the temperature of car exhaust has decreased in the last years due to optimization of engine efficiency and thus, CO poisoning might occur in a catalytic converter if the metal particles are too large.
Furthermore, the results show evidence for an additional mechanism taking place at temperatures around 300 K. It could be shown that in this case CO does not poison the clusters, instead surprisingly it even promotes oxygen activation. Further experimental as well as theoretical studies are in progress to verify this assumption.

Based on mole fraction and temperature dependent pulsed molecular beam reactive scattering (p-MBRS) experiments, micro kinetic simulations have been performed. It could be shown that a model, which can be used to describe CO oxidation on single crystals and large facetted nanoparticles, can reflect the general trends observed for small metal clusters. In a following step the single crystal model improved to take support effects into account, which play a significant role for low cluster surface/support surface ratios. Non-reactive reverse spill-over of the reactants was implemented in the simulation, using a model developed by Henry *et al.* and the activation barrier of the CO conversion and the CO desorption were lowered in accordance to the results presented in the CO poisoning study.
The integration led to a general improvement of the simulations in terms of reflecting the experimental results. The results demonstrate that for a low cluster / surface ratio spill-over effects should be taken into account in order to understand the mechanistic details completely.

The implementation of a MIES/UPS has been achieved successfully by developing a new measuring and data treatment technique as described in chapter 3.2.2 and 6. In order to test the setup, MIES and UPS spectra were recorded and analyzed for MgO/Mo(100). The adsorption of benzene on this support was probed. The results were compared with published spectra and a good agreement was found between these spectra and those measured in the nanocatalysis laboratory could be shown.
Furthermore, the adsorption properties of two organic molecules (trichloroethylene and cyclohexene) were investigated by means of MIES/UPS, with the purpose to test the setup towards its sensitivity. Whereas cyclohexene exhibits adsorption properties that could be explained easily, TCE shows a rather complicated adsorption behavior. A four step model has been developed based on MIES/UPS and TPD studies.
Since the setup is well-established, the group is trying to reach the next step of the project and investigate deposited clusters. First results have been gained; however, the results are not understood so far. Based on the aforementioned results, it is believed that MIES/UPS will reveal further details regarding the relation between electronic structure and reactivity.

The transfer of clusters to ambient conditions was accomplished as shown in chapter 0. By installing a vacuum lock a transfer system could be constructed that allows transferring samples between vacuum and ambient conditions.
Using TEM it was shown that clusters are randomly distributed on the surface after deposition. Size and coverage control could be confirmed in these studies and the stability was probed under ambient condition, in water and under soft electrochemical conditions. Further cluster samples were prepared on glassy carbon supports and electrochemical reactions were performed. Using CO stripping experiments, the reactive surface area was determined and compared to the coverage elucidated from the neutralization current measured during cluster deposition. The two different methods are in good agreement, confirming the possibility to use deposited clusters for catalytic studies. Additionally, the application of these two methods enables the determination the reactive surface area of a cluster, since the cluster coverage and the reactive surface area of the catalysts can be measured independently.

Further experiments are planned in order to investigate the properties of small metal clusters for gas-phase and electrochemical catalysis. Additionally, their stability under reactive conditions in different environments shall be explored.

9 Literature

[1] W. Ostwald, Physikalische Zeitschrift 1901, 3, 313.

[2] J. M. Thomas, Angewandte Chemie-International Edition 1994, 33, 913.

[3] S. T. Oyama, G. A. Somorjai, Journal of Chemical Education 1988, 65, 765.

[4] J. Hagen, Technische Katalyse, Wiley-VCH, 1996.

[5] P. L. J. Gunter, J. W. Niemantsverdriet, F. H. Ribeiro, G. A. Somorjai, Catalysis Reviews-Science and Engineering 1997, 39, 77.

[6] J. W. Niemantsverdriet, Spectroscopy in Catalysis, Wiley VCH, 2007.

[7] G. Ertl, Surface Science 1967, 6, 208.

[8] R. J. Behm, K. Christmann, G. Ertl, M. A. Vanhove, P. A. Thiel, W. H. Weinberg, Surface Science 1979, 88, L59.

[9] R. J. Behm, K. Christmann, G. Ertl, Surface Science 1980, 99, 320.

[10] J. Szanyi, D. W. Goodman, Catalysis Letters 1991, 10, 383.

[11] Z. Paal, R. Schlogl, G. Ertl, Journal of the Chemical Society-Faraday Transactions 1992, 88, 1179.

[12] W. Mausfriedrichs, M. Wehrhahn, S. Dieckhoff, V. Kempter, Surface Science 1990, 237, 257.

[13] K. Wandelt, Journal of Vacuum Science & Technology a-Vacuum Surfaces and Films 1984, 2, 802.

[14] H. Conrad, G. Ertl, J. Kuppers, S. W. Wang, K. Gerard, H. Haberland, Physical Review Letters 1979, 42, 1082.

[15] W. Huber, P. Zebisch, T. Bornemann, H. P. Steinruck, Surface Science 1991, 258, 16.

[16] G. Ertl, Catalysis Reviews-Science and Engineering 1980, 21, 201.

[17] 1997, DK patent application 0683/97.

[18] G. Ertl, Angewandte Chemie-International Edition 2009, 48, 6600.

[19] F. Besenbacher, I. Chorkendorff, B. S. Clausen, B. Hammer, A. M. Molenbroek, J. K. Norskov, I. Stensgaard, Science 1998, 279, 1913.

[20] P. L. Hansen, J. B. Wagner, S. Helveg, J. R. Rostrup-Nielsen, B. S. Clausen, H. Topsoe, Science 2002, 295, 2053.

[21] J. D. Grunwaldt, A. M. Molenbroek, N. Y. Topsoe, H. Topsoe, B. S. Clausen, Journal of Catalysis 2000, 194, 452.

[22] K. D. Jung, A. T. Bell, Journal of Catalysis 2000, 193, 207.

[23] U. Diebold, Surface Science Reports 2003, 48, 53.

[24] J. A. Horsley, Journal of the American Chemical Society 1979, 101, 2870.

[25] U. Heiz, A. Sanchez, S. Abbet, W. D. Schneider, Journal of the American Chemical Society 1999, 121, 3214.

[26] A. Sanchez, S. Abbet, U. Heiz, W. D. Schneider, H. Hakkinen, R. N. Barnett, U. Landman, Journal of Physical Chemistry A 1999, 103, 9573.

[27] A. A. Herzing, C. J. Kiely, A. F. Carley, P. Landon, G. J. Hutchings, Science 2008, 321, 1331.

[28] M. Baumer, H. J. Freund, Progress in Surface Science 1999, 61, 127.

[29] S. Giorgio, C. R. Henry, C. Chapon, J. M. Penisson, Journal of Crystal Growth 1990, 100, 254.

[30] S. Giorgio, C. Chapon, C. R. Henry, G. Nihoul, Philosophical Magazine B-Physics of Condensed Matter Statistical Mechanics Electronic Optical and Magnetic Properties 1993, 67, 773.

[31] C. R. Henry, Surface Science Reports 1998, 31, 231.

[32] S. Giorgio, C. R. Henry, C. Chapon, C. Roucau, Journal of Catalysis 1994, 148, 534.

[33] E. Perrot, A. Humbert, A. Piednoir, C. Chapon, C. R. Henry, Surface Science 2000, 445, 407.

[34] C. Becker, C. R. Henry, Surface Science 1996, 352-354, 457.

[35] S. Schauermann, J. Hoffmann, V. Johanek, J. Hartmann, J. Libuda, H. J. Freund, Catalysis Letters 2002, 84, 209.

[36] L. Piccolo, C. R. Henry, Journal of Molecular Catalysis a-Chemical 2001, 167, 181.

[37] I. Meusel, J. Hoffmann, J. Hartmann, J. Libuda, H. J. Freund, J. Phys. Chem. B 2001, 105, 3567.

[38] W. Harbich, S. Fedrigo, F. Meyer, D. M. Lindsay, J. Lignieres, J. C. Rivoal, D. Kreisle, Journal of Chemical Physics 1990, 93, 8535.

[39] U. Heiz, F. Vanolli, L. Trento, W. D. Schneider, Review of Scientific Instruments 1997, 68, 1986.

[40] M. A. Röttgen, S. Abbet, K. Judai, J. M. Antonietti, A. S. Worz, M. Arenz, C. R. Henry, U. Heiz, J. Am. Chem. Soc. 2007, 129, 9635.

[41] W. A. Deheer, Reviews of Modern Physics 1993, 65, 611.

[42] H. Hakkinen, M. Moseler, O. Kostko, N. Morgner, M. A. Hoffmann, B. von Issendorff, Physical Review Letters 2004, 93.

[43] U. Heiz, U. Landman, Nanocatalysis: Nanoscience and Technology, Springer, 2007.

[44] B. Yoon, H. Häkkinen, U. Landman, A. S. Wörz, J.-M. Antonietti, S. Abbet, K. Judai, U. Heiz, Science 2005, 307, 403.

[45] B. Huber, P. Koskinen, H. Hakkinen, M. Moseler, Nature Materials 2006, 5, 44.

[46] W. E. Kaden, T. P. Wu, W. A. Kunkel, S. L. Anderson, Science 2009, 326, 826.

[47] M. Henzler, W. Göpel, Oberflächenphysik des Festkörpers, Teubner, 2007.

[48] R. Popescu, R. Schneider, D. Gerthsen, A. Böttcher, D. Löffler, P. Weis, M. M. Kappes, Surface Science 2009, 603, 3119.

[49] R. Alayan, L. Arnaud, M. Broyer, E. Cottancin, J. Lerme, S. Marhaba, J. L. Vialle, M. Pellarin, Physical Review B 2007, 76.

[50] P. Gélin, M. Primet, Applied Catalysis B: Environmental 2002, 39, 1.

[51] K. C. Taylor, Catalysis Reviews Science and Engineering 1993, 35, 457.

[52] B. Hammer, J. K. Norskov, Nature 1995, 376, 238.

[53] M. Eigen, Discussions of the Faraday Society 1954, 194.

[54] T. Engel, G. Ertl, Journal of Chemical Physics 1978, 69, 1267.

[55] C. T. Campbell, G. Ertl, H. Kuipers, J. Segner, Journal of Chemical Physics 1980, 73, 5862.

[56] R. Imbihl, G. Ertl, Chemical Reviews 1995, 95, 697.

[57] H. Beusch, E. Wicke, P. Fieguth, Chemie Ingenieur Technik 1972, 44, 445.

[58] E. Wicke, P. Kummann, W. Keil, J. Schiefler, Berichte Der Bunsen-Gesellschaft-Physical Chemistry Chemical Physics 1980, 84, 315.

[59] N. Freyer, M. Kiskinova, G. Pirug, H. P. Bonzel, Surface Science 1986, 166, 206.

[60] G. Ertl, Science 1991, 254, 1750.

[61] S. Ladas, R. Imbihl, G. Ertl, Surface Science 1989, 219, 88.

[62] H. Conrad, G. Ertl, J. Kuppers, Surface Science 1978, 76, 323.

[63] G. Blyholder, Journal of Physical Chemistry 1964, 68, 2772.

[64] F. M. Hoffmann, Surface Science Reports 1983, 3, 107.

[65] C. Elschenbroich, Organometallchemie, Teubner, 2008.
[66] K. W. Kolasinski, Surface Science: Foundations of Catalysis and Nanoscience, John Wiley & Sons, 2008.
[67] A. M. Bradshaw, F. M. Hoffmann, Surface Science 1978, 72, 513.
[68] R. Imbihl, J. E. Demuth, Surface Science 1986, 173, 395.
[69] G. Ertl, H. P. a. P. B. W. D.D. Eley, in Advances in Catalysis, Vol. Volume 37, Academic Press, 1990, pp. 213.
[70] I. Meusel, J. Hoffmann, J. Hartmann, M. Heemeier, M. Baumer, J. Libuda, H. J. Freund, Catalysis Letters 2001, 71, 5.
[71] I. Meusel, J. Hoffmann, J. Hartmann, J. Libuda, H. J. Freund, Journal of Physical Chemistry B 2001, 105, 3567.
[72] R. T. K. Baker, E. B. Prestridge, R. L. Garten, Journal of Catalysis 1979, 56, 390.
[73] T. Risse, S. Shaikhutdinov, N. Nilius, M. Sterrer, H. J. Freund, Accounts of Chemical Research 2008, 41, 949.
[74] M. Boudart, D. G. Mariadassou, Kinetics of Heterogeneous Catalytic Reactions, Princeton University Press.
[75] S. Furuyama, H. Fujii, M. Kawamura, T. Morimoto, Journal of Physical Chemistry 1978, 82, 1028.
[76] E. A. Colbourn, W. C. Mackrodt, Surface Science 1984, 143, 391.
[77] C. Pisani, R. Dovesi, R. Nada, S. Tamiro, Surface Science 1989, 216, 489.
[78] F. Rumpf, H. Poppa, M. Boudart, Langmuir 1988, 4, 722.
[79] C. R. Henry, C. Chapon, C. Duriez, Journal of Chemical Physics 1991, 95, 700.
[80] C. R. Henry, Surface Science 1989, 223, 519.
[81] P. W. Atkins, Physical Chemistry, Wiley, 2006.
[82] R. Masel, Principles of Adsorption and Reaction on Solid Surfaces, Wiley Interscience, 1996.
[83] F. F. Schweinberger, Master Thesis, TU München 2009.
[84] C. N. Berglund, W. E. Spicer, Physical Review a-General Physics 1964, 136, 1030.
[85] C. N. Berglund, W. E. Spicer, Physical Review a-General Physics 1964, 136, 1044.
[86] W. Göpel, H.-D. Wiemhöfer, Statistische Thermodynamik, Spektrum Akademischer Verlag, 2000.
[87] N. D. Lang, W. Kohn, Physical Review B 1970, 1, 4555.

[88] G. A. Somorjai, Introduction to Surface Chemistry and Catalysis, John Wiley & Sons, 1994.
[89] G. Wedler, Eine Einführung in die Physisorption und Chemisorption, Verlag Chemie, 1970.
[90] M. Nonnenmacher, M. P. Oboyle, H. K. Wickramasinghe, Applied Physics Letters 1991, 58, 2921.
[91] G. Ertl, J. Küppers, Low Energy Electrons and Surface Chemistry Wiley-VCH, 1985.
[92] M. Lax, Journal of Chemical Physics 1952, 20, 1752.
[93] R. Hoffmann, Angewandte Chemie-International Edition in English 1987, 26, 846.
[94] S. Hüfner, Photoelectron Spectroscopy, Springer-Verlag, 1995.
[95] C. Kittel, Einführung in die Festkörperphysik, Oldenburg, 2005.
[96] F. Reinert, S. Hufner, New Journal of Physics 2005, 7.
[97] Y. Harada, S. Masuda, H. Ozaki, Chemical Reviews 1997, 97, 1897.
[98] H. Morgner, in Advances in Atomic Molecular, and Optical Physics, Vol. 42, Vol. 42, Academic Press Inc, San Diego, 2000, pp. 387.
[99] H. Brenten, H. Müller, A. Niehaus, V. Kempter, Surface Science 1992, 278, 183.
[100] G. Doyen, Surface Science 1982, 117, 85.
[101] M. Röttgen, PhD Thesis, TU München 2007.
[102] M. Liebermann, A. Lichtenberg, Principles of plasma discharges and materialy processing, Vol. 1, Wiley-Interscience: New York, 1994.
[103] M. A. Lieberman, A. J. Lichtenberg, Principles of Plasma Discharges and Materials Processing, John Wiley & Sons, 1994.
[104] E. L. Leasure, C. R. Mueller, T. Y. Ridley, Review of Scientific Instruments 1975, 46, 635.
[105] D. W. Fahey, W. F. Parks, L. D. Schearer, Journal of Physics E-Scientific Instruments 1980, 13, 381.
[106] P. R. Stracke, PhD Thesis, TU Clausthal-Zellerfeld 2000.
[107] W. Maus-Friedrichs, M. Wehrhahn, S. Dieckhoff, V. Kempter, Surface Science 1990, 237, 257.
[108] K. Judai, S. Abbet, A. S. Worz, M. A. Rottgen, U. Heiz, International Journal of Mass Spectrometry 2003, 229, 99.

[109] D. Proch, T. Trickl, Review of Scientific Instruments 1989, 60, 713.
[110] M. Röttgen, PhD Thesis, TU München 2003.
[111] G. Wedler, Lehrbuch der Physikalischen Chemie, Wiley-VCH, 1997.
[112] C. H. Hamann, A. Hamnett, W. Vielstich, Electrochemistry, Wiley VCH, 2007.
[113] A. J. Bard, L. R. Faulkner, ELECTROCHEMICAL METHODS: Fundamentals and Applications, JOHN WILEY & SONS, 2001.
[114] S. Kunz, F. F. Schweinberger, V. Habibpour, M. A. Rottgen, C. Harding, M. Arenz, U. Heiz, Journal of Physical Chemistry C 2010, 114, 1651.
[115] Y. T. Wong, R. Hoffmann, Journal of Physical Chemistry 1991, 95, 859.
[116] L. N. Kantorovich, M. J. Gillan, Surface Science 1997, 374, 373.
[117] M. Sterrer, T. Risse, H. J. Freund, Applied Catalysis a-General 2006, 307, 58.
[118] H. Conrad, G. Ertl, J. Koch, E. E. Latta, Surface Science 1974, 43, 462.
[119] V. Habibpour, PhD Thesis, TU München 2009.
[120] C. J. Harding, S. Kunz, V. Habibpour, V. Teslenko, M. Arenz, U. Heiz, Journal of Catalysis 2008, 255, 234.
[121] C. J. Harding, S. Kunz, V. Habibpour, U. Heiz, Physical Chemistry Chemical Physics 2008, 10, 5875.
[122] J. Hoffmann, I. Meusel, J. Hartmann, J. Libuda, H. J. Freund, Journal of Catalysis 2001, 204, 378.
[123] M. Galassi, GNU Scientific Library Reference Manual, 2nd ed., Network Theory Ltd., 2003.
[124] T. Engel, Journal of Chemical Physics 1978, 69, 373.
[125] C. R. Henry, C. Chapon, C. Duriez, The Journal of Chemical Physics 1991, 95, 700.
[126] A. Wörz, PhD Thesis, Universität Ulm 2005.
[127] M. C. Wu, J. S. Corneille, C. A. Estrada, J. W. He, D. W. Goodman, Chemical Physics Letters 1991, 182, 472.
[128] J. Gunster, S. Krischok, V. Kempter, J. Stultz, D. W. Goodman, Surface Review and Letters 2002, 9, 1511.
[129] D. Ochs, W. Maus-Friedrichs, M. Brause, J. Günster, V. Kempter, V. Puchin, A. Shluger, L. Kantorovich, Surface Science 1996, 365, 557.

[130] L. Kantorovich, A. Shluger, J. Gunster, J. Stultz, S. Krischok, D. W. Goodman, P. Stracke, V. Kempter, Nuclear Instruments & Methods in Physics Research Section B-Beam Interactions with Materials and Atoms 1999, 157, 162.
[131] D. Ochs, W. MausFriedrichs, M. Brause, J. Gunster, V. Kempter, V. Puchin, A. Shluger, L. Kantorovich, Surface Science 1996, 365, 557.
[132] J. Gunster, G. Liu, V. Kempter, D. W. Goodman, Surface Science 1998, 415, 303.
[133] I. Jordan, Forschungsarbeit, TU München 2010.
[134] S. Krischok, P. Stracke, V. Kempter, Applied Physics a-Materials Science & Processing 2006, 82, 167.
[135] K. Hartl, M. Nesselberger, K. J. J. Mayrhofer, S. Kunz, F. F. Schweinberger, G. Kwon, U. Heiz, M. Hanzlik, M. Arenz, Nano Letters 2010, submitted.
[136] M. Arenz, K. J. J. Mayrhofer, V. Stamenkovic, B. B. Blizanac, T. Tomoyuki, P. N. Ross, N. M. Markovic, Journal of the American Chemical Society 2005, 127, 6819.
[137] K. A. Friedrich, F. Henglein, U. Stimming, W. Unkauf, Colloids and Surfaces a-Physicochemical and Engineering Aspects 1998, 134, 193.
[138] S. Kunz, K. Hartl, M. Nesselberger, F. F. Schweinberger, G. Kwon, M. Hanzlik, K. J. J. Mayrhofer, U. Heiz, M. Arenz, PCCP 2010, submitted.
[139] T. R. Henriksen, J. L. Olsen, P. Vesborg, I. Chorkendorff, O. Hansen, Review of Scientific Instruments 2009, 80.
[140] P. C. K. Vesborg, J. L. Olsen, T. R. Henriksen, I. Chorkendorff, O. Hansen, Review of Scientific Instruments 2010, 81, 016111.

10 Appendix

10.1 Acknowledgements

First, I would like to thank Prof. Ulrich Heiz for the opportunity to work in his group, his support during the last three years and the chance to bear more responsibility than one usually has as a PhD student.
I appreciate the support of the mechanic and electronic work shop, especially Mr. Wiedemann and Mr. Schröter, who have been working very closely together with me. Without their permanent help, I would have never been able to finish the presented thesis on this level.
Thanks a lot to my gym team, Karl Mayrhofer and Matthias Arenz, for useful discussions and insights into different, scientific topics.
Furthermore, I would like to thank the whole Heiz group, especially Christopher Harding and Vahideh Habibpour, who worked together with me in the first period of my PhD thesis. Gustav Wiberg for spending more than three years in one office together with me, Florian Spirkl for useful discussions and insights into many physics topics; Florian Schweinberger who had to work and suffer most of the time with me and Josef Kiermaier for watching soccer games. Thanks to the current members of the nanocatalysis lab, who are GiHan Kwon, Florin Schweinberger, Tobias Zimmermann and Andrew Crampton, for a great working atmosphere and their enthusiastic motivation for the job we are doing.
I would like to thank those people and friends who are not working at the University for their support during the time of this thesis: Marcus Fischer, Thorben Hensler, Matthias Mikoteit, Johannes Gerber, Kati Zapp, Andreas Marschall, my room mates Daniel Globisch and Juliane Ritzka,
Thanks a lot to my parents for my education and the opportunity to follow my aims, to my sister Nikola and my brothers Tobias, Andreas and especially Henning, who studied together with me.
Finally, I would like to thank Sarah for her patience, useful advice and spending the last two years together with me as the best partner that I could ever imagine.

10.2 Statement (Erklärung)

Hiermit bestätige Ich, dass die der Fakultät für Chemie der Technischen Universität München zur Promotionsprüfung vorgelegte Arbeit mit dem Titel:

Cluster catalysis under UHV and ambient conditions

im Lehrstuhl für Physikalische Chemie unter Anleitung und Betreuung durch Prof. Dr. U. Heiz ohne sonstige Hilfe erstellt und bei der Abfassung nur die gemäß § 6 Abs. 5 angegebenen Hilfsmittel benutzt worden sind.
Die Dissertation in keinem anderen Prüfungsverfahren als Prüfungsleistung vorgelegt.

München, den 21.04.2010

Sebastian Kunz

10.3 Curriculum Vitae

Sebastian Kunz

Fernpaßstraße 44
81373 München
Germany

Phone: +49.89.289.13394
Mobile: +49.179.7360855
Email: sebastian-kunz@tum.de

Born: March 21st 1983 - Mannheim, Germany
Nationality: German

Research interests

Heterogeneous Catalysis, Spectroscopy, Quantum Mechanics, Materials Science, Clusters, Electronic Structure, Reaction Kinetics, Thermodynamics.

Education

PhD studies
Since March 2007

Chair of Physical Chemistry, Chemistry Department, Technische Universität München; Munich - Germany

Project	Cluster catalysis under vacuum and ambient condition;
Position	PhD Student funded by Kekúle Scholarship ("Fond der Chemischen Industrie") from September 2007 – August 2009 Member of the "European Graduate School on Sustainable Energy Technology" since September 2009
Supervisor	Prof. Dr. Ulrich Heiz

Diploma Thesis
April 2006 - February 2007

Department of Advanced Material Science, University of Augsburg; Augsburg - Germany

Project	Influence of the syntheses conditions on the adsorption properties of $Cu_3(BTC)_2$
Supervisor	Prof. Dr. Martin Hartmann

Diploma studies
October 2003 – February 2006
University of Technology Kaiserslautern; Kaiserslautern - Germany

Major Subjects: Physical, Technical and Organic Chemistry

Studies funded by a scholarship of the "Studienstiftung des Deutschen Volkes"

Intermediate Examination for Diploma
April 2002 – October 2003
University of Technology Kaiserslautern; Kaiserslautern - Germany

Project & Gamble award for best Examination of Intermediate Diploma

School Education
September 1993 – March 2002
Gauß-Gymnasium Worms; Worms - Germany

Abitur (A-levels) in March 2002

Presentations and talks

Talks

COST 41 Meeting
München - Germany, March 2010

First meeting of the “Graduate School on Sustainable Energy Technology”
Heeze - Netherlands, November 2009

COST 41 Meeting
Goteborg - Sweden, Mai 2009

Deutsches Katalytiker Treffen
Weimar - Germany, March 2009

COST 41 Meeting
Marseille - France, April 2008

Fond der Chemischen Industrie Treffen
Munich - Feburary 2008

Poster presentations

Deutsches Clustertreffen
Berlin - Germany, September 2007

Deutsche Zeolithes Tagung
Leipzig - Germany, March 2007

10.4 Publications

1. Poppl, A.; Kunz, S.; Himsl, D.; Hartmann, M., CW and pulsed ESR Spectroscopy of cupric ions in the metal-organic framework compound Cu-3(BTC)(2). *Journal of Physical Chemistry C* **2008,** 112, (7), 2678-2684.
2. Hartmann, M.; Kunz, S.; Himsl, D.; Tangermann, O.; Ernst, S.; Wagener, A., Adsorptive separation of isobutene and isobutane on Cu-3(BTC)(2). *Langmuir* **2008,** 24, (16), 8634-8642.
3. Harding, C. J.; Kunz, S.; Habibpour, V.; Teslenko, V.; Arenz, M.; Heiz, U., Dual-pulsed beam controlled mole fraction studies of the catalytic oxidation of CO on supported Pd nanocatalysts. *Journal of Catalysis* **2008,** 255, 234.
4. Harding, C. J.; Kunz, S.; Habibpour, V.; Heiz, U., Microkinetic simulations of the oxidation of CO on Pd based nanocatalysis: a model including co-dependent support interactions. *Physical Chemistry Chemical Physics* **2008,** 10, (38), 5875-5881.
5. Harding, C. J.; Kunz, S.; Habibpour, V.; Heiz, U., Dual reverse spill-over: Microkinetic simulations of the CO oxidation on Pd nanocatalysts. *Chemical Physics Letters* **2008,** 461, (4-6), 235-237.
6. Harding, C.; Habibpour, V.; Kunz, S.; Farnbacher, A. N.-S.; Heiz, U.; Yoon, B.; Landman, U., Control and manipulation of gold nanocatalysis: effects of metal oxide support thickness and composition. *J Am Chem Soc* **2009,** 131, (2), 538-48.
7. Kunz, S.; Schweinberger, F. F.; Habibpour, V.; Rottgen, M. A.; Harding, C.; Arenz, M.; Heiz, U., Temperature Dependent CO Oxidation Mechanisms on Size-Selected Clusters. *Journal of Physical Chemistry C* **2010,** 114, (3), 1651-1654.